



Theses and Dissertations

2006-03-16

Analysis of Viscous Drag Reduction and Thermal Transport Effects for Microengineered Ultrahydrophobic Surfaces

Jason W. Davies
Brigham Young University - Provo

Follow this and additional works at: <https://scholarsarchive.byu.edu/etd>



Part of the [Mechanical Engineering Commons](#)

BYU ScholarsArchive Citation

Davies, Jason W., "Analysis of Viscous Drag Reduction and Thermal Transport Effects for Microengineered Ultrahydrophobic Surfaces" (2006). *Theses and Dissertations*. 368.
<https://scholarsarchive.byu.edu/etd/368>

This Thesis is brought to you for free and open access by BYU ScholarsArchive. It has been accepted for inclusion in Theses and Dissertations by an authorized administrator of BYU ScholarsArchive. For more information, please contact scholarsarchive@byu.edu, ellen_amatangelo@byu.edu.

ANALYSIS OF VISCOUS DRAG REDUCTION AND THERMAL
TRANSPORT EFFECTS FOR MICROENGINEERED
ULTRAHYDROPHOBIC SURFACES

by

Jason W. Davies

A thesis submitted to the faculty of

Brigham Young University

in partial fulfillment of the requirements for the degree of

Master of Science

Department of Mechanical Engineering

Brigham Young University

April 2006

COPYRIGHT © 2005 Jason W. Davies

All Rights Reserved

BRIGHAM YOUNG UNIVERSITY

GRADUATE COMMITTEE APPROVAL

of a thesis submitted by

Jason W. Davies

This thesis has been read by each member of the following graduate committee and by majority vote has been found to be satisfactory.

Date

R. Daniel Maynes, Chair

Date

Brent W. Webb

Date

Jeffrey P. Bons

BRIGHAM YOUNG UNIVERSITY

As chair of the candidate's graduate committee, I have read the thesis of Jason W. Davies in its final form and have found that (1) its format, citations, and bibliographical style are consistent and acceptable and fulfill university and department style requirements; (2) its illustrative materials including figures, tables, and charts are in place; and (3) the final manuscript is satisfactory to the graduate committee and is ready for submission to the university library.

Date

R. Daniel Maynes
Chair, Graduate Committee

Accepted for the Department

Matthew R. Jones
Graduate Coordinator

Accepted for the College

Alan R. Parkinson
Dean, Ira A. Fulton College of Engineering and
Technology

ABSTRACT

ANALYSIS OF VISCOUS DRAG REDUCTION AND THERMAL TRANSPORT EFFECTS FOR MICROENGINEERED ULTRAHYDROPHOBIC SURFACES

Jason W. Davies

Department of Mechanical Engineering

Master of Science

One approach recently proposed for reducing the frictional resistance to liquid flow in microchannels is the patterning of micro-ribs and cavities on the channel walls. When treated with a hydrophobic coating, the liquid flowing in the microchannel wets only the top surfaces of the ribs, and does not penetrate into the cavities, provided the pressure is not too high. The net result is a reduction in the surface contact area between channel walls and the flowing liquid. For micro-ribs and cavities that are aligned normal to the channel axis (principal flow direction), these micropatterns form a repeating, periodic structure. This thesis presents numerical results of a study exploring the momentum and thermal transport in a parallel plate microchannel with such

microengineered walls. The liquid-vapor interface (meniscus) in the cavity regions is approximated as flat in the numerical analysis. Two conditions are explored with regard to the cavity region: 1) The liquid flow at the liquid-vapor interface is treated as shear-free (vanishing viscosity in the vapor region), and 2) the liquid flow in the microchannel core and the vapor flow within the cavity are coupled through the velocity and shear stress matching at the interface. Predictions reveal that significant reductions in the frictional pressure drop (as large as 80%) can be achieved relative to the classical smooth channel Stokes flow. In general, reductions in the friction factor-Reynolds number product (fRe) are greater as the cavity-to-rib length ratio is increased (increasing shear-free fraction), as the relative module length (length of a rib-cavity module over the channel hydraulic diameter) is increased, as the Reynolds number decreases, and as the vapor cavity depth increases. The thermal transport results predict lower average Nusselt (Nu) numbers as the cavity-to-rib length ratio is increased (increasing shear-free fraction), as the relative module length (is increased, and as the Reynolds number decreases with little dependence on cavity depth. The ratio of Nu to fRe was evaluated to characterize the relative change in heat transfer with respect to the reduction in driving pressure. Results show that the benefits of reduction in driving pressure outweigh the cost of reduction in heat transfer at higher Reynolds numbers and narrower relative channel widths.

ACKNOWLEDGEMENTS

There are a lot of people that I would like to thank for their help on this thesis. I want to thank my parents and siblings for the help they have given me throughout my life as I have pursued my education. They have always been supportive and encouraging to me, especially during the last few months of this project.

I would also like to acknowledge and thank Dr. Maynes and Dr. Webb for the steady guidance and direction they gave me. I want to thank them for their friendship, their patience with me, and their example.

I want to thank my friends for helping me out when I needed it and also my boss for his understanding as I have been working on this. Finally, thanks to all those I have known from the lab, they were always there to help me take a break.

TABLE OF CONTENTS

TITLE PAGE	i
COPYRIGHT	iii
ABSTRACT	ix
ACKNOWLEDGEMENTS	xiii
TABLE OF CONTENTS	xv
LIST OF FIGURES	xix
LIST OF SYMBOLS	xxvii
1 INTRODUCTION	1
1.1 INTRODUCTION TO DRAG REDUCTION	1
1.2 DRAG REDUCTION FUNDAMENTALS	2
1.3 DRAG REDUCING SURFACES	4
1.4 RESEARCH FOCUS	8
2 LITERATURE REVIEW	11
2.1 PREVIOUS WORK	11
2.1.1 Liquid Droplet Dynamics	11
2.1.2 Flow of a Liquid Continuum.....	14
2.2 CONTRIBUTION OF THIS WORK.....	19
3 HYDRODYNAMIC MODEL AND RESULTS	23
3.1 MODEL DEVELOPMENT	23
3.1.1 Metric for Comparison - fRe	24
3.1.2 Periodically Fully-developed Flow.....	25
3.1.3 Solution Methodology	27
3.2 DETAILED FLOW FIELD BEHAVIOR	30
3.2.1 Representative Streamlines.....	31
3.2.2 Streamwise-Velocity Field Behavior.....	32
3.2.3 Interface and Centerline Velocity Behavior	43
3.2.4 Wall-normal Velocity Behavior.....	54
3.2.5 Shear Stress Predictions for Rib Surface and Liquid-Gas Interface.....	55
3.3 GENERAL RESULTS OF THE DARCY FRICTION FACTOR – REYNOLDS NUMBER PRODUCT	57
4 CONSTANT WALL TEMPERATURE THERMAL TRANSPORT RESULTS	65
4.1 THERMAL MODEL DEVELOPMENT	65
4.1.1 Thermally Periodically Fully-developed	65
4.1.2 Metric for Comparison – Average Nusselt Number.....	70
4.1.3 Solution Methodology	72
4.2 THERMAL CONTOUR PLOTS	75
4.3 DETAILED THERMAL TRANSPORT PHYSICS.....	80
4.3.1 Influence of F_s on θ	83

4.3.2	Influence of Re on θ	85
4.3.3	Influence of L/D_h on θ	88
4.3.4	Influence of Z_c on θ	90
4.3.5	Heat Flux at the Interface and Rib Wall.....	90
4.4	AVERAGE NUSSELT NUMBER RESULTS.....	93
4.5	COMBINED EFFECT OF AVERAGE NUSSELT NUMBER AND DARCY FRICTION FACTOR – REYNOLDS NUMBER PRODUCT.....	97
5	CONCLUSIONS AND RECOMMENDATIONS.....	101
5.1	CONCLUSIONS.....	101
5.2	RECOMMENDATIONS.....	103
	REFERENCES.....	105
	Appendix A – User Defined Function Used for Numerical Modeling.....	109

LIST OF FIGURES

Figure 1.1: Velocity profile for fully-developed laminar flow through infinite parallel plates.....	3
Figure 1.2: Microengineered surface with microribs 8 μm tall by 4 μm wide and cavities 4 μm wide.....	5
Figure 1.3: Schematic of liquid over a Microengineered surface with gas-filled cavities.....	6
Figure 2.1: Schematic illustrating how the contact angle is measured.....	12
Figure 2.2: Schematic of the computational domain encompassing a rib/cavity module. Flow direction is from left to right.	20
Figure 3.1: Schematic of entrance near wall and cavity regions for liquid flow over an ultrahydrophobic surface exhibiting micro-rib structures and flow perpendicular to the ribs.	26
Figure 3.2: Schematic of the computational domain encompassing a rib/cavity module using the shear-free (SF) model. Flow direction is from left to right. The domain does not extend into the gas cavity and a shear-free boundary is placed at the liquid-gas interface.....	28
Figure 3.3: Schematic of the computational domain encompassing a rib/cavity module using the air cavity (AC) model. Flow direction is from left to right.	29
Figure 3.4: Representative streamlines for two different scenarios.....	31
Figure 3.5: Velocity profile of a classical fully-developed laminar channel flow.....	33
Figure 3.6: Nondimensionalized velocity profile in a fully-developed classical channel flow.	33
Figure 3.7: Schematic showing percentage of repeated module used in reporting velocity data.....	34
Figure 3.8: Velocity profile predictions for a (SF) case where $F_s=0.5$, $L/D_h=0.25$, and $Re=1000$ compared with a classical fully-developed channel flow.....	35
Figure 3.9: Near-wall velocity profile predictions for a (SF) case where $F_s=0.5$, $L/D_h=0.25$, and $Re=1000$ compared with a classical fully-developed channel flow.	36
Figure 3.10: Near-wall comparison of velocity profile predictions in the rib region for a (SF) case where $F_s=0.5$, $L/D_h=0.25$, and $Re=1000$ and a (AC) case where $F_s=0.5$, $L/D_h=0.25$, $Re=1000$, and $Z_c=1$; both also compared to a classical fully-developed channel flow.....	37

Figure 3.11: Near-wall comparison of velocity profile predictions in the cavity region for a (SF) case where $F_s=0.5$, $L/D_h=0.25$, and $Re=1000$ and a (AC) case where $F_s=0.5$, $L/D_h=0.25$, $Re=1000$, and $Z_c=1$; both also compared to a classical fully-developed channel flow	38
Figure 3.12: Velocity profile predictions for a (SF) case where $F_s=0.98$, $L/D_h=0.25$, and $Re=1000$ and a (AC) case where $F_s=0.98$, $L/D_h=0.25$, $Re=1000$, and $Z_c=1$; both also compared to a classical fully-developed channel flow.....	39
Figure 3.13: Near-wall region of velocity profile predictions above the cavity region for a (SF) case where $F_s=0.98$, $L/D_h=0.25$, and $Re=1000$ and a (AC) case where $F_s=0.98$, $L/D_h=0.25$, $Re=1000$, and $Z_c=1$; both also compared to a classical fully-developed channel flow	41
Figure 3.14: Near-wall region of velocity profile predictions above the cavity region for a (AC) case where $F_s=0.5$, $L/D_h=0.25$, $Re=1000$, and $Z_c=1$ and a (AC) case where $F_s=0.5$, $L/D_h=0.25$, $Re=0.4$, and $Z_c=1$ compared with a classical fully-developed channel flow.....	42
Figure 3.15: Near-wall velocity profile predictions for a (SF) case where $F_s=0.5$, $L/D_h=0.25$, and $Re=1000$ and a (SF) case where $F_s=0.5$, $L/D_h=0.05$, and $Re=1000$	43
Figure 3.16: Schematic illustrating the interface position ($y^*=0$) and the centerline position ($y^*=1$).....	44
Figure 3.17: Interface ($y^*=0$) velocities in the x -direction for many scenarios, unless otherwise specified in the legend $Re=1000$, $Z_c=2$, and $L/D_h=0.25$	45
Figure 3.18: Maximum dimensionless interface velocity (u^*_{im}) along the interface ($y^*=0$) vs. F_s for four relative rib/cavity module sizes and at $Re=1000$ for a (SF) model.....	47
Figure 3.19: Maximum dimensionless interface velocity (u^*_{im}) along the interface ($y^*=0$) vs. L/D_h for $F_s=0.98$, 0.875 , and 0.5 and at $Re=1000$ for a (SF) model.....	47
Figure 3.20: Maximum dimensionless interface velocity (u^*_{im}) along the interface ($y^*=0$) vs. Z_c for $F_s=0.98$ and 0.5 , where $Re=1000$, and $L/D_h=0.25$ for both a (AC) and a (SF) model.....	49
Figure 3.21: Maximum dimensionless interface velocity (u^*_{im}) along the interface ($y^*=0$) vs. Re for $Z_c=2$ for $F_s=0.98$ and 0.5 , where $Re=1000$, and $L/D_h=0.25$ for both a (AC) and a (SF) model.....	49
Figure 3.22: Dimensionless centerline ($y^*=1$) velocities in the x -direction for many scenarios, unless otherwise specified in the legend $Re=1000$, $Z_c=2$, and $L/D_h=0.25$	50
Figure 3.23: Dimensionless centerline velocity (u^*_{cl}) along the centerline ($y^*=1$) vs. F_s for four relative rib/cavity module sizes and at $Re=1000$ for a (SF) model.....	51
Figure 3.24: Dimensionless centerline velocity (u^*_{cl}) along the centerline ($y^*=1$) vs. Z_c for $F_s=0.98$ and 0.5 , where $Re=1000$, and $L/D_h=0.25$ for both a (AC) and a (SF) model.....	52

Figure 3.25: Dimensionless centerline velocity (u^*_{cl}) along the centerline ($y^*=1$) vs. Re for $Z_c=2$ for $F_s=0.98$ and 0.5 , and $L/D_h=.25$ for both a (AC) and a (SF) model.	53
Figure 3.26: Wall-normal velocity profile predictions for a (AC) case where $F_s=0.5$, $L/D_h=0.25$, $Z_c=2$, and $Re=1000$	55
Figure 3.27: Shear stress predictions for (AC) cases where $F_s=0.5$, $L/D_h=0.25$, and $Re=1000$; $F_s=0.5$, $L/D_h=0.25$, and $Re=0.4$; and $F_s=0.98$, $L/D_h=0.25$, and $Re=1000$	56
Figure 3.28: Predictions of fRe vs. F_s in a parallel plate channel with ultrahydrophobic walls and microrib/cavity structures oriented perpendicular to the flow direction for five relative rib/cavity module sizes and at $Re=1000$ (SF) model.	58
Figure 3.29: Predictions of fRe vs. relative rib/cavity module size for slip fractions of 0.98 , 0.875 , and 0.5 and at $Re=1000$ (SF) model.	59
Figure 3.30: Dependence of fRe on the depth of the vapor cavity for the $L/D_h=0.25$ channel at $Re=1000$ and at slip fractions of $F_s=0.98$ and 0.5	60
Figure 3.31: Variation of fRe with Reynolds number for the $L/D_h=0.25$ channel, slip fractions of 0.02 and 0.5 , and for both the (SF) interface and coupled vapor cavity interface conditions.	62
Figure 4.1: Qualitative variation of the bulk mean temperature, T_m , changes for a fully-developed laminar parallel plate flow with walls at a constant temperature, T_s	66
Figure 4.2: Temperature profiles at two different x -locations in a fully-developed laminar parallel plate flow with walls at a constant temperature, $T_s=300K$	68
Figure 4.3: Dimensionless temperature, θ , profiles at two different x -locations in a fully-developed laminar parallel plate flow with walls at a constant temperature, $T_s=300K$	68
Figure 4.4: Schematic of the entrance wall and cavity regions for liquid flow over an ultra-hydrophobic surface exhibiting micro-rib structures and flow perpendicular to the ribs. Both hydrodynamic and thermal boundary layers are shown as well as how the constant wall temperature is imposed.	69
Figure 4.5: Schematic of the computational domain encompassing a rib/cavity module. Flow direction is from left to right. The domain extends into the gas cavity and the temperature of all the walls is indicated as T_s	74
Figure 4.6: Contour plot of Ω for $F_s=0.5$, $Z_c=1$, $L/D_h=0.25$, and $Re=1000$	76
Figure 4.7: Contour plot of Ω for $F_s=0.5$, $Z_c=1$, $L/D_h=0.25$, and $Re=0.4$	78
Figure 4.8: Contour plot of Ω for $F_s=0.98$, $Z_c=1$, $L/D_h=0.25$, and $Re=1000$	78
Figure 4.9: Contour plot of Ω for $F_s=0.5$, $Z_c=2$, $L/D_h=0.05$, and $Re=0.4$	79
Figure 4.10: Schematic showing percentage of repeated module and mixed mean temperature T_m used in reporting dimensionless temperature data.	80
Figure 4.11: Schematic showing dimensionless temperature, θ , for a case where $F_s=0.5$, $Re=1000$, $L/D_h=.25$, and $Z_c=2$ compared to a classical case.	81

Figure 4.12: Schematic showing the near-wall region of dimensionless temperature, θ , for a case where $F_s=0.5$, $Re=1000$, $L/D_h=.25$, and $Z_c=2$; compared to a classical case.	83
Figure 4.13: Schematic showing comparison θ profiles where $F_s=0.5$ and $F_s=0.98$ while $Re=1000$, $L/D_h=0.25$, and $Z_c=2$. Also shown is θ for a classical scenario.	84
Figure 4.14: Schematic showing the near-wall region (20% of channel) of a comparison of θ profiles where $F_s=0.5$ and $F_s=0.98$ while $Re=1000$, $L/D_h=0.25$, and $Z_c=2$. Also shown is θ for the classical scenario.	85
Figure 4.15: Schematic showing effect of Re on the θ profile. A classical case is shown with two ultrahydrophobic cases where $Re=1000$ and $Re=4$ for $F_s=0.98$, $L/D_h=0.25$, and $Z_c=2$	87
Figure 4.16: Near-wall region showing the effect of Re on the θ profile. A classical case is shown with two ultrahydrophobic cases where $Re=1000$ and $Re=4$ for $F_s=0.98$, $L/D_h=0.25$, and $Z_c=2$	88
Figure 4.17: Schematic showing the effect of L/D_h on the θ profile. A classical case is shown with three ultrahydrophobic cases where $L/D_h=0.05$ and $L/D_h=2.5$ for $F_s=0.5$, $Re=1000$, and $Z_c=2$	89
Figure 4.18: Normalized heat flux at the rib wall and interface for two ultrahydrophobic cases where $Re=1000$ and $Re=4$ for $F_s=0.5$, $L/D_h=0.25$, and $Z_c=2$	91
Figure 4.19: Normalized heat flux at the rib wall and interface for two ultrahydrophobic cases where $L/D_h=0.25$ and $L/D_h=0.05$ for $F_s=0.5$, $Re=4$, and $Z_c=2$	92
Figure 4.20: Normalized heat flux at the rib wall and interface for two ultrahydrophobic cases where $Z_c=2$ and $Z_c=0.1$ for $F_s=0.98$, $Re=1000$, and $L/D_h=0.25$	92
Figure 4.21: Schematic showing effect of Re on Nu for $F_s=0.98$ and $F_s=0.5$ where $L/D_h=0.25$, and $Z_c=2$	94
Figure 4.22: Schematic showing effect of Re on Nu for $F_s=0.98$ and $F_s=0.5$ where $L/D_h=2.5$, and $Z_c=2$	95
Figure 4.23: Schematic showing effect of F_s on Nu for $L/D_h=0.05$ and $L/D_h=2.5$ where $Re=1000$, and $Z_c=2$	96
Figure 4.24: Schematic showing effect of Re on $(Nu/fRe)/(Nu/fRe)_{classical}$ for $F_s=0.98$ and $F_s=0.5$ where $L/D_h=2.5$ and 0.25 , and $Z_c=2$	98
Figure 4.25: Schematic showing effect of F_s on $(Nu/fRe)/(Nu/fRe)_{classical}$ for $L/D_h=0.05$ and $L/D_h=2.5$ where $Re=1000$, and $Z_c=2$	99

LIST OF SYMBOLS

Acronyms

Acronym	Definition
AC	Air cavity included in the model
SF	Shear-Free, liquid-gas interface modeled as full slip
UDF	User Defined Function

Roman Symbols

Symbol	Unit(AC)	Definition
A	m^2	Channel cross sectional area
B	m	Channel span-wise width
c_p	$J/kg/K$	Specific heat
D_h	—	Channel hydraulic diameter $\left(\frac{4A}{P_w}\right)$
F	—	Average friction factor $\left(\frac{2D_h}{\rho\bar{u}\left(\frac{\Delta P}{L}\right)}\right)$
fRe	—	Friction factor-Reynolds number product
F_s	—	Slip fraction $\left(\frac{l_s}{L}\right)$
H	m	Vapor cavity depth
\bar{h}	$W/m^2/K$	Heat transfer coefficient
H	m	Channel gap-width between microengineered walls
K	$W/m/K$	Thermal conductivity
l_s	m	Cavity width or region of vanishing shear stress interface
l_r	m	Micro-rib width or region of no-slip interface
L	m	Module length (length of one rib and one cavity) $(l_r + l_s)$
L/D_h	—	Normalized microrib/cavity module length

\dot{m}	kg/s	Mass flow rate
Nu	—	Average Nusselt number
P	Pa	Pressure
Pr	—	Prandtl number (ν/α)
P_w	m	Channel perimeter
q''	W/m ²	Heat flux
Re	—	Reynolds number $\left(\frac{\rho \bar{u} D_h}{\mu} \right)$
T	K	Temperature at specified location
T_m	K	Bulk mean fluid temperature or mixing temperature
T_{mi}	K	Mean inlet temperature
T_{mo}	K	Mean outlet temperature
T_s	K	Temperature at the surface or wall
U	m/s	Streamwise fluid velocity
u^*	—	Dimensionless velocity in streamwise direction (u/u_{mc})
u_{im}^*	—	Dimensionless interface velocity in streamwise direction
u_{cl}^*	—	Dimensionless centerline velocity in streamwise direction
\bar{u}	m/s	Average fluid velocity
u_{mc}	m/s	Maximum velocity in a classical channel flow with same Re and geometry
U_∞	m/s	Channel core fluid velocity
U_{max}	m/s	Maximum velocity
v	m/s	Wall-normal fluid velocity
X	—	Streamwise coordinate
Y	—	Wall-normal coordinate
y^*	—	Dimensionless coordinate in wall-normal direction ($2y/H$)
Z_c	—	Relative vapor cavity depth $\left(\frac{h}{l_s} \right)$

Greek Symbols

Symbol	Unit(AC)	Definition
α	m^2/s^2	Thermal diffusivity
δ	m	Boundary layer thickness
δ_t	m	Thermal boundary layer thickness
ϕ	Radians	Angle measurement
μ	kg/m/s	Dynamic viscosity
ν	m^2/s	Kinematic viscosity
θ	—	Dimensionless temperature $\left(\frac{T_s - T}{T_s - T_m} \right)$
ρ	kg/m^3	Fluid density
Ω	—	Dimensionless contour temperature $\left(\frac{T_s - T}{T_s - T_{mo}} \right)$
ζ	—	Dimensionless heat flux $\left(\frac{q'' D_h^2}{k(T_s - T_{mo})} \right)$

1 INTRODUCTION

1.1 INTRODUCTION TO DRAG REDUCTION

During the past decade the field of microfluidics has developed dramatically. What was once a novel idea for scientists and engineers has become an integral part in the development of drug research, genetic research, and even inkjet technology. As this field has developed there have been several challenges encountered along the way. One of these challenges is the significant amount of required pressure increase for small scale flows through channels. For ($\Delta P \sim 1/D^4$, for equivalent flow rates, the increase in driving pressure is proportional to the inverse of the diameter of the channel raised to the fourth power). The required driving pressure gradient is a direct result of the viscous drag exerted on the walls of the duct. One focus of this thesis will be on characterizing a relatively new method proposed for significant reductions in the pressure losses due to frictional drag for special cases. While any reduction in pressure is an extreme advantage in these situations, some undesirable influences may result. In microfluidic applications heat transfer is frequently important (e.g., integrated cooling of computer chips) and when the frictional drag is changed the heat transfer is affected. Along with the study of frictional drag, this thesis will focus on a parametric study to help understand and predict trends in heat transfer behavior.

This study will not only be important to the field of microfluidics, but it will also be applicable to many fields where viscous drag is significant and must be overcome.

Within these fields any reduction in drag is of great benefit. The cost to overcome the effects of drag is power use and as drag is reduced, less work is needed for the system, resulting in more efficient and less costly designs.

To date there is very little work that undertakes this type of problem. General trends are understood, but there has been no comprehensive study. One of the objectives of this work is to provide a fundamental and detailed understanding of the flow physics and thermal transport using such surfaces. The literature review will explain previous related work and will describe how this work represents a significant contribution to this field.

1.2 DRAG REDUCTION FUNDAMENTALS

Any object moving through a fluid will experience a drag, or a net force exerted by the fluid on the object. Drag can be divided into two categories: pressure drag and viscous drag. Pressure or form drag is drag that comes directly from the pressure on the object. Viscous or frictional drag is caused by the shear stress on the object. Usually pressure drag is dominant in external flows unless the object is highly streamlined. In internal flows through straight constant-area channels viscous drag dominates and the driving force, or the pressure gradient, is required to overcome the shear force of the fluid on the wall.

By way of review, a laminar parallel plate channel flow will illustrate the key components of frictional drag and will help introduce the method this study explores to reduce drag. Figure 1.1 illustrates the fully-developed velocity profile of laminar flow through infinite parallel plates. In this figure the walls are depicted at the top and bottom

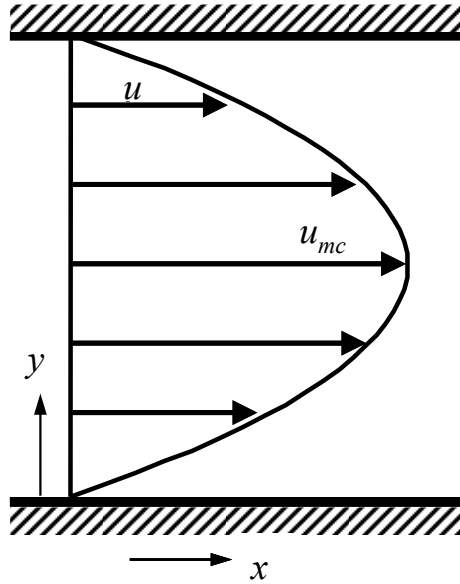


Figure 1.1: Velocity profile for fully-developed laminar flow through infinite parallel plates.

of the schematic and it is at these boundaries that the no-slip condition exists. The flow profile is parabolic with the maximum velocity (u_{mc}) at the centerline and is directed in the x -direction. Under the influence of an applied pressure gradient fluid motion will result. When steady conditions are attained, the force from the applied pressure gradient must be balanced with the force required to shear the fluid. The drag force is equal to the integral of the product of the shear stress at the wall and the differential area over which the shear stress acts.

$$D = \int \tau_{wall} dA_{wall} = \int_A \mu \left. \frac{du}{dy} \right|_{y=0} dA_{wall} \quad (1.1)$$

In the fully-developed case the velocity profile will not change over the length of the pipe and for a specific fluid, a given pressure gradient, a specified channel height, and

a specified length the drag will always be the same value. For such a scenario the only way to reduce drag without changing the geometry would be to change the velocity profile and/or area over which the shear stress acts.

1.3 DRAG REDUCING SURFACES

New surfaces have recently been engineered [1] that can result in drag reduction by both reducing the area in contact with the fluid and changing the velocity gradient at the wall. When coated with a hydrophobic coating the surfaces become highly liquid repellent. These surfaces have been termed ultrahydrophobic [2], which implies a high degree of non-wetting, such that if a droplet were placed on the surface, not only would it bead up, but it would have little resistance to motion on the surface. Such surfaces will only reduce drag for unique scenarios (i.e., a non-wetting surface with the appropriate liquid flowing over it).

Figure 1.2 shows an electron microscope image of one example of this type of surface and will help illustrate how drag is reduced. The view in Fig. 1.2 shows the top of the ultrahydrophobic surface and the edge (the darker region at the bottom of the image). The surface is made up of a silicon substrate with a layer of SU-8 photoresist on top into which the microcavities have been etched. The rectangular protrusions are called microribs.

A typical ultrahydrophobic surface will have many microscale cavities that are etched into it. These cavities must be small (in Fig. 1.2 the cavities are 8 μm deep by 4 μm wide) to prevent the liquid from entering into them. One method for creating these

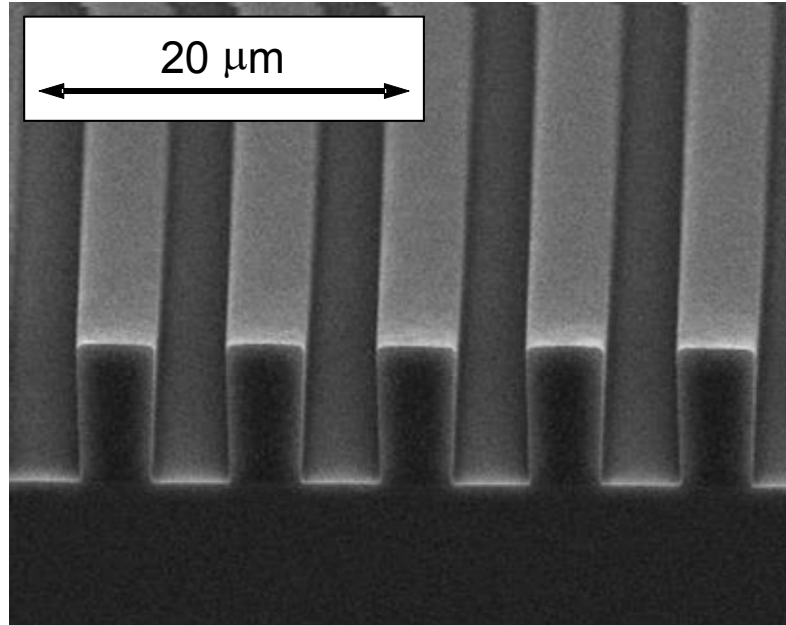


Figure 1.2: Microengineered surface with microribs 8 μm tall by 4 μm wide and cavities 4 μm wide.

surfaces uses a photolithographic process. In this process a negative photoresist (SU-8 25) is spun onto silicon wafers and a mask exhibiting the desired microrib/cavity dimensions was used to develop the microstructure patterns with light of the appropriate wavelength. An SU-8 developer solution was then used to treat the wafer, leaving the desired microstructure rib/ cavity geometry on the surface. Once hard-baked, SU-8 adheres permanently to the silicon substrate. After thermal treatment of the SU-8, the wafers were coated with a hydrophobic solution [3]. An initial visual evaluation of these surfaces may make it seem counter-intuitive that the added “roughness” on the surface helps reduce viscous drag. This phenomenon can be explained. Roughness increases the viscous drag on surfaces when the fluid is present over the entire surface. In the case of ultrahydrophobic surfaces the small size of the cavities and the hydrophobic coating prevent liquid from entering into the cavity regions, provided the local pressure is not too

high. The cavity regions are filled with gas and the liquid does not cover the entire surface. Figure 1.3 shows schematically an ultrahydrophobic surface with liquid on top of it.

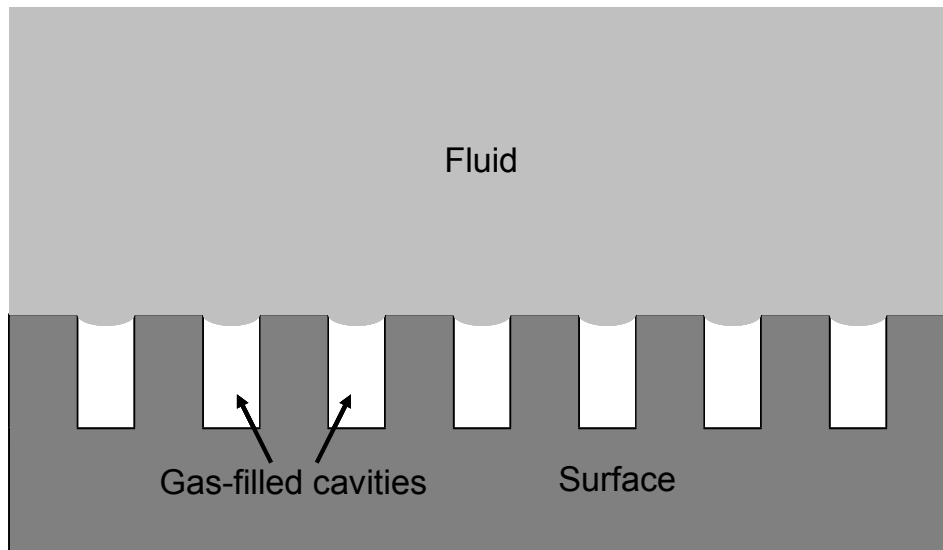


Figure 1.3: Schematic of liquid over a Microengineered surface with gas-filled cavities.

Gas-filled cavities are the critical factor in reducing drag along the surface. It can be seen that the area of fluid in contact with the solid surface has been reduced. This unique configuration also changes the velocity profile. The combination of these two conditions can reduce the net drag force on the surface. Because of the no-slip condition, the velocity of the liquid in contact with the top of the rib must be zero, but at the gas-liquid interface the liquid velocity need not be zero. The gas at the interface is free to move and because of the difference in viscosities between gases and liquids the shear stress at the interface will be very small. Air, for example, exhibits viscosity three orders

of magnitude smaller than typical liquids. At this liquid-gas interface two kinematic conditions must be satisfied, the fluid velocities and the shear stresses must be equal at the interface.

It should be noted that this type of significant drag reduction is unique only to scenarios where the fluid flowing through the channel is a liquid and the cavities are filled with gas. For scenarios where the cavity is filled with liquid and the fluid moving through the channel is gas the difference in viscosities and densities would not permit high velocities at the gas-liquid interface and the reduction in drag would be small. In addition to having a relatively low density and low viscosity fluid in the cavities the surface must be hydrophobic or non-wetting. If the fluid is not repelled by the surface then it can wet the cavity and the likely result would be an increase in drag. The wetting characteristics are determined by the surface tensions at the liquid-solid-gas interfaces. Optimization of the hydrophobic coating with the solid surface material and the liquid flowing over it is necessary for maximum effect.

Drag reduction could potentially be very dependent on the geometry of the surface and microcavities and the bulk fluid velocity above the surface. Figure 1.2 illustrates only one configuration for an ultrahydrophobic surface. The surface could be modified in many ways to obtain different results in drag reduction. For example, the cavities could be wider or they could be made deeper. Instead of microribs being formed on the surface, microposts (square protrusions) could be formed, further minimizing the contact area. An unlimited number of geometries exist, each having a different effect on the velocity of the fluid above and net force or drag on the surface. Not only will surface

geometry be important in reducing drag, but the bulk velocity of the fluid could also have an effect on the overall drag exhibited by the surface.

In addition to reducing drag, ultrahydrophobic surfaces will have an effect on the overall heat transfer of the surface. Heat transfer from a surface is extremely dependent on the velocity field of the fluid moving over it. The geometry of the microribs, the barrier of the gas-filled cavities, and the change in the velocity field above the surface will all affect the thermal transport of the surface, potentially decreasing its effectiveness at transferring heat. In microfluidic applications where heat transfer is important, ultrahydrophobic surfaces have the benefit of reducing drag, but may come at the cost of reducing thermal transport.

1.4 RESEARCH FOCUS

This study will explore the heat transfer properties and flow characteristics for surfaces with microribs and flows moving in a direction perpendicular to the microcavities. The study is limited to the two-dimensional parallel plate channel case with liquid flowing between the surfaces. A parametric investigation of the important relevant dimensional parameters that influence this flow will be conducted. Namely the influence of the following parameters will be explored:

- Relative size of cavity to rib surface
- Reynolds number based on the channel hydraulic diameter
- Relative cavity depth
- Relative length of a module length (one rib and one cavity), or ratio of the module length over the hydraulic diameter

Reynolds numbers in the laminar region will be explored and heat transfer will be analyzed assuming a constant wall temperature. This research will be limited to the scenario where the cavities are filled with air and the liquid moving through the channel is water. Different results would be expected for different mixtures of fluids and gases. It is from this parametric study that the general trends in drag and heat transfer will be understood.

2 LITERATURE REVIEW

2.1 PREVIOUS WORK

2.1.1 Liquid Droplet Dynamics

Much work has been performed on the development of ultrahydrophobic surfaces with the driving force being the recognized influence this technology could have on the microfluidics and MEMS fields. Methods used to produce these surfaces have been continually improving and developing and the technology has been improved to the point where most patterns (i.e., micro-ribs or microposts) with dimensions in the micrometer range can be created [1]. Some limitations do exist as to how deep the micro-cavities can be fabricated, depending on the process employed.

One example of the evolution of this field is the work done by Jansen et al. and Kim et al. [4,5]. A well-known characteristic of deep reactive ion etching (RIE) has been used to their advantage in producing surfaces with ultrahydrophobic properties. During a typical deep RIE process unwanted silicon structures on the nanometer scale are formed. They are formed as a byproduct when etching deep into material. Native oxide, dust, or other impurities can act as micromasks and nanoscale spikes or needles of silicon can form [4]. Kim has utilized this unique byproduct of deep RIE, or the black silicon method, to produce surfaces covered with nanoscale spikes, or NanoTurf [5]. When these surfaces are coated with a hydrophobic coating, NanoTurf has the advantage that

when a liquid droplet is placed on it, the liquid will only come in contact with the tips of the silicon spikes, therefore exhibiting a very small liquid-solid contact.

The majority of prior work on ultrahydrophobic surfaces focuses on liquid droplet behavior exposed to the surface [2,6-10]. An important parameter related to the hydrophobicity of the surface is the contact angle of the water droplet. The contact angle (ϕ) is the angle between the surface and the edge of the water droplet as shown in Figure 2.1.

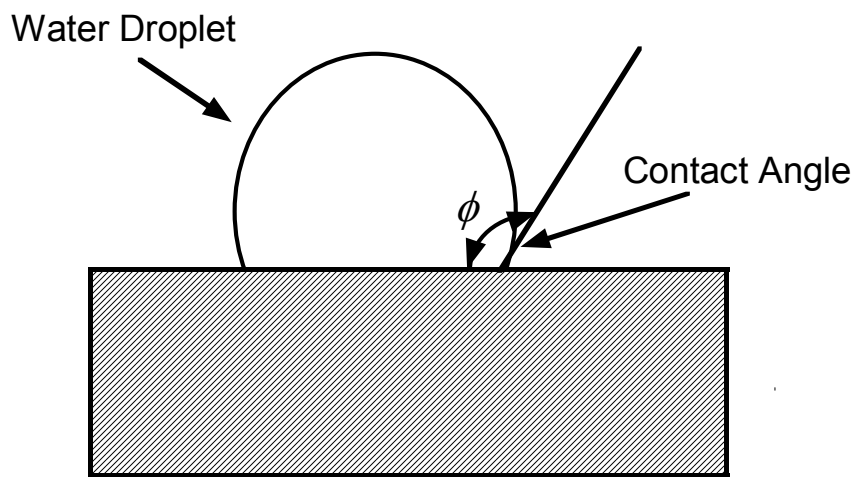


Figure 2.1: Schematic illustrating how the contact angle is measured.

With increasing hydrophobicity the contact angle of the water droplet approaches 180° and there is less resistance to motion of the droplet. In fact, a NanoTurf surface has achieved contact angles approaching the limit of 180° corresponding to a droplet flow resistance reduction of 99% compared to a silicon surface without microstructures or a hydrophobic coating [5].

Flow resistance of these surfaces is measured using a simple tilting experiment. In this experiment the angle of the surface at which the droplet begins to move is recorded. The tilting angle can be compared between an ultrahydrophobic surface and an untreated surface to measure the flow resistance reduction. Kim et al. also performed a tilting experiment for a water droplet in a microchannel made of two ultrahydrophobic surfaces which resulted in a droplet flow resistance reduction of 95% [5].

A study performed by Bico et al. [11] observed contact angles approaching 180° for a water droplet placed on a hydrophobic rough substrate. Different microstructured hydrophobic surfaces were analyzed (spikes, shallow cavities, and microribs). In this study the prediction of the contact angle was found to be most dependent on the fraction of the solid surface actually in contact with the liquid. In addition to the area of the surface in contact with the liquid the surface tension was important. The value of the surface tension depends on the solid, the liquid, and the vapor. A similar study was performed by Oner et al. [2] in which contact angles were measured for different surface configurations.

Of particular interest concerning droplet research is finding ways to move and manipulate individual droplets. There are potentially many microfluidic applications where this technology could be utilized. The ability to move small quantities of fluid and combine them contributes to miniaturizing laboratory analyses. Electrowetting has been used to accomplish this. Surface tension is highly sensitive and can be controlled electrically; electrowetting electrically adjusts the surface tension of the liquid. A change in the surface tension between the solid and the liquid changes the contact angle and

leads to fluid motion. This type of micro-liquid handling has been explored by Lee et al. [12].

2.1.2 Flow of a Liquid Continuum

Beyond the research addressing liquid droplet dynamics, there is significant interest in the dynamics of a liquid continuum between two ultrahydrophobic surfaces. This is a fascinating new field where only limited previous work has taken place. The alternating no-slip/no-shear regions create a unique flow. Far downstream of the microchannel inlet the flow may ideally reach a periodically fully-developed condition.

To date only three researchers have reported experimental work in this field. The first is from Ou et al. [1]. In this study significant drag reduction was observed for flow of a continuous liquid through a parallel plate microchannel constructed with ultrahydrophobic surfaces. The ultrahydrophobic surfaces were fabricated using photolithography to create uniform microribs or microposts on the surface. The surfaces were then coated with a hydrophobic coating which prevented the liquid from penetrating and wetting the cavities formed by the microribs and microposts. Ou showed that it was the combination of both the surface roughness and the hydrophobic coating that reduced the drag. By preventing the liquid from entering the cavities there exists less liquid-solid contact area and more liquid-gas contact area. The no-slip condition applied requires a zero velocity at the solid surface while the liquid at the liquid-gas interface experiences a much smaller shear stress. The shear stress at this interface is proportional to the ratio of viscosities.

A channel was created to measure the effect these surfaces would have on pressure drop in continuous flow. In the experimental setup only one of the surfaces was

ultrahydrophobic while the other surface was made of a smooth hydrophilic glass. The motivation behind having one glass no-slip surface was to allow optical access to measure the air-water interface profile suspended between the microposts. The pressure decrease in the direction of the flow was measured for various micropost and microrib configurations and flow rates. In each case the dimensions of the microposts were $30\ \mu\text{m}$ by $30\ \mu\text{m}$ square and the spacing between microposts varied for each surface from $30\ \mu\text{m}$ to $150\ \mu\text{m}$. It was observed that surfaces with larger spacing between microposts caused more reduction in pressure drop, as much as 40%. The pressure drop was found to increase linearly with flow rate and the magnitude of the reduction in the pressure drop increased monotonically with increased spacing between microposts.

The effect of the channel wall spacing, or the spacing between the ultrahydrophobic surface and the hydrophilic surface, was also studied. An average pressure drop reduction was calculated over a range of flow rates for different channel depths, holding the aspect ratio of the channel cross section to a constant value. It was found that the pressure drop increased linearly with increasing channel depth. In other words, as the channel depth was made larger the ultrahydrophobic surfaces affected the reduction in pressure drop less. In the limit, the ultrahydrophobic surfaces exerted negligible influence for channels with large hydraulic diameters.

Choi et al. has also contributed experimentally to understand the drag reduction associated with ultrahydrophobic surfaces in channel flow of a continuous liquid [13]. In this study both surfaces of the microchannel were ultrahydrophobic and they report preliminary results in the overall drag reduction of approximately 20%~30%. In these previous studies no extensive research was conducted on the optimization of the channel

configuration to reduce drag nor were the thermal transport dynamics investigated. Knowledge of heat transfer could be important to the field of microfluidic devices.

Most recently work done by Woolford et al. [3] has shown analytical and experimental results in this field. One significant difference in this work is the cavities and ribs are oriented longitudinally or in the direction of the flow. The results showed that the reductions in the total frictional resistance increases as the channel hydraulic diameter and/or microrib width are reduced. Drag reductions of up to 27% were measured experimentally. Analytical predictions show drag reductions of up to 90%. The results also showed significant correlation between the analytical and experimental results with dynamically similar conditions. Greater deviation was observed with increasing relative size of the shear-free regions.

One of the difficulties with using microscale heat exchangers is the required pressure drop to move fluid through the system. If ultrahydrophobic surfaces could be used in this application, there would be a large benefit in the pressure drag reduction, but it is critical to also understand how the heat transfer characteristics will be affected.

Previous analytical research on this topic has also been limited. The studies that have appeared have focused only on momentum transport characteristics and, like experimental results, do not characterize the thermal transport behavior. Philip [14] investigated eight different viscous flow problems with mixed no-slip and no-shear boundary conditions, and determined an analytical flow solution for each scenario. Having mixed no-slip/no-shear boundary conditions is a simplified model of an ideal ultrahydrophobic surface; the solid area in contact with the liquid has a no-slip boundary

condition, while the gas/liquid interface could be ideally modeled as a shear-free boundary. The following cases were studied:

1. Unbounded shear flow over a plate with a longitudinal no-shear slot
2. Unbounded shear flow over a plate with a regular array of such slots
3. Fully-developed flow in a circular tube with one or more longitudinal slots
4. Fully-developed flow between two parallel plates with a longitudinal no-shear slot in one of them
5. Flows between two parallel plates with a regular array of longitudinal slots on one plate
6. Shear Stokes flow over a single plate with a single transverse no-shear slot
7. Shear Stokes flow over a plate with a regular array of such slots; and Stokes flow due to a two-belt stirrer (two co-planar moving belts in contact with the fluid, one of them moves in the positive x -direction, while the other moves in the negative x -direction)

The first five solutions are found by the use of conformal mapping to solve Laplace's equation satisfying the mixed boundary conditions. The Stokes flow solutions were found by a general method of solving the biharmonic equation in the upper half plane subject to the mixed boundary conditions on the real axis. These solutions are given without direct characterization of the corresponding drag reduction for each scenario.

The focus of this thesis is on flow through a parallel plate channel where the no-shear slots on the surfaces are transverse, or perpendicular, to the flow direction. Philip's solution to Stokes flow over a regular array of transverse slots is most closely related to

this thesis. Several significant differences between Philip's solution and the focus of this thesis exist. 1. Stokes flow assumes the inertial and body forces in the Navier-Stokes equation are equal to zero, an assumption only correct at low Reynolds numbers. 2. Philip's solution modeled flow over a single plate, while this thesis is focused on parallel plate channel flow. 3. No analysis of the heat transfer was performed. 4. The vapor space and its contribution was neglected.

Benzi et al. [15] arrived at a similar result as Philip through a different method. Using a mesoscopic model of the fluid-wall interactions and solving the momentum equations using the Lattice Boltzmann Equation (LBE) a numerical solution to parallel plate flow through a channel with mixed slip and no-slip conditions was obtained. This study was a simplification of work done by Cottin-Bizonne et al. [16] in which molecular dynamics were used to solve the same problem presented by Philip. Cottin-Bizonne is careful to point out that this solution holds for scenarios where the liquid does not enter into and wet the cavities between the microribs, i.e., there is no curvature at the liquid-gas interface; this will occur at low pressures. In contrast, high pressures in the fluid create more force at the liquid-gas interface and result in a curved interface boundary. Results by both Benzi and Cottin-Bizonne agree and match those presented by Philip. In addition to showing the same streamlines as Philip they also reported a slip length for each scenario. The slip length is used as a measure of drag reduction and is defined as the distance between the wall and the position at which the linear extrapolation of the velocity profile vanishes. Although the no-slip condition will be valid at the liquid-solid interface, from a macroscopic viewpoint flow over an ultrahydrophobic surface appears to slip. Macroscopically, the effects of both the no-shear and no-slip regions average out

and have the averaged effect of slip at that interface. From this apparent slip an effective slip length can be calculated.

Very few studies have attempted to model the general trends in drag reduction for ultrahydrophobic surfaces depending on different parameters such as Reynolds number, channel geometries (hydraulic diameters), and ultrahydrophobic surface geometries. Ou et al. has contributed the most to the field with his experimental work on flow rates (Reynolds number variation), surface geometry effects (spacing of square microposts variation), and variation of the hydraulic diameter. Most studies focus only on the effect of the ratio of no-slip area to shear-free area. In addition to the small amount of work done on the hydrodynamic characteristics of this type of flow no previous work has considered the heat transfer implications.

2.2 CONTRIBUTION OF THIS WORK

The scope of this thesis is to perform a parametric study on continuous laminar flow through parallel plate channels with ultrahydrophobic surfaces. As was previously noted, far downstream of the microchannel inlet (in relative terms), the flow may ideally reach a periodically fully-developed condition wherein the flow structure repeats from one rib/cavity module to the next with the flow moving in a direction perpendicular to the microcavities. Numerical results exploring both the momentum transport and heat transfer will be presented for a two-dimensional periodically fully-developed condition. The liquid-vapor interface (meniscus) in the cavity regions is treated as ideal in the numerical analysis (flat). Two conditions are explored with regard to the cavity region: 1) The liquid flow at the liquid-vapor interface is treated as no-shear (vanishing viscosity in the vapor region), and 2) the liquid flow in the microchannel core and the vapor flow

within the cavity are coupled through matching the velocity and shear stress at the interface. The geometry of the channel is shown in Fig. 2.2. H represents the channel gap-width between microengineered surfaces, h represents the vapor cavity depth, l_r is the micro-rib width, l_s is the cavity width, and L is the width of one rib and one cavity ($L=l_r+l_s$). The influences of four variables will be studied: channel Reynolds number, Re ; relative cavity depth, $Z_c=h/l_s$; slip fraction, $F_s=l_s/L$; and relative module length, L/D_h . The Reynolds number will be varied from 0.4 – 2000, Z_c will range from 0.1 – 4, F_s from 0 – 0.98, and L/D_h from 0.05 to 2.5. Constant fluid properties will be imposed.

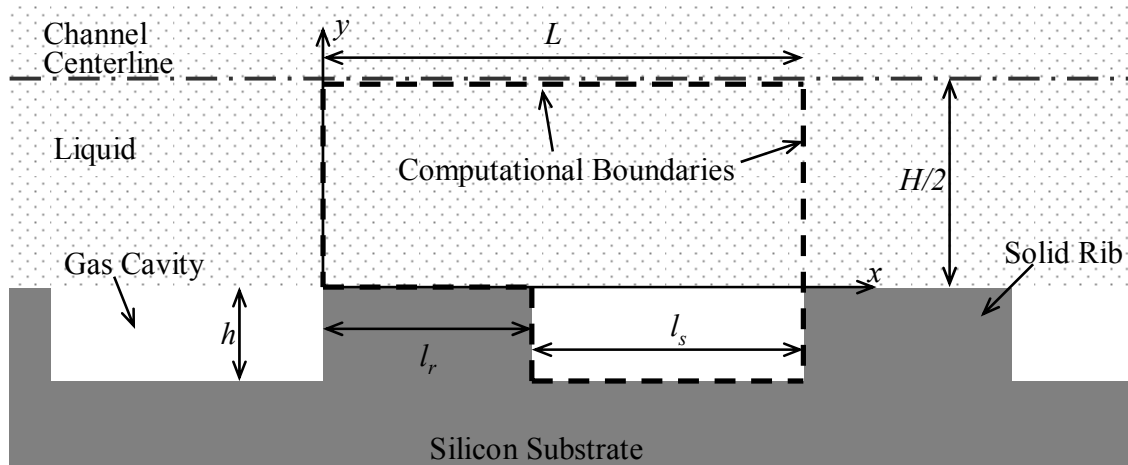


Figure 2.2: Schematic of the computational domain encompassing a rib/cavity module. Flow direction is from left to right.

It is intended that this thesis will add to the knowledge of the general trends in drag reduction characteristics of ultrahydrophobic surfaces and will clarify parametric effects. Further the thermal transport will be investigated. The results of this study will

assist in optimizing the surface topology for friction drag reduction and heat transfer characteristics in microfluidic applications.

3 HYDRODYNAMIC MODEL AND RESULTS

3.1 MODEL DEVELOPMENT

A parametric study was conducted utilizing a two-dimensional periodically fully-developed analytical model of an ultrahydrophobic channel to obtain hydrodynamic results. In the hydrodynamic results two different modeling conditions were explored. The first model approximated the fluid-gas interface as a full slip boundary (zero shear) or ($du/dy = 0$) at that interface (this model is abbreviated as “SF” meaning “Shear-Free”). Neglecting the viscosity at the liquid-vapor interface was assumed to be a reasonable approximation because the ratio of viscosities for the fluid and gas of interest is small, $\mu_{air}/\mu_{water} \approx 0.02$.

The second model did not neglect the vapor space, but included a gas-filled cavity in the computational domain (this model is abbreviated as “AC” meaning “Air Cavity”). At the interface the fluid velocities and shear stresses are set equal to each other in the liquid and vapor phases. The second model was used to evaluate the approximation made in the first model and to show the effect of the relative vapor-cavity depth, Z_c . Both models approximated the boundaries as perfectly hydrophobic, i.e., there was no fluid that entered the cavity and the meniscus shape was flat.

3.1.1 Metric for Comparison - fRe

By way of comparison it is useful to compute the Darcy friction factor-Reynolds number product, fRe , where the Reynolds number is based on the hydraulic diameter, D_h (3.1).

$$D_h = \frac{4A}{P_w} = 2H \quad (3.1)$$

The hydraulic diameter is defined as four times the cross sectional area, A , divided by the wetted perimeter, P_w and represents a length scale for non-circular geometries. The friction factor, f , represents the integrated frictional resistance. For the classical no-slip two-dimensional channel flow $fRe = 96$ [17] and is constant regardless of Re or H . Following the classical approach [17], fRe can be expressed as

$$fRe = \frac{2D_h^2}{\bar{u}\mu} \frac{\Delta P}{L} \quad (3.2)$$

where ΔP is the pressure drop across a rib-cavity module, \bar{u} is the average channel velocity, μ is the absolute viscosity of the liquid, and L is the rib-cavity module length. In practice a mass flow rate per unit of channel width was specified in the numerical scheme and iteration continued until the solution was converged. Subsequently the pressure drop was determined by integrating the drag over the ultrahydrophobic surface and the liquid vapor interface and fRe was determined from 3.2.

fRe serves as a valuable metric for comparing drag reduction from channels with ultrahydrophobic surfaces to classical no-slip channels. Regardless of the channel geometry or Re the classic case has a constant fRe , which means that fRe values from ultrahydrophobic cases can be calculated and compared to the classical case. If the ultrahydrophobic fRe is lower than 96 this would indicate that the channel reduces drag. fRe is also beneficial because it normalizes all scenarios from which comparisons and conclusions about different geometric configurations can be drawn.

3.1.2 Periodically Fully-developed Flow

Although the reduction in pressure drop is simple to compare between a classical flow and flow through microengineered channels, the fundamental momentum transport dynamics differ significantly. Consider the near-wall region of a channel wall that exhibits micro-rib structures separated by vapor-filled cavities, as illustrated in Fig. 3.1. Liquid is flowing over the top of the wall from left to right in the figure and perpendicular to the ribs at a core velocity, U_∞ . The surface begins at $x = 0$ and boundary layer growth will occur on the first rib section where the wall shear stress decreases from its maximum value at $x = 0$ in the streamwise (x) direction. If the rib length is sufficiently large and continuum behavior is prevalent, the liquid velocity at the wall will vanish to satisfy the no-slip condition. For $l_r < x < l_r + l_s$ (the cavity region), the liquid will no longer be in contact with a solid surface and the liquid velocity at the vapor-liquid interface need not be zero.

At the vapor-liquid interfaces several phenomena not common in traditional boundary layer flows are evident. First, the liquid velocity at the interfaces will increase,

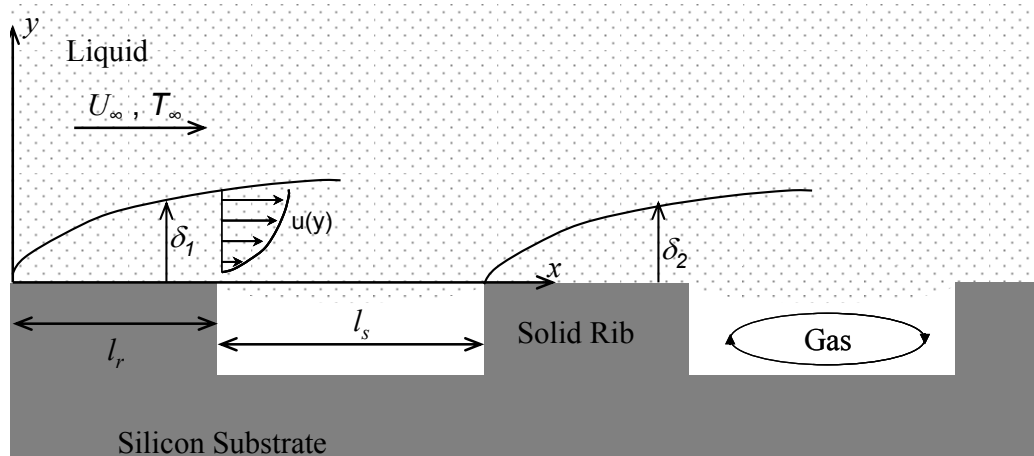


Figure 3.1: Schematic of entrance near wall and cavity regions for liquid flow over an ultrahydrophobic surface exhibiting micro-rib structures and flow perpendicular to the ribs.

starting from zero at the trailing edge of the micro-rib. Also, the liquid and vapor velocities will be equal and the shear stress at the interfaces will be small since the viscosity of the liquid phase will be approximately two orders of magnitude greater than in the vapor phase. The shape of the interface, and consequently the streamlines in the liquid, are dependent on the surface tension, the contact angle of the liquid-solid-vapor interface, and the thermodynamic pressure in both the liquid and vapor phases. A convection cell will exist in the vapor cavity, driven by the induced motion at the interface. At the second rib ($x > l_r + l_s$) a second momentum boundary layer begins to grow inside of the first and the wall shear stress will again decrease along the solid rib in the streamwise direction, although the initial value will not be as high as for the preceding rib. This behavior will repeat in the streamwise direction, and provided the meniscus shape remains the same, far downstream from the channel inlet a periodically fully-developed state may be established. At this point the flow will exhibit periodic

variations in the x-direction across repeating modules (of length $L = l_r + l_s$) consisting of a single rib and cavity. It is this periodically fully-developed condition where entry effects have vanished that will be modeled in this study.

3.1.3 Solution Methodology

A classical control volume approach was employed to characterize the periodically fully-developed flow through an infinitely wide channel for steady, laminar, conditions with constant fluid viscosity. The coupled x- and y-momentum equations and the equation of continuity given below for an incompressible Newtonian fluid were solved numerically.

$$\rho u \frac{du}{dx} + \rho v \frac{du}{dy} = \frac{dP}{dx} + \mu \left(\frac{d^2 u}{dx^2} + \frac{d^2 u}{dy^2} \right) \quad (3.3)$$

$$\rho u \frac{dv}{dx} + \rho v \frac{dv}{dy} = \frac{dP}{dy} + \mu \left(\frac{d^2 v}{dx^2} + \frac{d^2 v}{dy^2} \right) \quad (3.4)$$

$$\frac{du}{dx} + \frac{dv}{dy} = 0 \quad (3.5)$$

u is the streamwise (x) velocity, v is the wall-normal (y) velocity, P is the static pressure, μ is the fluid viscosity and ρ is the fluid density. Equations (3.3-3.5) were solved for the domains illustrated schematically in Fig. 3.2 and Fig. 3.3. The figures indicate a module length, L , consisting of one rib and cavity section of the two-dimensional channel. The shape of the meniscus at the cavity interface was assumed to be perfectly flat, representing the limiting case of perfectly hydrophobic walls. In reality the meniscus will

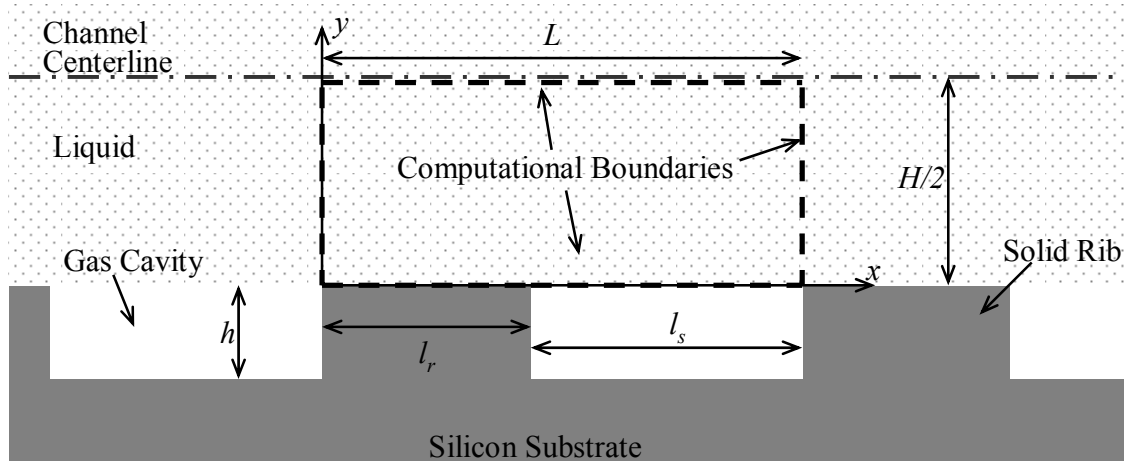


Figure 3.2: Schematic of the computational domain encompassing a rib/cavity module using the shear-free (SF) model. Flow direction is from left to right. The domain does not extend into the gas cavity and a shear-free boundary is placed at the liquid-gas interface.

be present, but a flat meniscus serves as a benchmark of the best case scenario. The micro-rib width where the no-slip condition exists is of length l_r and the vapor space is of length l_s . Symmetric boundary conditions were specified at the channel centerline, $y = H/2$ and no-slip and no-penetration at $y = 0$ and $0 \leq x \leq l_r$. The conditions at the upstream and downstream edges parallel to the y -axis were specified to be periodic, meaning u , v , du/dx and dv/dx were set to be equal at corresponding locations along these two faces. At the liquid-vapor interface, $y = 0$ and $l_r \leq x \leq l_r + l_s$ two conditions were explored. First, the interface was specified with a vanishing shear stress (“SF” model see Fig. 3.2). The second treatment modeled the cavity space solving Eqs. (3.3-3.5) in both the liquid and vapor spaces with their appropriate transport properties (“AC” model see Fig. 3.3). For this scenario the solutions were coupled by matching local velocities and shear stresses at the interface. The liquid properties were specified to remain constant and equal to those

of water at standard temperature and pressure. Likewise the vapor fluid properties were specified to be constant at the values of air at standard conditions.

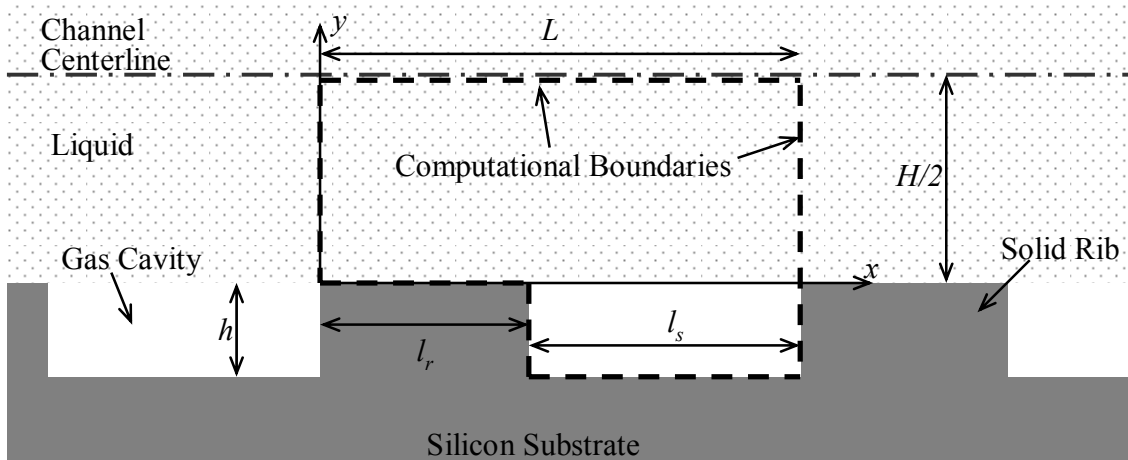


Figure 3.3: Schematic of the computational domain encompassing a rib/cavity module using the air cavity (AC) model. Flow direction is from left to right.

Due to the non-linearity of the momentum equations, solutions to Eqs. 3.3-3.5 for a fixed l_r , l_s , and H , depend on the channel Reynolds number. The domain was discretized into different cells. Each cell had a group of nodes associated with it. The segregated solver was used to obtain the solution. In this solution scheme the governing equations Eqs. 3.3-3.5 were solved sequentially. Because the governing equations are non-linear and coupled several iterations of the solution loop must be performed before a converged solution is obtained. A point implicit (Gauss-Seidel) linear equation solver was used in conjunction with an algebraic multigrid method to solve for the variables in the domain. Grid-independent solutions were obtained by successively refining the computational grid, using dynamic grid refinement, until the solution was independent of the grid. Cell

clustering was implemented near all regions of anticipated high gradients, particularly above the no-slip boundary and in the regions of transition between the rib and cavity. In practice grid refinement was carried out until the drag on the surface no longer changed significantly. In some scenarios this represented grids with up to 600,000 nodes.

Several important non-dimensional parameters exist for the varying scenarios of interest, these being the relative module length, L/D_h , the slip fraction, $F_s = l_s/L$, the Reynolds number, $Re = \rho \bar{u} D_h/\mu$, and the relative cavity depth, $Z_c = h/l_s$. L/D_h and F_s were varied in the ranges 0.05 – 2.5 and 0 – 0.98, respectively. Re was varied from 0.4 – 2000 and Z_c was varied from 0.1 to 2. The range of Re was chosen to be in the laminar regime while the range for F_s was chosen based on manufacturing capabilities.

3.2 DETAILED FLOW FIELD BEHAVIOR

It is enlightening to examine closely the detailed local flow behavior throughout the entire flow field. The following sections will focus on this behavior. First, representative streamlines will be shown to illustrate the motion of the flow in both the liquid and vapor filled regions. Second, velocity variation will be examined both in the wall-normal and streamwise directions, comparing the shear free (SF) model to the air cavity (AC) model. Third, the wall-normal velocity data will be illustrated, and finally, the wall shear stress behavior on the rib and cavity sections will be shown and discussed. Several different cases will be used to illustrate the intricacies of the overall flow dynamics and how the local behavior is influenced as the parameters F_s , Re , L/D_h , and Z_c are varied.

3.2.1 Representative Streamlines

In order to illustrate more clearly the motion of the fluid as it moves through the computational domain Fig. 3.4 shows streamlines for two different scenarios. The first scenario is for $F_s = 0.5$, $Re = 1000$, $L/D_h = 0.25$, and $Z_c = 1$, while the second scenario is for $F_s = 0.98$, $Re = 1000$, $L/D_h = 0.25$, and $Z_c = 1$. Throughout the liquid region in both cases the streamlines far from the wall are straight, while those streamlines close to the wall show motion away from the wall above the rib and toward the wall in the region above the cavity. The streamlines in the air cavity show a region of recirculation. The difference between the two slip fractions show that there is less influence on the liquid flow streamlines as the slip fraction increases. These streamlines shown in the Fig. 3.4 are representative of streamlines for other values of F_s , Re , L/D_h , and Z_c .

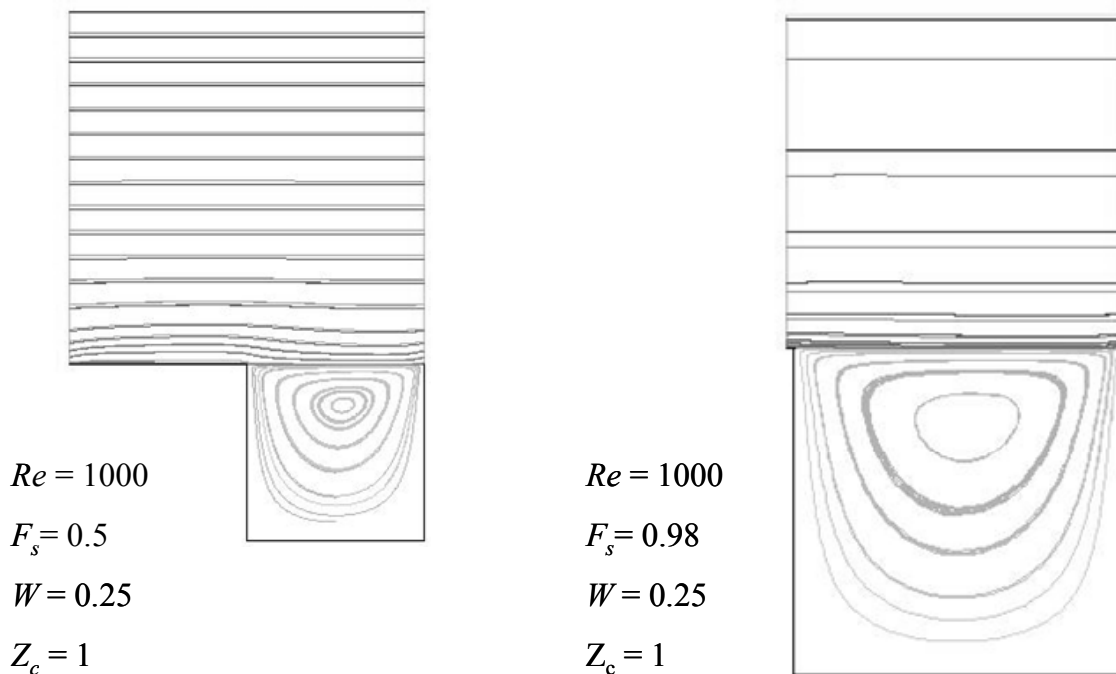


Figure 3.4: Representative streamlines for two different scenarios.

3.2.2 Streamwise-Velocity Field Behavior

Streamlines are useful in showing the path of the fluid, but they are insufficient to illustrate the velocities of the fluid at different locations. This section displays results showing how geometric parameters and the Reynolds number affect the streamwise-velocity of the fluid. In order to understand how the velocity changes throughout the geometry it must first be explained how the results are presented. All of the velocities presented here will be compared to a classical fully-developed laminar parallel plate channel flow shown qualitatively in Fig. 3.5.

If the velocity profile shown in Fig. 3.5 is nondimensionalized by the maximum centerline velocity in the classical solution (u_{mc}) and the position is nondimensionalized by $H/2$ then the velocity profile shown in Fig. 3.6 is obtained. Notice that by taking advantage of symmetry only the lower half of the channel need be shown. The range of both u/u_{mc} (or u^*) and $2y/H$ (or y^*) is 0 to 1. For laminar, periodically fully-developed flow, all comparisons of the axial velocity will be made against this benchmark, regardless of the Reynolds number and axial position in the repeating channel module.

The axial velocity behavior for the ultrahydrophobic cases will be nondimensionalized by the same parameters as the corresponding classical case for meaningful comparisons. This form of nondimensionalization also makes it possible to compare flows for channels that have different geometries (i.e., L/D_h) and Reynolds numbers, because all data will be displayed on the same scale.

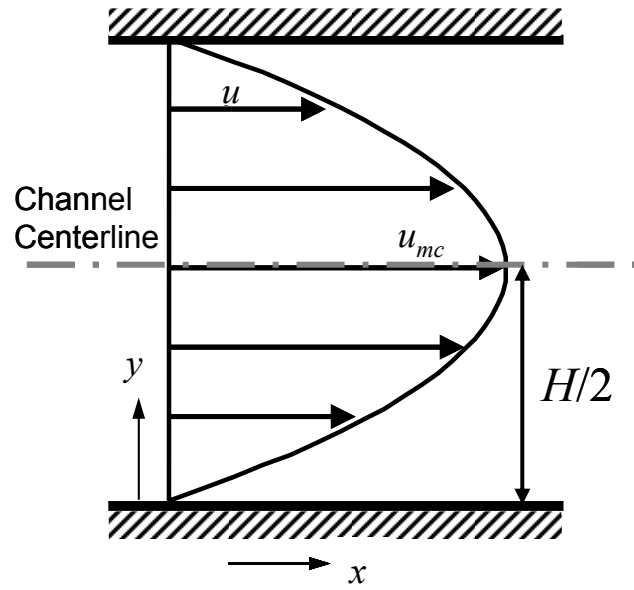


Figure 3.5: Velocity profile of a classical fully-developed laminar channel flow.

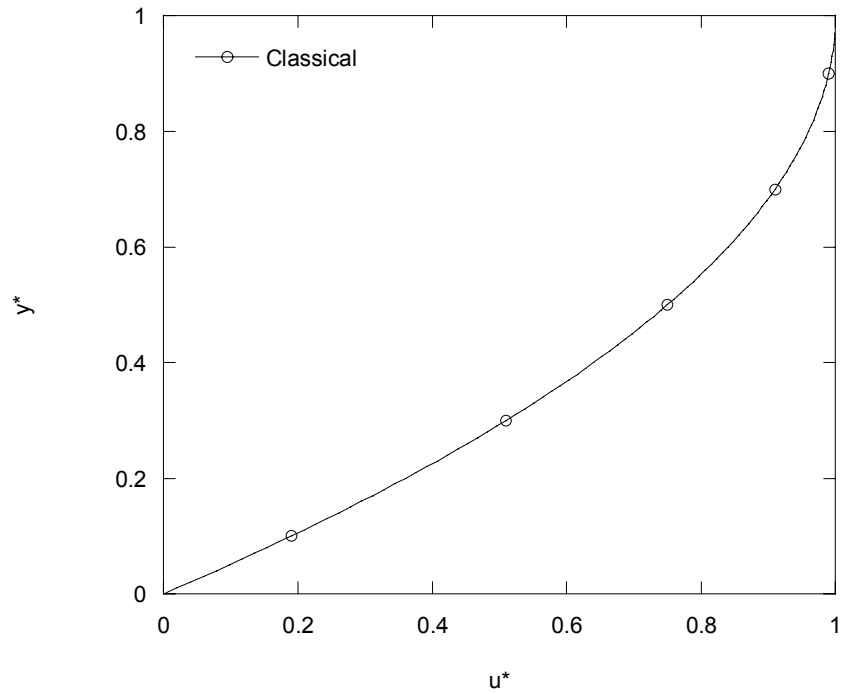


Figure 3.6: Nondimensionalized velocity profile in a fully-developed classical channel flow.

Also important in displaying the results is identifying how different locations along the channel are described. The x -location will be specified using a percentage of the repeated module length, for example $x/L = 0$ would indicate an x -location at the inlet of the repeating module, while $x/L = 0.50$ would indicate an x -location at half the distance of the repeated module length. This is illustrated in Fig. 3.7. As was mentioned before when the air cavity is included in the model the data is reported as “AC” and when the interface above the cavity is modeled as shear-free the data is labeled as “SF”.

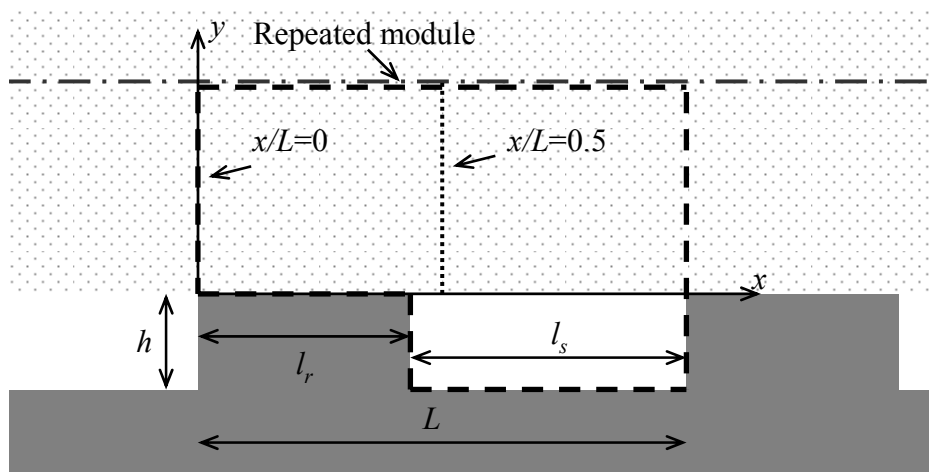


Figure 3.7: Schematic showing percentage of repeated module used in reporting velocity data.

Shown in Fig. 3.8 are velocity profile behavior for a (SF) case where $F_s=0.5$, $L/D_h = 0.25$, and $Re=1000$. It can be seen that the velocity magnitude at all x/L locations appears to be unchanging far from the wall. Indeed for $y^* > 0.1$ the profiles look similar. Also the centerline velocity of the (SF) model is slightly smaller ($\sim 3\%$ less) than that of the classical case. A smaller velocity at the centerline would be expected because the

ultrahydrophobic surface allows an apparent slip at the channel wall. In order for continuity to hold, with greater axial velocity near the channel wall, there must therefore be less fluid velocity at the centerline.

Fig. 3.8 shows that the velocity profiles for the different x/L locations deviate from each other near the wall of the channel. Fig. 3.9 shows a close-up of the near-wall region. For the rib region ($0 < x/L < 0.50$) the velocity profiles look very similar and

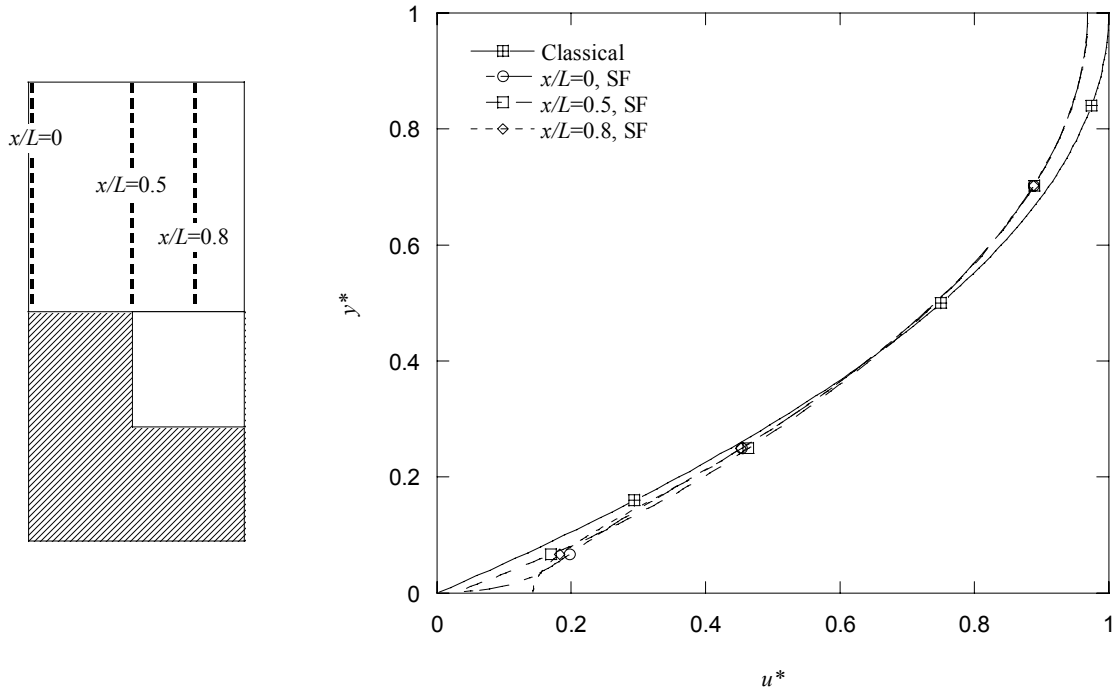


Figure 3.8: Velocity profile predictions for a (SF) case where $F_s = 0.5$, $L/D_h = 0.25$, and $Re = 1000$ compared with a classical fully-developed channel flow.

each has a velocity at the wall of zero. Right at $x/L = 0$, (the start of the rib) the velocity shows a distinct difference from the other locations above the rib. The difference is due to the fluid in the near wall region with higher approaching momentum, since it has just

come from a no-shear region. When the fluid enters the rib region the velocity at the wall must vanish, but momentum still exists in the fluid in the near wall region. It takes some streamwise distance for viscous diffusion to slow the fluid (by approximately $x/L=0.10$ in this case).

In the cavity region ($0.50 < x/L < 1.0$) the results show that as x/L increases the velocity at the boundary increases, as expected. Notice that the velocity gradient with respect to the y -direction is zero ($du/dy = 0$) from the no-shear boundary condition. Following the rib (where the velocity at the wall was zero) the no-shear boundary condition allows the fluid to accelerate and the fluid axial momentum to be redistributed.

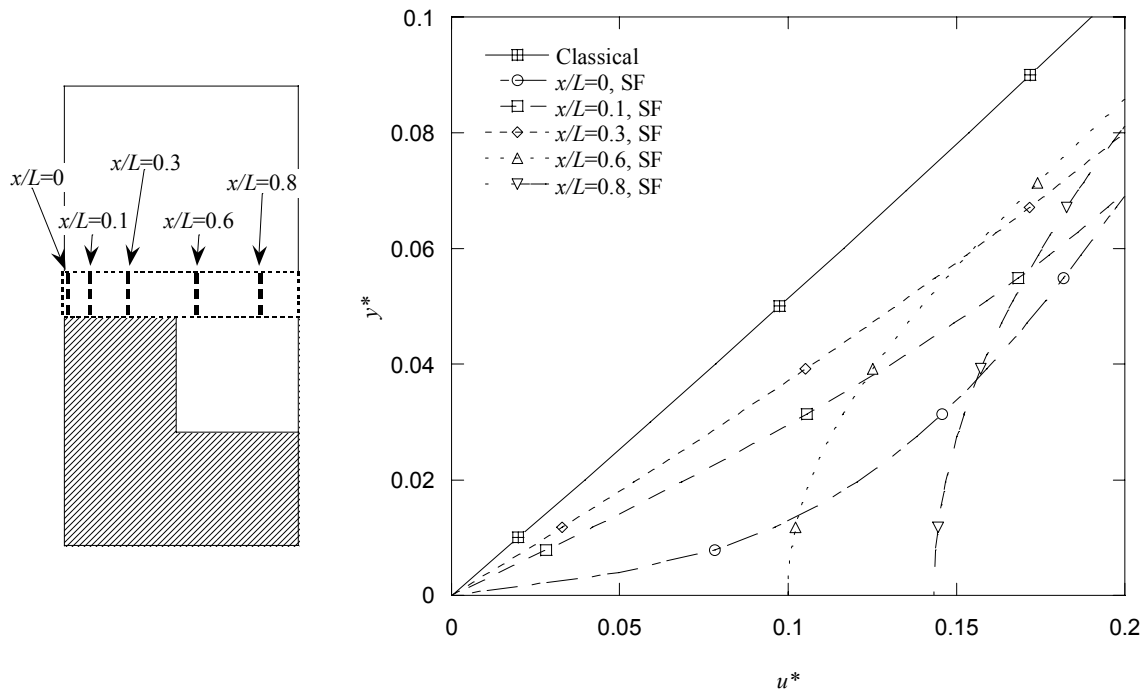


Figure 3.9: Near-wall velocity profile predictions for a (SF) case where $F_s=0.5$, $L/D_h=0.25$, and $Re=1000$ compared with a classical fully-developed channel flow.

For the (AC) model, when the cavity region is included in the model, the velocity profiles that result are very similar to those shown above with only minor differences in the region near the wall and interface observed. Figure 3.10 shows a near-wall

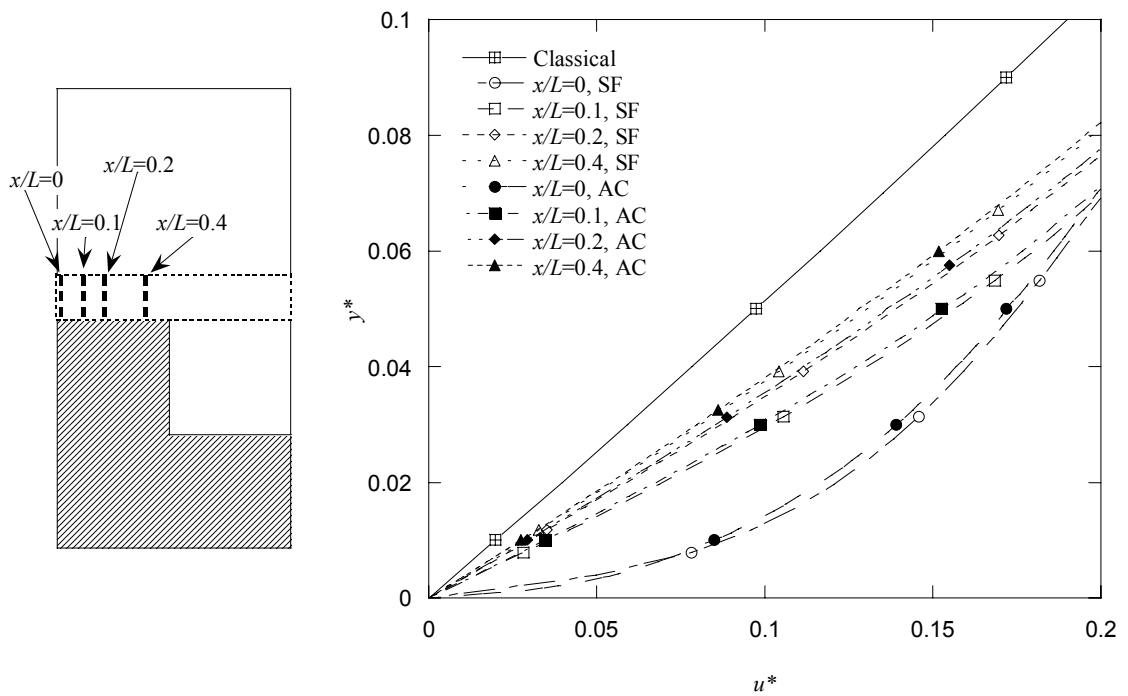


Figure 3.10: Near-wall comparison of velocity profile predictions in the rib region for a (SF) case where $F_s=0.5$, $L/D_h=0.25$, and $Re=1000$ and a (AC) case where $F_s=0.5$, $L/D_h=0.25$, $Re=1000$, and $Z_c=1$; both also compared to a classical fully-developed channel flow.

comparison between the (AC) and (SF) models for the same conditions ($F_s=0.5$, $L/D_h=0.25$, $Re=1000$, and $Z_c=1$ for (AC)) above the rib region ($0 < x/L < 0.50$), while Fig. 3.11 shows the near-wall comparison above the cavity region ($0.50 < x/L < 1.0$). The stream-wise velocity comparisons between the (AC) and (SF) cases show only slight differences

(2-4% difference in u^*) and confirms that approximating the boundary to be full slip is a good approximation for $F_s=0.5$, $L/D_h=0.25$, $Re=1000$, and $Z_c=1$ for (AC). Although Figs. 3.9 and 3.10 are very similar, there is a small difference in the velocity distributions, arising because the air cavity is included in the model. There will be some shear stress at the liquid-vapor interface and this will slow the fluid down slightly. This is why the velocity profiles derived using the (AC) model are smaller than the velocity profiles derived using the (SF) model.

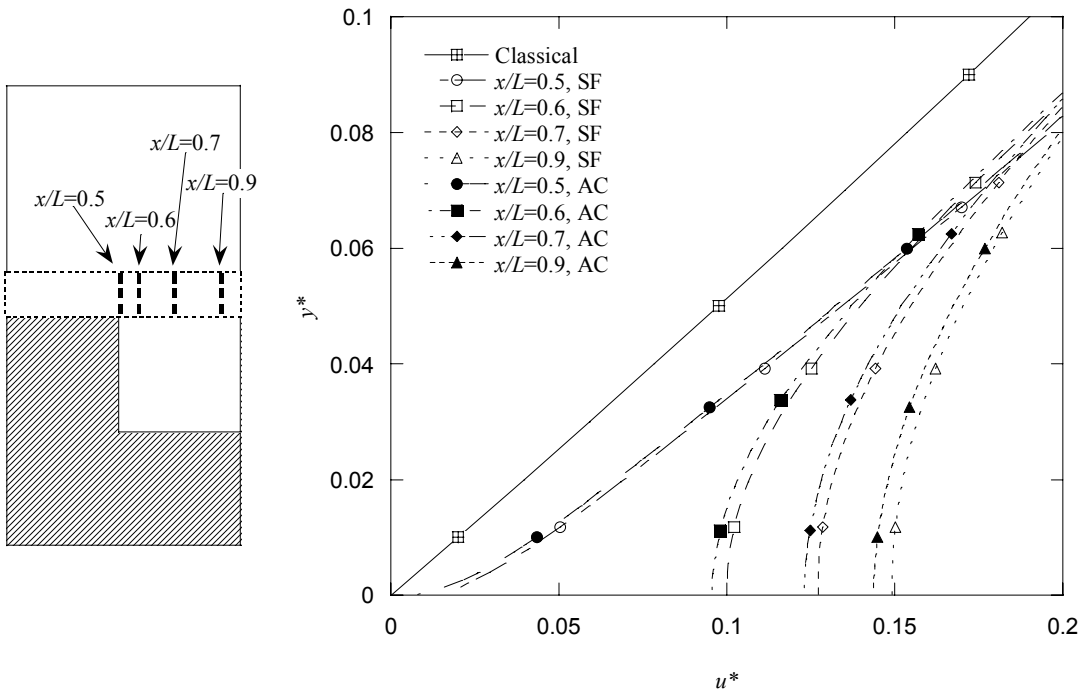


Figure 3.11: Near-wall comparison of velocity profile predictions in the cavity region for a (SF) case where $F_s=0.5$, $L/D_h=0.25$, and $Re=1000$ and a (AC) case where $F_s=0.5$, $L/D_h=0.25$, $Re=1000$, and $Z_c=1$; both also compared to a classical fully-developed channel flow .

As the slip fraction increases the differences between the (SF) model and the (AC) model become more apparent. This is illustrated below in Fig. 3.12 where the channel that is

modeled has $F_s=0.98$, $L/D_h=0.25$, $Re=1000$, and $Z_c=1$ for the (AC) model. When Fig. 3.12 is compared to Fig. 3.8 it can be seen how dramatically the size of the slip fraction length can affect the velocity profile in the channel. Instead of a 3% reduction in velocity at the channel centerline shown in Fig. 3.8 where $F_s=0.5$, here there are reductions of 17% and 16% for the (SF) case and the (AC) cases, respectively. Not only is the centerline velocity reduced, but the shape of the curve has become more similar to a classical time averaged velocity profile for a turbulent channel flow. Again, the reduction of velocity at the centerline occurs because the fluid is on average flowing faster near the wall and in order for the mass flow rate to be the same this increase in velocity near the wall is balanced by a decrease in velocity at the centerline.

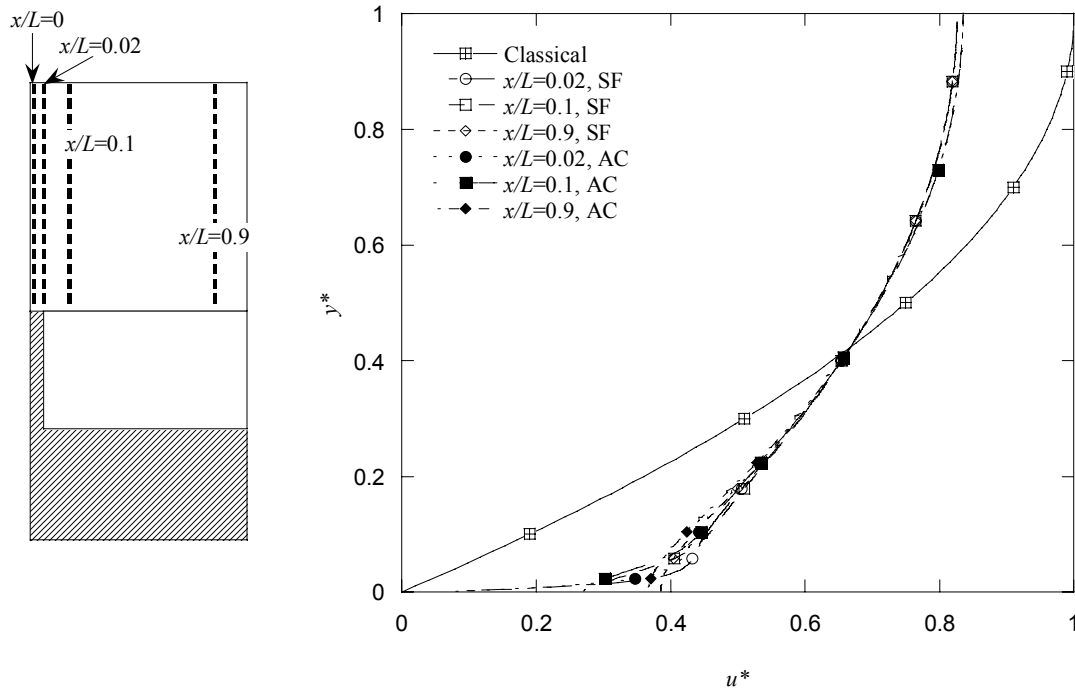


Figure 3.12: Velocity profile predictions for a (SF) case where $F_s=0.98$, $L/D_h=0.25$, and $Re=1000$ and a (AC) case where $F_s=0.98$, $L/D_h=0.25$, $Re=1000$, and $Z_c=1$; both also compared to a classical fully-developed channel flow.

Zooming into the near-wall region and examining the profiles located above the cavity region the differences between the (AC) and (SF) model can be analyzed more closely (see Fig. 3.13). As expected higher velocities are shown with the (SF) model since there is no resistance to the liquid flow at the no-shear interface. The velocity difference between the two different models is slightly more pronounced in this scenario. Before, where $F_s = 0.5$, the interface velocity difference between the two models was at a maximum 4% different, while in this case where $F_s=0.98$ the difference in interface velocity between the two models is as high as 5.5%.

Not only does the model utilized (AC vs. SF) have an effect on the velocity profile, but each of the parameters, L/D_h , Re , and Z_c affect the flow field and thus velocity profiles as well. Figure 3.13 illustrates how the normalized streamwise velocity profiles change when the Reynolds number is decreased from $Re=1000$ (inertial range) to $Re=0.4$ (creeping flow) for a case where $F_s = 0.5$. The figure shows the near-wall region where the differences are most apparent. Clearly, the creeping flow Reynolds number case shows that the ultrahydrophobic surfaces have a more pronounced influence on the resulting flow field. The dimensionless velocity above the cavity region has a significantly larger magnitude (more apparent slip) for $Re = 0.4$. This occurs because at a lower Reynolds number fluid inertia is less important and the flow is able to more easily adjust to the cavity region. This trend is similar for other geometries. For example, if a similar comparison was made for $F_s=0.98$ it would be seen that at the lower Reynolds number a greater dimensionless velocity in the cavity region exists. Another interesting

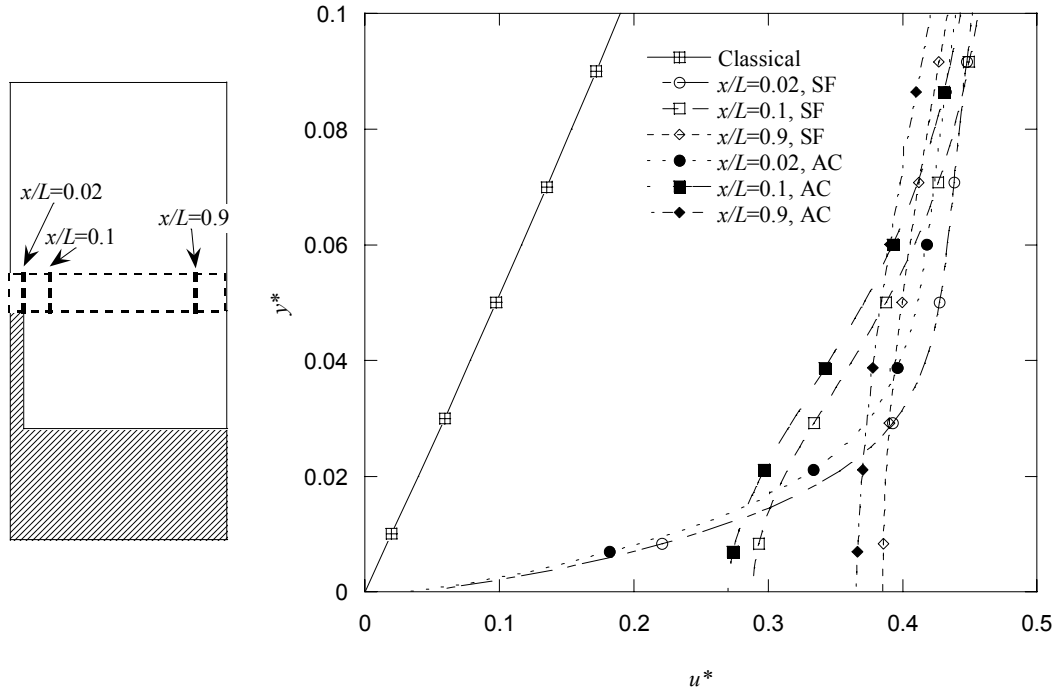


Figure 3.13: Near-wall region of velocity profile predictions above the cavity region for a (SF) case where $F_s=0.98$, $L/D_h=0.25$, and $Re=1000$ and a (AC) case where $F_s=0.98$, $L/D_h=0.25$, $Re=1000$, and $Z_c=1$; both also compared to a classical fully-developed channel flow .

observation for low Reynolds number flow is that the velocity profiles are symmetric in the streamwise direction (i.e., the velocity field for $0.5 < x/L < 0.75$ is a mirror image of the velocity field for $0.75 < x/L < 1$) this is characteristic of low Re flow and results since inertia effects are negligible.

Figure 3.14 shows how L/D_h , the normalized microrib/cavity module length, affects the velocity profiles when it is changed from $L/D_h=0.25$ (surfaces close together relative to the module length) to $L/D_h=0.05$ (surfaces are far from each other relative to the module length). More data will be presented on this later, but when the value of L/D_h is decreased (the channel walls are moved farther apart), the ultrahydrophobic surfaces have less effect on the flow. This is seen in the figure below; the velocity profiles above

the cavity region for the case of $L/D_h = 0.05$ are more nearly like the velocity profile for the classical no-slip wall case. This results because the ratio of the wall area to total flow cross-sectional area has decreased (for the volume of fluid flowing there is less wall area affecting it). It is important to point out that this trend is observed for all other slip fractions, F_s , as well.

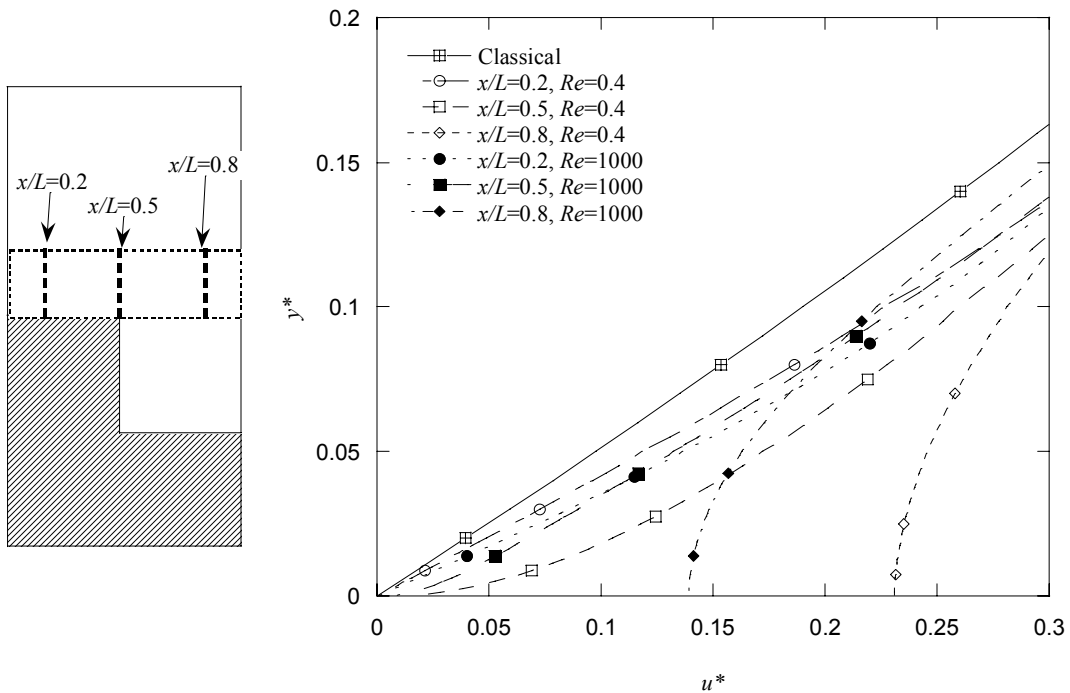


Figure 3.14: Near-wall region of velocity profile predictions above the cavity region for a (AC) case where $F_s=0.5$, $L/D_h = 0.25$, $Re=1000$, and $Z_c=1$ and a (AC) case where $F_s=0.5$, $L/D_h = 0.25$, $Re=0.4$, and $Z_c=1$ compared with a classical fully-developed channel flow.

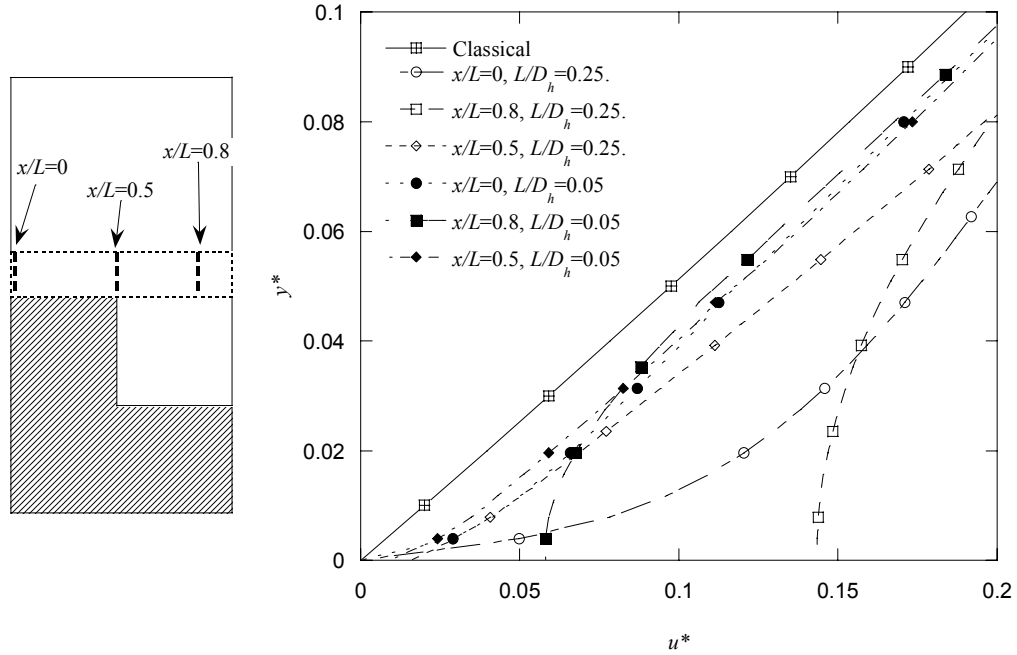


Figure 3.15: Near-wall velocity profile predictions for a (SF) case where $F_s=0.5$, $L/D_h=0.25$, and $Re=1000$ and a (SF) case where $F_s=0.5$, $L/D_h=0.05$, and $Re=1000$.

3.2.3 Interface and Centerline Velocity Behavior

In the previous subsection, the impact of ultrahydrophobic walls on the streamwise-velocity was illustrated by displaying velocities at different x/L locations. This subsection shows how the velocity changes in the x -direction at two different locations, $y^*=0$ and $y^*=1$, corresponding to the interface and the centerline respectively, for a wide range of parameters. Fig. 3.16 illustrates the location of these positions.

The interface velocities for several different scenarios are shown in Fig. 3.17. The effects on the interface velocity can be seen in this figure for each parameter (F_s , L/D_h , Z_c , Re , and the model AC vs. SF). For $F_s=0.5$, $L/D_h=0.25$, $Z_c=2$, and $Re=1000$, the interface velocity change is small (approximately 1.5% error) when comparing the two different models, (AC) vs. (SF). On the other hand, when $F_s=0.98$, $L/D_h=0.25$, $Z_c=2$, and

$Re=1000$, the difference in interface velocity between the two models becomes more apparent (approximately 6% difference). More error occurs for $F_s=0.98$ between a (AC) and a (SF) case because there is more apparent surface area over which the model is important, (i.e., more air in contact with the water to decelerate the fluid).

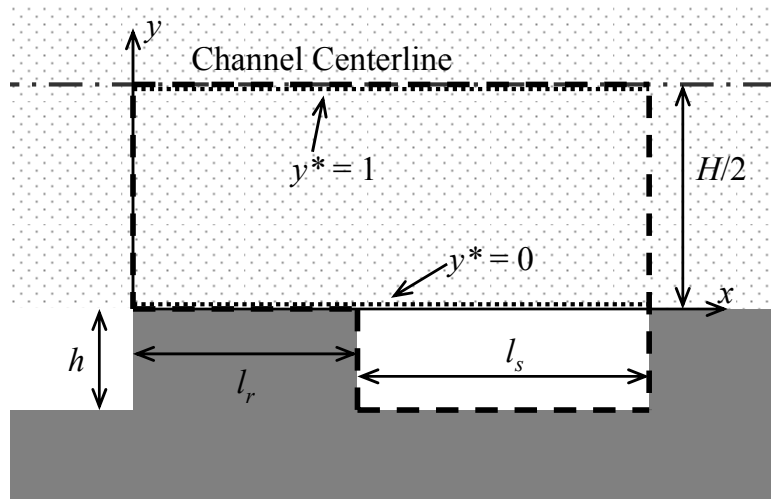


Figure 3.16: Schematic illustrating the interface position ($y^*=0$) and the centerline position ($y^*=1$).

It can be seen how changes in F_s affects the interface velocity, here, when comparing $F_s=0.5$ to $F_s=0.982$ with $L/D_h = 0.25$, $Z_c=2$, and $Re=1000$, the interface velocity above the cavity is more than twice the magnitude for the $F_s=0.98$ scenario. The increase in interface velocity is due to the fact that there is more slip surface for $F_s=0.98$ and the solid rib has less of a retarding effect. Also shown in the figure is the influence that Re exercises. A comparison of $Re=0.4$ with $Re=1000$ for $F_s=0.98$ for $L/D_h = 0.25$, $Z_c=2$, shows that a lower Re tends to increase the velocity above the cavity. Symmetry above the cavity region becomes more apparent for the low Re case, where the nonlinear

terms of the x -momentum equation have a smaller impact. The higher Re scenario shows a skewed profile caused by the significance of the momentum of the fluid. After passing the rib it takes some distance above the cavity for the velocity to gain momentum.

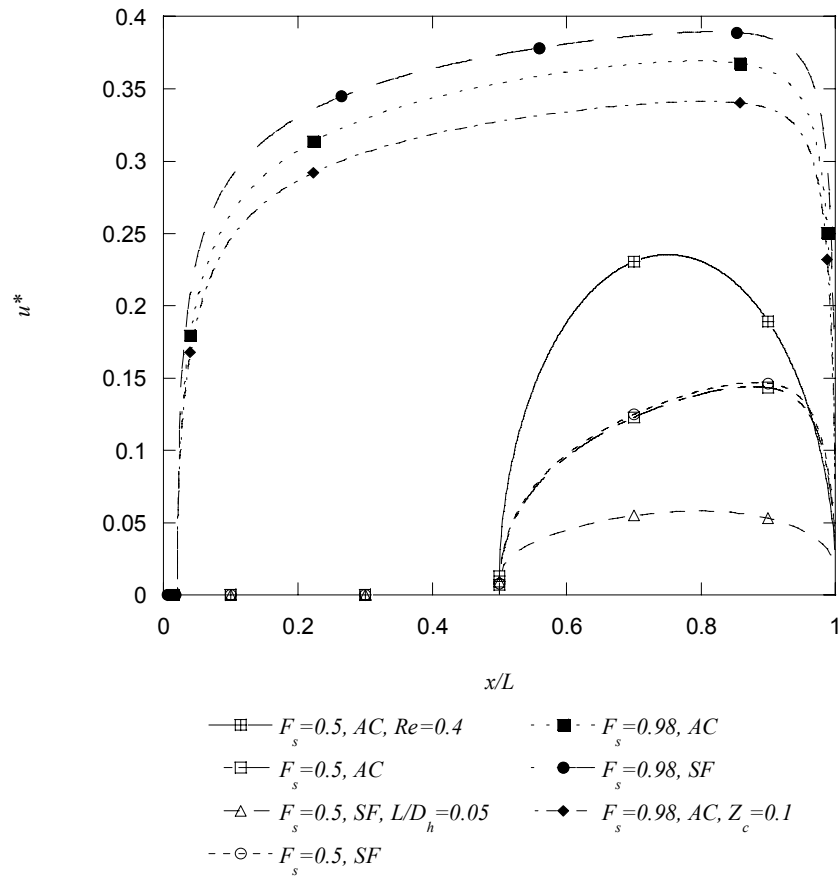


Figure 3.17: Interface ($y^*=0$) velocities in the x -direction for many scenarios, unless otherwise specified in the legend $Re=1000$, $Z_c=2$, and $L/D_h=0.25$.

Finally the effects of L/D_h and Z_c are shown in Fig. 3.17. Here, two scenarios where $F_s=0.5$, $Z_c=2$, and $Re=1000$ are compared; $L/D_h=0.05$ in one case and $L/D_h=0.25$

in the other. Decreasing L/D_h causes the interface velocity to decrease significantly and also to become more symmetric even though Re is the same. This occurs because the apparent fractional surface area to fluid volume ratio is decreasing.

The effect of the cavity depth, Z_c , is shown for $Z_c=2$ and $Z_c=0.1$ with $F_s=0.98$, $L/D_h=0.25$, and $Re=1000$ for both cases. Decreasing Z_c causes the velocity above the cavity at the interface to decrease. As Z_c becomes smaller the interface surface is closer to the bottom wall of the cavity. In the cavity the air is circulating and when the cavity becomes shallower, there is a larger velocity gradient, which causes more shear stress and therefore reduces the interface velocity.

Figure 3.17 is descriptive and illustrates what happens to the interface velocity profile when one parameter is changed from case to case. In order to get a broader understanding of how the interface velocity is affected by each parameter (F_s , L/D_h , Z_c , and Re) the maximum interface velocity, u^*_{im} , will be displayed for many unique individual cases. u^*_{im} represents the maximum velocity of the liquid at $y^*=0$ normalized by the centerline velocity in the laminar classical channel flow case, u_{mc} . This is important in showing the parametric effect and will be useful in displaying most of the scenarios that were studied.

Shown in Fig. 3.18 are predictions of the maximum interface velocity u^*_{im} for four different values of L/D_h ranging from 0.083 to 2.5. Each prediction is shown with an individual data point. These predictions were obtained at $Re=1000$ and using the (SF) model. This figure illustrates that as F_s decreases u^*_{im} decreases at approximately the same rate depending on the value of L/D_h . Also shown in Fig. 3.19 are trend lines and predictions of u^*_{im} vs. L/D_h for three slip fractions, $F_s = 0.5, 0.875, \text{ and } 0.98$.

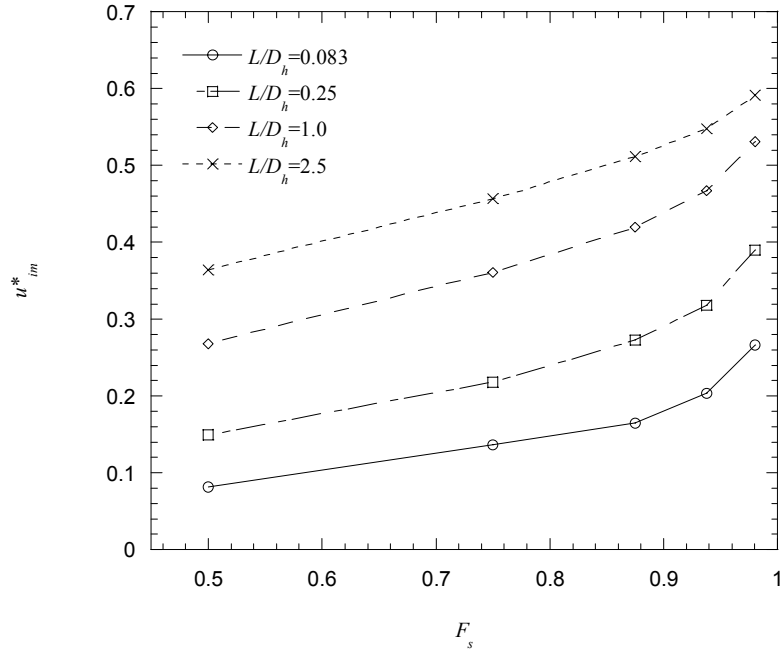


Figure 3.18: Maximum dimensionless interface velocity (u^*_{im}) along the interface ($y^*=0$) vs. F_s for four relative rib/cavity module sizes and at $Re=1000$ for a (SF) model.

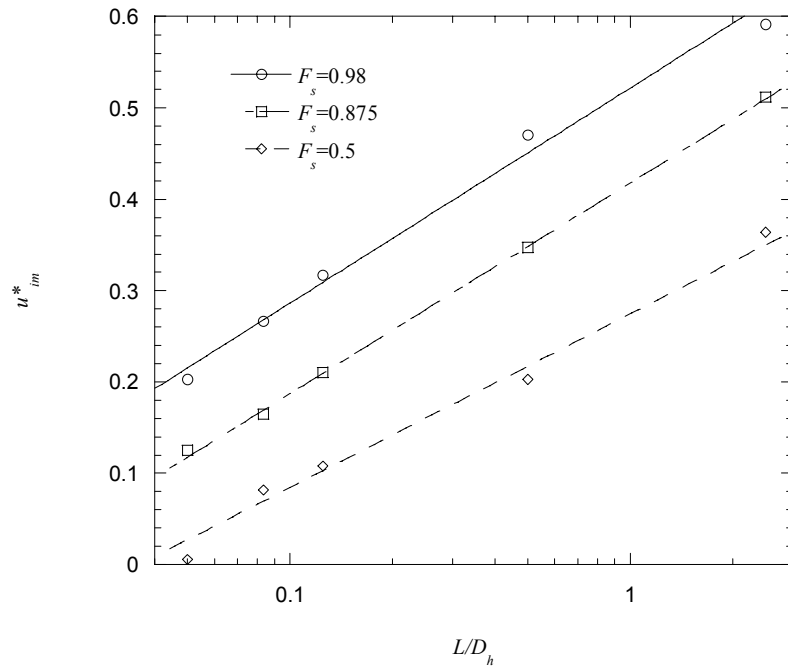


Figure 3.19: Maximum dimensionless interface velocity (u^*_{im}) along the interface ($y^*=0$) vs. L/D_h for $F_s=0.98, 0.875,$ and 0.5 and at $Re=1000$ for a (SF) model.

For all scenarios as L/D_h decreases, u^*_{im} approaches zero. This occurs because the volume to surface area has increased and the wall has less of an effect on the motion of the fluid. Also for all scenarios as F_s approaches zero the interface u^*_{im} approaches zero too. This occurs because an decrease in the slip fraction increases the solid-liquid interfacial contact area.

Shown in Fig. 3.20 are predictions of the interface velocity u^*_{im} plotted for cases exhibiting different values of Z_c to illustrate the influence exerted by the relative air cavity size. Also, shown in the figure are the (SF) results to illustrate the comparison between the two different models. u^*_{im} does not show strong dependence on cavity depth, Z_c . It increases slightly with increasing Z_c up to about $Z_c=0.5$, where it levels off to a constant value. The constant value is dependent on F_s , L/D_h , and Re . For $F_s=0.5$ the predictions of u^*_{im} from the (SF) model have an 8% difference from the (AC) model at low values of Z_c and level off at 2% difference as Z_c increases. The difference is larger for $F_s=0.98$, at low values of Z_c the difference in the (SF) model is 14% higher than the (AC) model and the difference levels off at 5.5% for large values of Z_c . The (SF) model underpredicts the maximum interface velocity, and more closely approximates the (AC) model for small values of F_s .

The effect of Re on the maximum interface velocity u^*_{im} is shown in Fig. 3.21 for $F_s=0.98$ and 0.5. The figure shows that as the Re increases the maximum interface velocity u^*_{im} decreases. This result is expected because at higher Re the influence of momentum forces are dominant and the influence of the boundary is lessened.

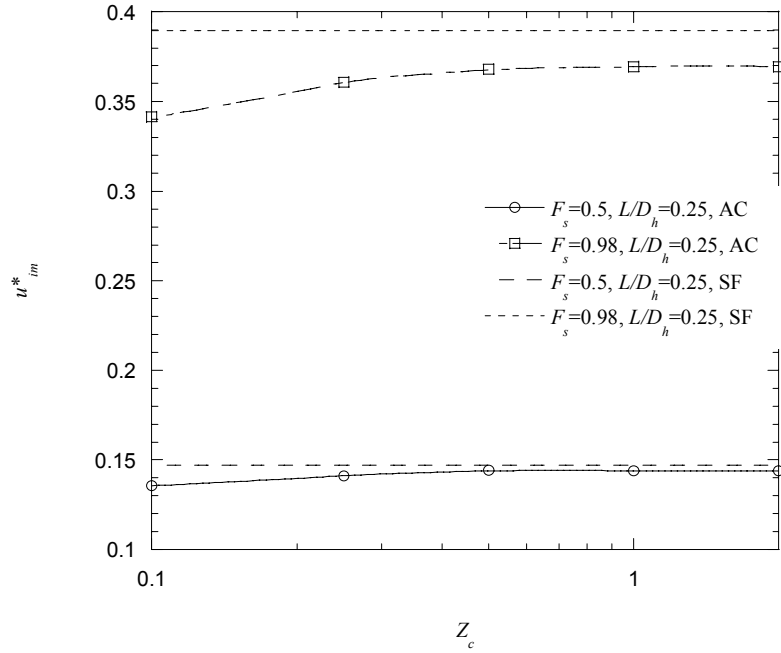


Figure 3.20: Maximum dimensionless interface velocity (u^*_{im}) along the interface ($y^*=0$) vs. Z_c for $F_s=0.98$ and 0.5 , where $Re=1000$, and $L/D_h=0.25$ for both a (AC) and a (SF) model.

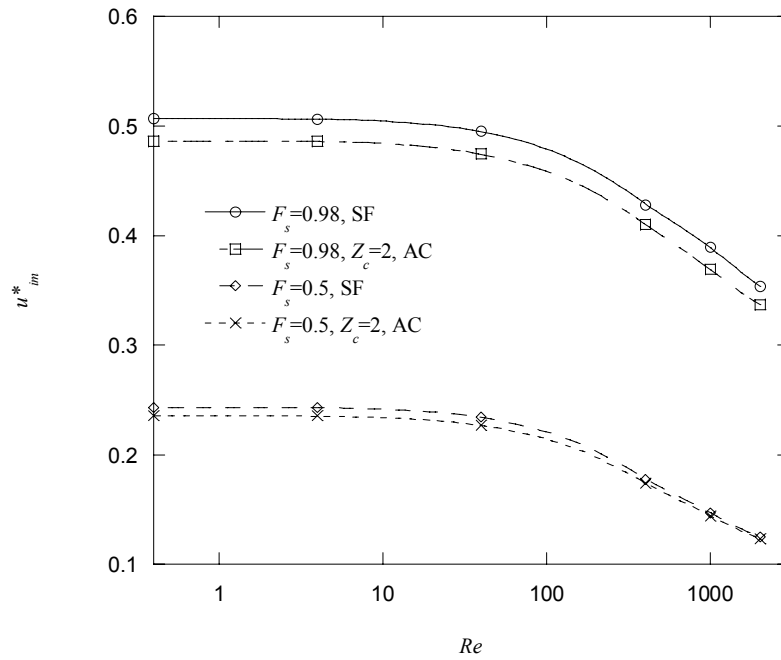


Figure 3.21: Maximum dimensionless interface velocity (u^*_{im}) along the interface ($y^*=0$) vs. Re for $Z_c=2$ for $F_s=0.98$ and 0.5 , where $Re=1000$, and $L/D_h=0.25$ for both a (AC) and a (SF) model.

The normalized centerline ($y^*=1$) velocity, u^*_{cl} , behavior for each of the cases discussed and shown in Fig. 3.17 is shown in Fig. 3.22. In this figure the normalized centerline velocity, u^*_{cl} , is plotted versus the streamwise direction. When comparing Fig. 3.16 and 3.22, each case that had a higher average interface velocity corresponds to a lower average centerline velocity. This result occurs because mass was conserved. The normalized centerline velocity remains relatively constant at different streamwise locations of the channel.

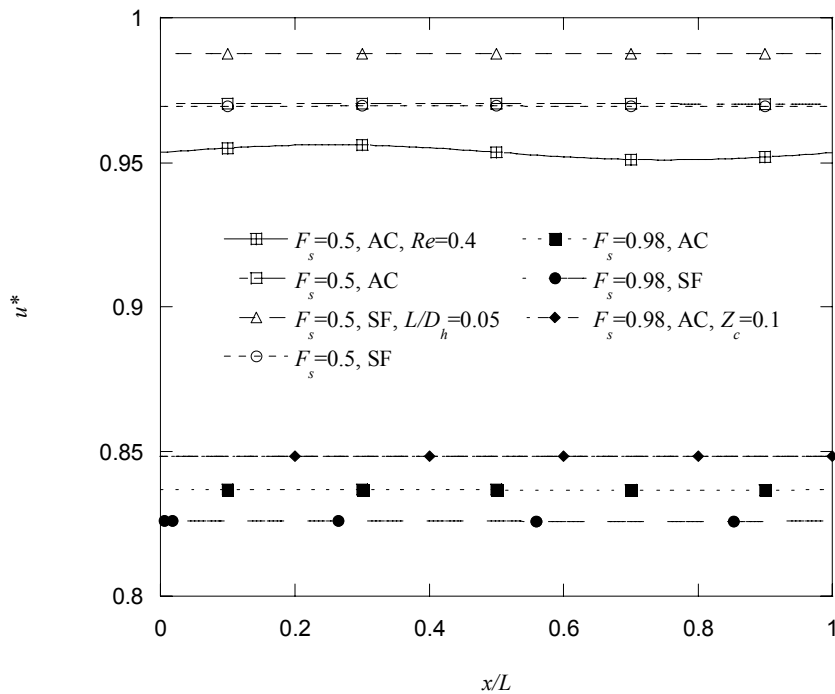


Figure 3.22: Dimensionless centerline ($y^*=1$) velocities in the x -direction for many scenarios, unless otherwise specified in the legend $Re=1000$, $Z_c=2$, and $L/D_h=0.25$.

To illustrate more clearly how the dimensionless centerline velocity, u^*_{cl} , varies with different geometries it is plotted in Fig. 3.23 as a function of F_s for four different

relative module lengths, $L/D_h = 2.5, 1.0, 0.0625,$ and 0.05 . As the slip fraction increases the centerline velocity decreases because there is more fluid moving in the near wall region. As the relative module length increases the centerline velocity decreases. Again, large relative module lengths are representative of large surface area to volume ratios and the ultrahydrophobic surface has more of an influence on the fluid. Alternatively as the relative module length, L/D_h , decreases the centerline velocity approaches the same value as in the classical scenario, indicating that the ultrahydrophobic surface has less of an influence on the fluid.

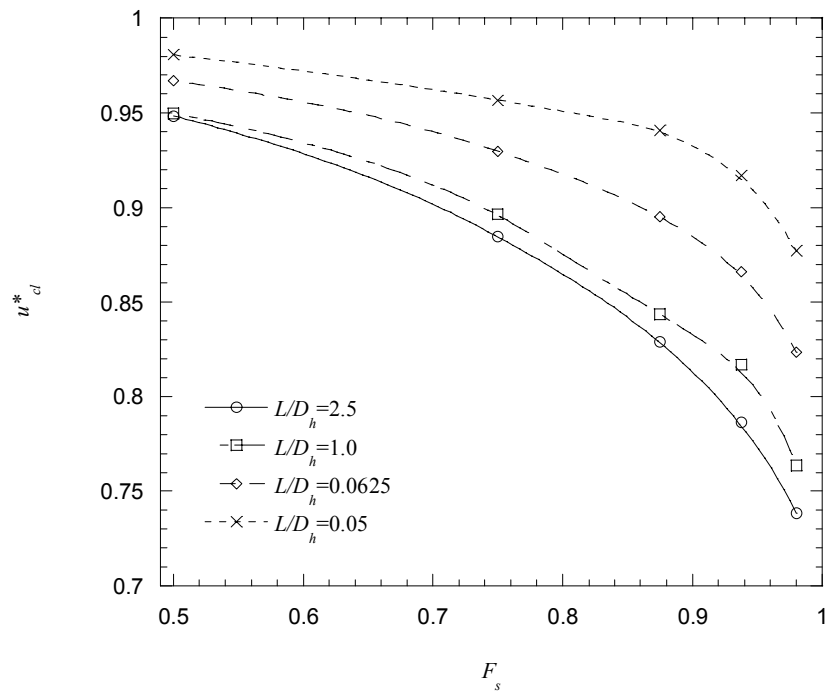


Figure 3.23: Dimensionless centerline velocity (u^*_{cl}) along the centerline ($y^*=1$) vs. F_s for four relative rib/cavity module sizes and at $Re=1000$ for a (SF) model.

Figure 3.24 illustrates the influence of the relative cavity depth, Z_c . For each scenario shown in the figure $Re=1000$ and $L/D_h=0.25$. Two slip fractions are studied $F_s=0.98$ and $F_s=0.5$. The figure shows that for $Z_c>0.5$ the influence of the relative cavity depth on the centerline velocity vanishes for $F_s=0.98$. This also shows that for $F_s=0.5$ the centerline velocity was not influenced by the value of the relative cavity depth for the cases studied. Analytical results from both the (AC) model and the (SF) model are presented and show that in all cases the (AC) model predicts faster centerline velocities. This occurs because in the (AC) model the vapor cavity will slow the fluid in the near wall region and when the fluid is slower in the near wall region it is faster in the centerline.

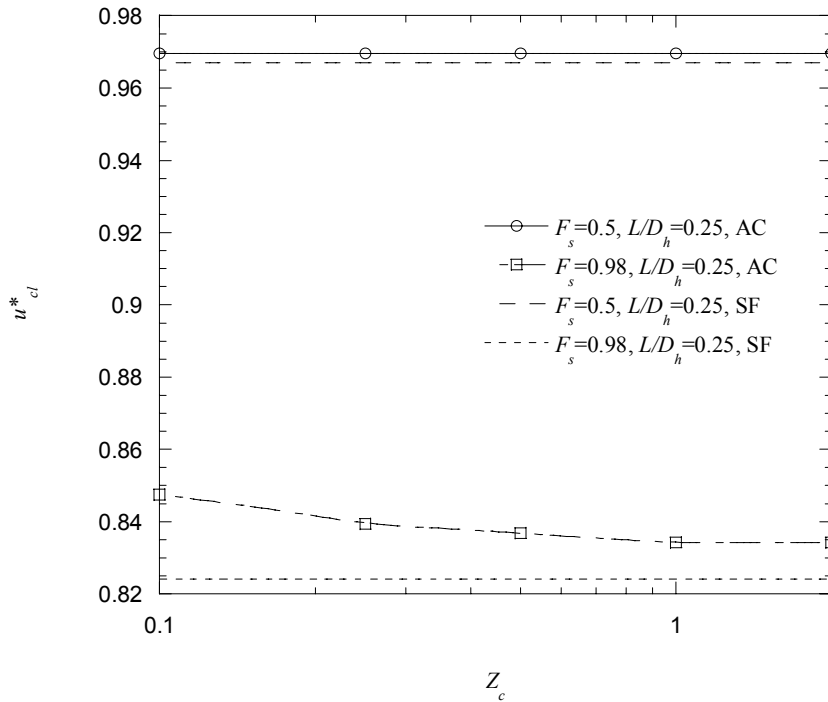


Figure 3.24: Dimensionless centerline velocity (u_{cl}^*) along the centerline ($y^*=1$) vs. Z_c for $F_s=0.98$ and 0.5 , where $Re=1000$, and $L/D_h=0.25$ for both a (AC) and a (SF) model.

The magnitude of the Reynolds number also has an influence on the centerline velocity. Figure 3.25 shows results for two slip fractions, $F_s=0.98$ and $F_s=0.5$, for Reynolds numbers ranging between 0.4 and 2000. Both the (AC) and the (SF) model are presented. For all models $L/D_h = 0.25$ and for the (AC) model $Z_c=2$. The calculations show that as Re increases the dimensionless centerline velocity increases, but for $Re < 40$ the centerline velocity is independent of Re . For $F_s=0.5$ there was no significant difference in the centerline velocity when the air cavity was modeled, but for $F_s=0.98$ there was a difference between the (AC) and (SF) models. For $F_s=0.98$ the (AC) model had centerline velocities 1.6% larger than the (SF) model.

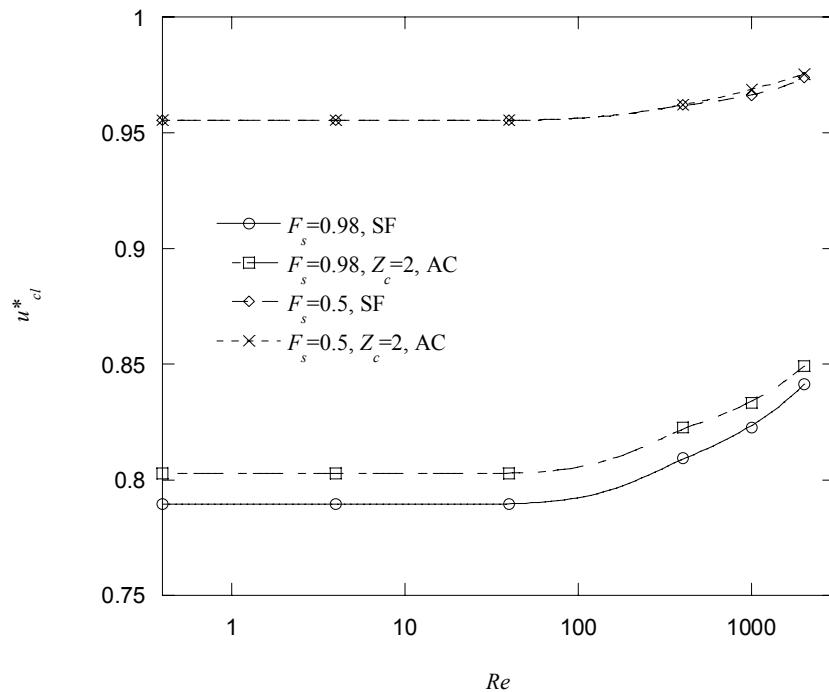


Figure 3.25: Dimensionless centerline velocity (u_{cl}^*) along the centerline ($y^*=1$) vs. Re for $Z_c=2$ for $F_s=0.98$ and 0.5, and $L/D_h = 0.25$ for both a (AC) and a (SF) model.

The details shown in the centerline and interface streamwise velocity calculations will assist in understanding the trends associated with drag reduction for microengineered ultrahydrophobic surfaces.

3.2.4 Wall-normal Velocity Behavior

In classical fully-developed laminar parallel plate flow the wall-normal component of velocity vanishes. However, when ultrahydrophobic surfaces are present it does exist. In the previous subsection (3.2.1) the x -velocity profiles from ultrahydrophobic channels showed variations of the streamwise-velocity in the near-wall region. For a flow that is incompressible, this can only happen if there is fluid motion in the wall-normal direction, to satisfy the equation of continuity (3.4). Figure 3.26 shows the normalized wall-normal component of velocity ($v^*=v/u_{mc}$) at ten different x/L locations for a case where $F_s=0.5$, $Re=1000$, $L/D_h=0.25$, and $Z_c = 1$. At $x/L=0$, just after fluid has moved past the cavity region and above the rib region, the wall-normal velocity is positive in the near wall region and decreases to zero far from the wall. Further downstream the magnitude of the wall-normal velocity decreases in the near wall region. When the fluid moves over the cavity region ($x/L=0.5$) there exists a negative wall-normal velocity. The magnitude of the negative wall-normal velocity decreases further downstream.

At the entrance to the cavity region, where the fluid near the wall is accelerating in the streamwise direction, the wall-normal velocity is negative (i.e., fluid is moving towards the wall from the channel core). In order for the streamwise-component of velocity to accelerate, fluid in the near-wall region must be replaced. As the next rib is

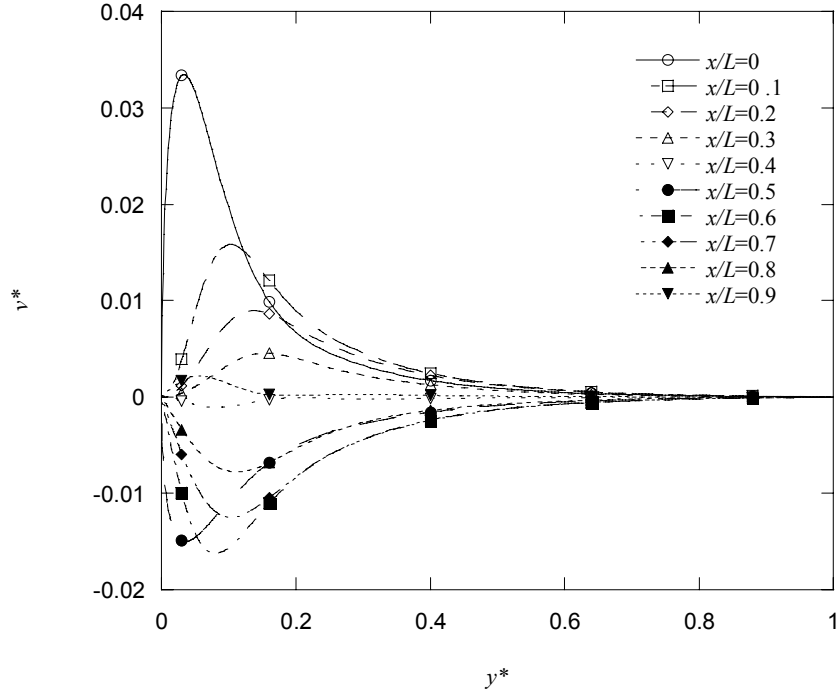


Figure 3.26: Wall-normal velocity profile predictions for a (AC) case where $F_s=0.5$, $L/D_h=0.25$, $Z_c=2$, and $Re=1000$.

approached, where the streamwise-velocity decelerates, there exists a positive wall-normal velocity. The results for all other cases show similar behavior. The magnitude of the wall-normal velocity is relatively small; this figure shows the maximum wall-normal velocity being 3% of u_{mc} . As expected, the wall-normal velocity vanishes far from the wall for all scenarios.

3.2.5 Shear Stress Predictions for Rib Surface and Liquid-Gas Interface

Predictions of the normalized wall shear stress are shown in Fig. 3.27. The results, shown as a ratio of local shear stress (τ_w) to that for a classical laminar channel flow ($\tau_{w\text{ classical}}$), reveal as expected that the location where the shear stress is highest is at

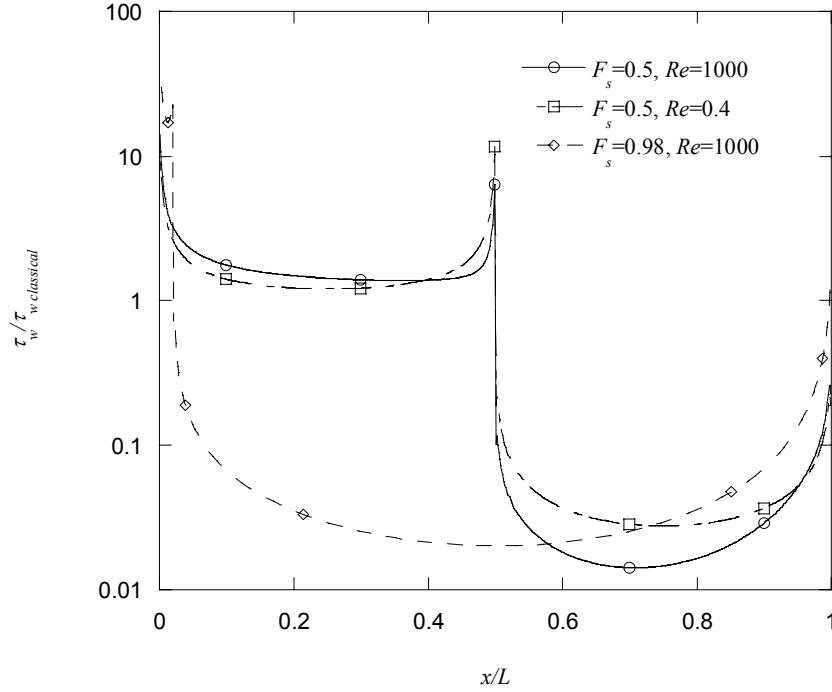


Figure 3.27: Shear stress predictions for (AC) cases where $F_s=0.5$, $L/D_h=0.25$, and $Re=1000$; $F_s=0.5$, $L/D_h=0.25$, and $Re=0.4$; and $F_s=0.98$, $L/D_h=0.25$, and $Re=1000$.

the leading edge of the rib. The shear stress is highest in this region because the fluid decelerates from a finite velocity just upstream of the rib to zero at the rib, creating a very large velocity gradient. Figure 3.27 is plotted on a semi-log scale to more fully illustrate the shear stress behavior and magnitude at the liquid-vapor interface. The wall shear stress on the rib region is larger at all x/L locations compared to the shear stress on the wall in the classical case. However, the integrated influence is not sufficient to make the total pressure drop through the channel greater than for the classical case. The shear stress at the vapor-liquid interface for the $F_s=0.98$ is larger than the shear stress above the cavity region for $F_s=0.5$.

In general, as the slip fraction increases the shear stress above the rib increases. This is why, as will be shown in the next section, the drag reduction does not exhibit a

simple proportional relationship with the slip fraction. Shear stress increases as the Reynolds number increases and as the relative module length decreases. When the relative cavity depth is small ($Z_c < .5$) there is more shear stress above the cavity region than for cases with large relative cavity depths.

3.3 GENERAL RESULTS OF THE DARCY FRICTION FACTOR – REYNOLDS NUMBER PRODUCT

One of the advantages of looking at the detailed flow field and seeing how velocities change depending on certain parameters is that it helps to understand trends in the general sense (i.e., why fRe behaves the way it does when parameters are changed). In a global view, how much of an influence ultrahydrophobic surfaces have on the overall drag or pressure drop is more important. Shown in Fig. 3.28 are predictions of the fRe product as a function of the slip fraction, F_s , for five values of the relative module length, L/D_h , ranging from 0.05 to 2.5 using a (SF) model. Each data point is shown along with corresponding trend lines. Also shown in Fig. 3.29 are predictions of fRe displayed vs. L/D_h for three slip fractions, $F_s = 0.5, 0.875,$ and 0.98 . Note again that increasing F_s results in greater relative shear-free (or reduced shear) area on the microchannel wall. The Reynolds number for all predictions shown in Figs. 3.28 and 3.29 was $Re = 1000$ and it should be underlined that the simulations are dependent on Re as will be shown later. The boundary condition specified at the liquid-vapor interface for the data of Figs. 3.28 and 3.29 was the zero shear stress condition. The influence of the vapor phase on the overall fRe will be explored in a section to follow. For all scenarios as the slip fraction approaches zero, fRe approaches 96, the classical value for laminar flow in a parallel

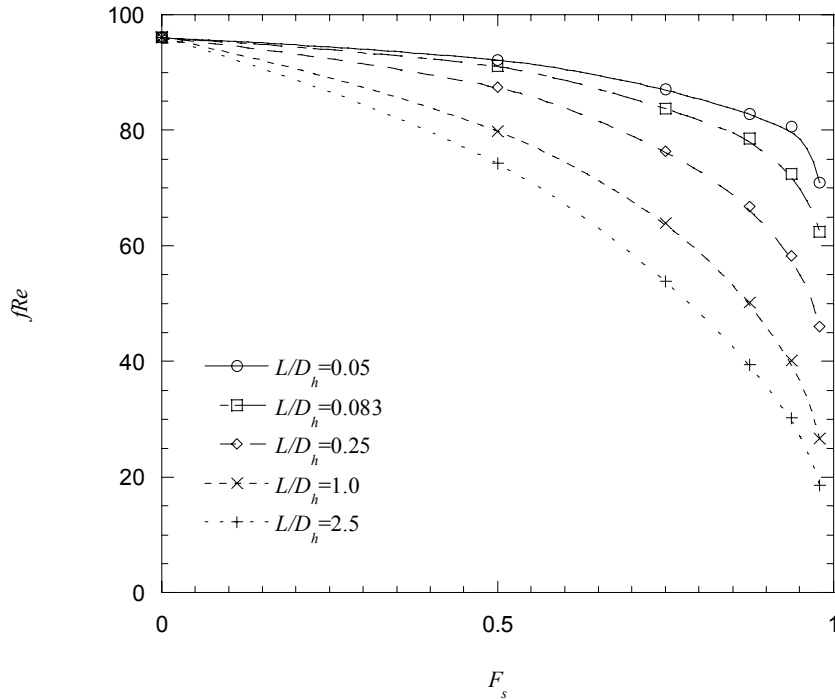


Figure 3.28: Predictions of fRe vs. F_s in a parallel plate channel with ultrahydrophobic walls and microrib/cavity structures oriented perpendicular to the flow direction for five relative rib/cavity module sizes and at $Re=1000$ (SF) model.

plate channel. As F_s increases, (as the relative size of the cavity increases with respect to the module length) the predicted value of fRe decreases monotonically as expected since the liquid-solid contact area is decreasing. As illustrated in 3.1 the average velocity is inversely proportional to fRe , and therefore, reductions in fRe may be interpreted as increases in the mass flow rate for a given applied driving pressure. The decrease in fRe is more dramatic, both in magnitude and rate of decrease, as the relative module length increases, corresponding to larger values of L/D_h . The implication is that greater reduction can be achieved for smaller microchannels where the required driving pressure would otherwise approach extreme levels. Note that a reduction in the frictional resistance as high as 80% is observed for the scenario where $F_s = 0.98$ and $L/D_h = 2.5$

(corresponding to $fRe = 19$). In practice this scenario would be realized, for example, with a microchannel of hydraulic diameter $D_h \sim 10 \mu\text{m}$ exhibiting micro-rib and cavity widths of $l_r = 0.5$ and $l_s = 25 \mu\text{m}$, respectively. By contrast a channel with the same rib/cavity dimensions but of hydraulic diameter, $D_h \sim 510 \mu\text{m}$, would yield $L/D_h = 0.05$ and a reduction in the frictional resistance of 26% is predicted (corresponding to $fRe = 71$).

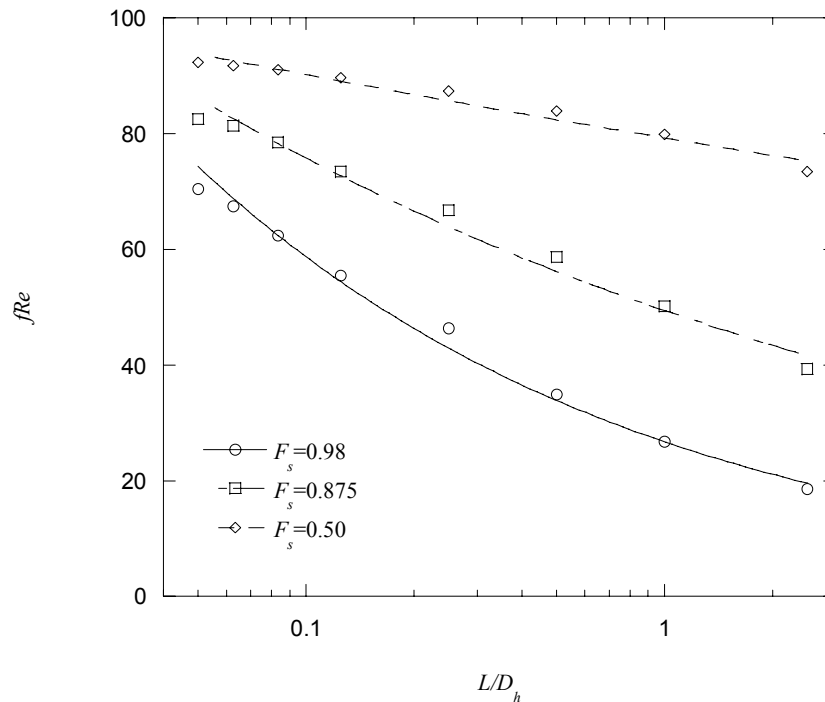


Figure 3.29: Predictions of fRe vs. relative rib/cavity module size for slip fractions of 0.98, 0.875, and 0.5 and at $Re=1000$ (SF) model.

The influence of the vapor cavity on fRe is illustrated in Fig. 3.30 where fRe is plotted as a function of the relative cavity depth, $Z_c = h/l_s$, for the $L/D_h = 0.25$ channel at

$Re = 1000$ and at two slip fractions of 0.98 and 0.5. For these scenarios the vapor space was rigorously modeled in the simulations and coupled with the liquid phase by matching the velocities and shear stresses at the liquid-vapor interface. The fRe results corresponding to the no-shear boundary condition are nominally 46 and 87 for the $F_s = 0.98$ and 0.5 cases, respectively, and are also shown on Fig. 3.30. The predictions of Fig. 3.30 reveal that the vapor cavity does exercise influence on the magnitude of fRe with a notable increase above the value of 46 for $F_s=0.98$, but exerts little effect for $F_s=0.5$.

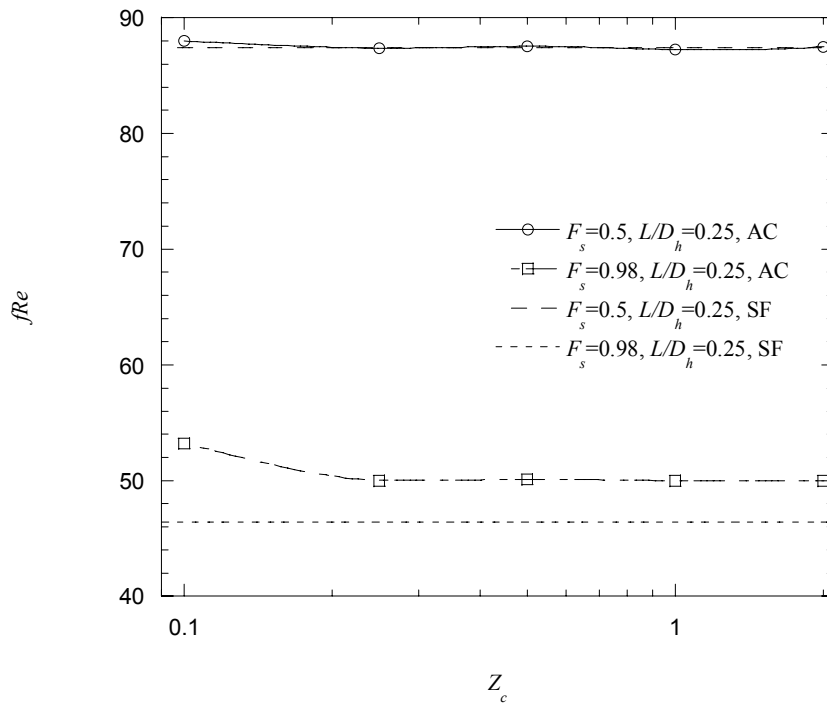


Figure 3.30: Dependence of fRe on the depth of the vapor cavity for the $L/D_h=0.25$ channel at $Re=1000$ and at slip fractions of $F_s=0.98$ and 0.5.

Further, the influence is dependent on the depth of the vapor cavity with cavities of relative depth smaller than $Z_c = 0.25$ (i.e., $h = 6 \mu\text{m}$ with $D_h = 10 \mu\text{m}$ and $l_s = 25 \mu\text{m}$) exhibiting a marked increase in the magnitude of fRe . The results further show that as the relative depth of the cavity increases above $Z_c \sim 0.25$ the predicted values of fRe become independent of the cavity depth. For scenarios with cavities of $Z_c > 1$, the magnitudes of fRe asymptote to 50 and 87.5 for the $F_s = 0.98$ and 0.5 cases, respectively. These magnitudes are, respectively, 8% and 0.1% greater than the predictions where the interface boundary condition was specified as zero shear.

As noted previously, due to the non-linear convective acceleration terms in the momentum equations (Eqs.3.3-3.4) the fRe behavior for the transverse rib orientation is expected to exhibit dependence on Re . This dependence is illustrated in Fig. 3.31 where the fRe product for the extreme slip fractions of 0.98 and 0.5 are plotted as a function of Re for the $L/D_h = 0.25$ channel. Note that both vapor-liquid interface boundary condition scenarios are shown for comparative purpose. For the predictions where the liquid and vapor spaces were coupled, the relative depth of the cavity was $Z_c = 2$. As discussed above and illustrated in Fig. 3.30 for $Z_c > 1$ the relative cavity depth is sufficient such that the fRe product is independent of the relative cavity depth. As Re approaches zero the fRe product for the two different imposed boundary conditions at the vapor-liquid interface asymptote to constant values of 82 and 86 for the $F_s = 0.5$ scenarios, and 34.5 and 45 for the $F_s = 0.98$ scenarios. Of course this behavior is expected since as Re approaches zero the flow is creeping and the non-linear terms of Eqs. (3.2) and (3.3) become negligibly small. At all Re , the fRe product is greater when the vapor cavity is coupled with the

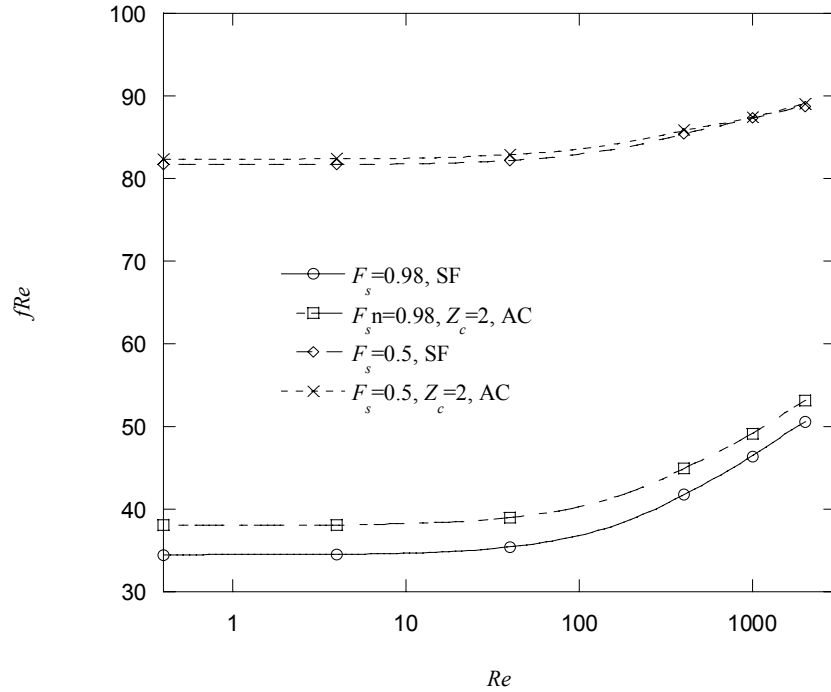


Figure 3.31: Variation of fRe with Reynolds number for the $L/D_n = 0.25$ channel, slip fractions of 0.02 and 0.5, and for both the (SF) interface and coupled vapor cavity interface conditions.

liquid phase in the model. Furthermore, the variation between the fRe product for the two interface conditions shows little dependence on the Reynolds number. For the $F_s = 0.98$ scenario, the relative difference in fRe between the no-shear and modeled interface scenarios varies from approximately 10 at $Re = 0$ to nominally 6 at $Re \sim 2000$. Above a Reynolds number of about 10 the fRe product begins to increase in magnitude with increasing Re . This increase results from the added pressure required to accelerate the flow over successive rib elements and it is thus more pronounced as the average velocity magnitude increases.

In summary the following conclusions can be made about drag reduction for channels with ultrahydrophobic surfaces.

- Increasing slip fraction decreases fRe

- Increasing dimensionless module length decreases fRe
- Decreasing Reynolds number decreases fRe
- Small dimensionless air cavities increase fRe
- A model that includes the vapor cavity has larger fRe than a model that assumes a shear free boundary condition at the liquid-vapor interface

4 CONSTANT WALL TEMPERATURE THERMAL TRANSPORT RESULTS

4.1 THERMAL MODEL DEVELOPMENT

In addition to the hydrodynamic study of the previous chapter a parametric study was also conducted on the same periodically fully-developed model of an ultrahydrophobic channel to obtain thermal transport results. In the hydrodynamic results two different models were used, (SF) and (AC) (with air cavity), this was possible because the ratio of viscosities for the fluid and gas of interest is small, $\mu_{air}/\mu_{water} = 0.02$. The thermal transport results, however, could not be simplified because the boundary condition at the liquid-gas interface was unknown. This requires that in each of the cases where the thermal transport results are displayed, the air cavity be included in the model. The surface of the silicon substrate was modeled to be at a constant temperature. Each repeated module was modeled to be thermally periodically fully-developed.

4.1.1 Thermally Periodically Fully-developed

To further explain the concept of a thermally fully-developed flow a classical fully-developed laminar parallel plate flow will be reviewed. In this scenario where the wall or surface temperature, T_s , is constant, and the fluid moves through the channel, in the x -direction the bulk mean temperature, T_m (see 4.1) will increase, eventually asymptoting to the wall temperature.

Figure 4.1 illustrates how the temperatures, T_m and T_s , change with axial position for the classical constant wall temperature fully-developed scenario.

$$T_m = \frac{1}{\rho \bar{u} A_c} \int_{A_c} \rho u T dA_c \quad (4.1)$$

A_c is the cross sectional area through which the fluid passes, u and T are the velocity and temperature of the fluid respectively at different locations on that area, and \bar{u} is the average velocity. T_m is the fluid mixed mean temperature characterizes the average thermal energy state of the fluid at a specific streamwise location [18].

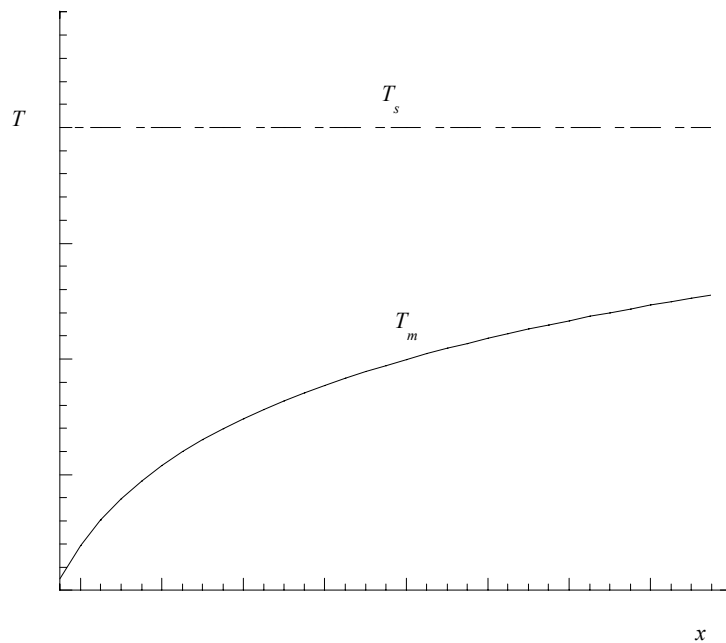


Figure 4.1: Qualitative variation of the bulk mean temperature, T_m , changes for a fully-developed laminar parallel plate flow with walls at a constant temperature, T_s .

Initially it may not appear that a temperature distribution such as this could yield a fully-developed behavior since the temperature changes at a different rate in the axial direction of the channel. A thermally fully-developed condition, however, is one where the dimensionless temperature does not change in the axial direction (see 4.2 below).

$$\frac{\partial}{\partial x}(\theta) = 0 \quad (4.2)$$

where θ is defined as the dimensionless temperature and is given in 4.3.

$$\theta = \frac{T_s - T}{T_s - T_m} \quad (4.3)$$

To more clearly illustrate a fully-developed temperature profile, Fig. 4.2 shows actual temperature profiles in a channel at two different axial or x -locations for a classical fully-developed parallel plate flow with the walls at a constant temperature. In this figure y^* again indicates the dimensionless position in the channel normal to the wall. In this scenario the fluid in the channel is cooler than the wall temperature and increases in bulk temperature as it moves in the axial direction.

The wall temperature is at 300 K, and it can be seen that the two profiles at different x -locations are not identical. The profile for T_2 is located downstream of the profile for T_1 , which is why the temperature is larger across the channel cross section.

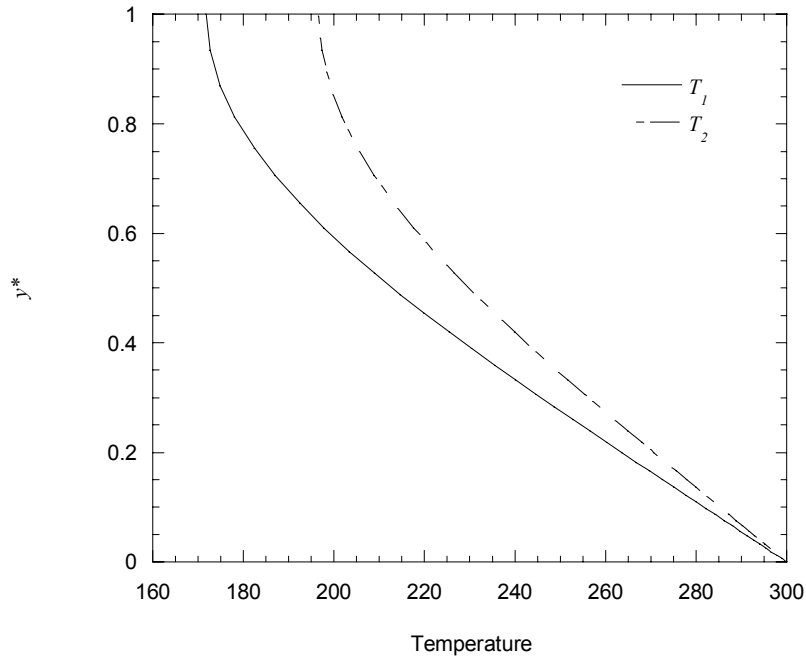


Figure 4.2: Temperature profiles at two different x -locations in a fully-developed laminar parallel plate flow with walls at a constant temperature, $T_s=300\text{K}$.

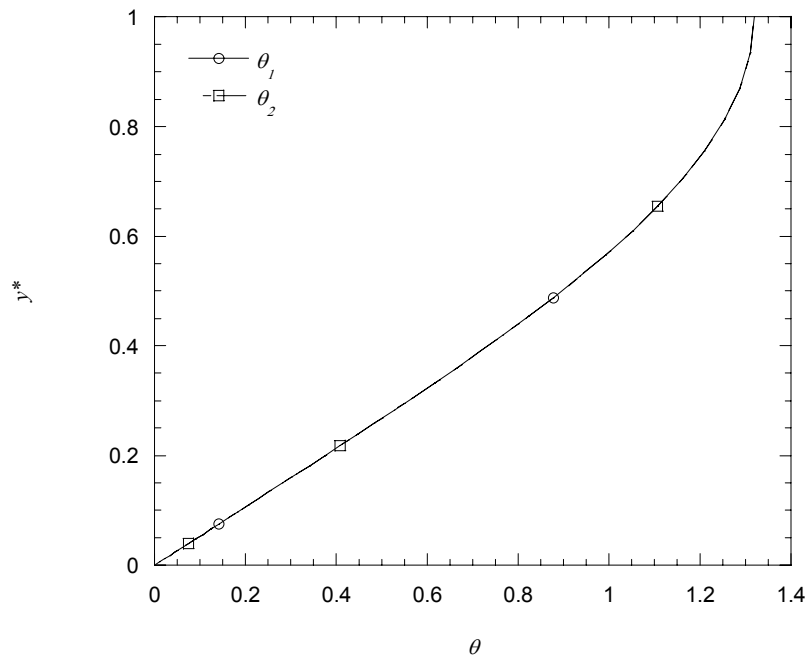


Figure 4.3: Dimensionless temperature, θ , profiles at two different x -locations in a fully-developed laminar parallel plate flow with walls at a constant temperature, $T_s=300\text{K}$.

Although, the temperature distributions are not the same, the dimensionless temperature, θ , for the two profiles are identical (See Fig. 4.3). This is what is meant by thermally fully-developed, the profile of θ remains constant at different axial locations along the channel.

Several differences from classical fully-developed duct flow exist with regard to the thermal transport for flow through microengineered channels. Just as was shown in Fig. 3.1, Fig. 4.4 shows the near-wall region of a channel that exhibits micro-rib structures separated by vapor-filled cavities. Liquid is flowing over the top of the wall from left to right in the figure and perpendicular to the ribs at a core velocity, U_∞ and upstream temperature T_∞ . Not only will a velocity boundary layer begin to grow at $x = 0$, but a thermal boundary layer (δ_t) will also begin to grow at this locale. Also, the fluid temperature at the wall will be the same as the wall temperature, given that continuum

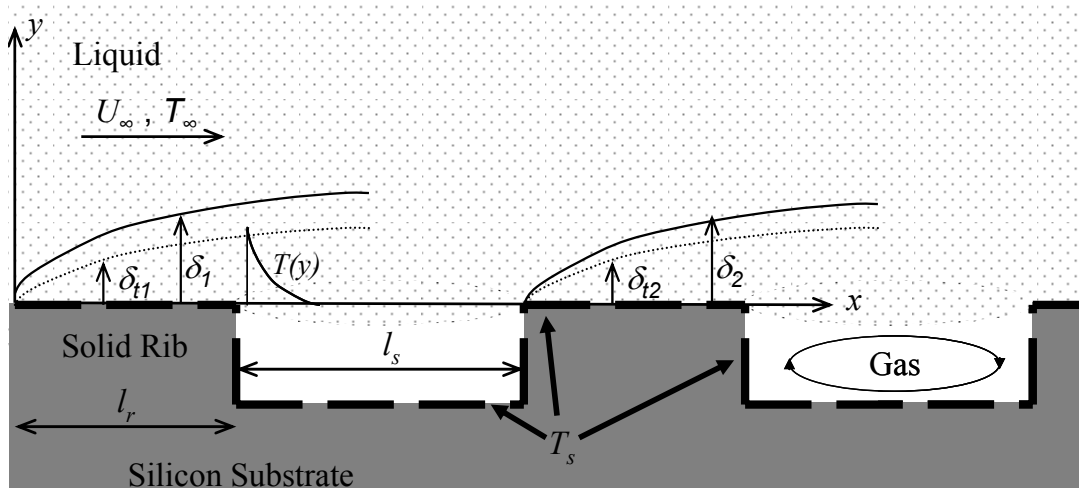


Figure 4.4: Schematic of the entrance wall and cavity regions for liquid flow over an ultra-hydrophobic surface exhibiting micro-rib structures and flow perpendicular to the ribs. Both hydrodynamic and thermal boundary layers are shown as well as how the constant wall temperature is imposed.

behavior is prevalent. For $l_r < x < l_r + l_s$ (the cavity region), the liquid will no longer be in contact with a solid surface and the liquid temperature at the vapor-liquid interface need not be the same as the wall temperature.

At the vapor-liquid interfaces several phenomena not common in traditional boundary layer flows are evident. First, the thermal boundary layer will continue to develop, but it will be at a much different rate and will be coupled to the vapor cavity thermal dynamics. The liquid and vapor temperatures will be equal, as will the heat flux in both phases at the interface be the same. At the second rib ($x > l_r + l_s$) a second thermal boundary layer begins to grow inside of the first and the wall heat flux will again decrease along the solid rib in the streamwise direction, although the initial value will not be as high as for the preceding rib. This behavior will repeat in the streamwise direction, and provided the meniscus shape remains the same, far downstream from the channel inlet a periodically thermally fully-developed state may be established. At this point the dimensionless temperature, θ , will exhibit periodic variations in the x -direction across repeating modules (of length $L = l_r + l_s$) consisting of a single rib and cavity. It is this thermally periodically fully-developed state that will be modeled in this study.

4.1.2 Metric for Comparison – Average Nusselt Number

To compare the ultrahydrophobic channels with those of a classical flow it is useful to compute the average Nusselt number, Nu shown in 4.4.

$$Nu = \frac{hD_h}{k} \quad (4.4)$$

Where h is the average heat transfer coefficient at the wall, D_h is the hydraulic diameter, and k is the thermal conductivity of the fluid. Just as the fRe value was constant for a classical flow, the value of Nu is also constant in the laminar fully-developed region for classical no-slip two-dimensional channel flow. Values for steady laminar flow through rectangular channels of varying aspect ratio have been tabulated by several investigators [17]. Following the classical approach [18-19], Nu can be derived for a constant wall temperature fully-developed laminar flow. From an energy balance on a channel the classical solution for the variation of mean temperature for constant wall temperature is logarithmic (see 4.5-4.6).

$$q = \dot{m}c_p(T_{mo} - T_{mi}) \quad (4.5)$$

$$q = \frac{hLB(T_{mo} - T_{mi})}{\ln\left(\frac{T_s - T_{mi}}{T_s - T_{mo}}\right)} \quad (4.6)$$

Where \dot{m} is the mass flow rate through the channel, c_p is the specific heat of the fluid, T_{mi} and T_{mo} are the bulk mean temperatures at the inlet and outlet of L respectively, T_s is the surface or wall temperature, L is the rib-cavity module length, and B is the width of the cross-sectional area (and in the case of infinite parallel plates $B \rightarrow \infty$). These equations can be combined and from 4.4 the average Nusselt number, Nu , can be derived (see 4.7).

$$Nu = \frac{\rho \bar{u} D_h^2 c_p}{4Lk} \ln\left(\frac{T_s - T_{mi}}{T_s - T_{mo}}\right) \quad (4.7)$$

For a classical two-dimensional parallel plate laminar flow with a constant wall temperature the value of the average Nusselt number is a constant (4.8), and will remain constant regardless of the Reynolds number (assuming it is laminar) or the relative module length, L/D_h .

$$Nu = 7.54 \quad (4.8)$$

Even though with the existence of ultrahydrophobic surfaces the bulk mean temperature does not vary with a smooth logarithmic function, the average Nu over the module length will be calculated using 4.7, and it will allow a direct comparison to the classical case. The Nu reported for channels with ultrahydrophobic surfaces is not technically the average Nusselt number of the channel, (i.e., it is not calculated by taking an average value of the heat transfer coefficient along the wall). Instead the apparent average Nu is calculated using the mean bulk outlet temperature of the fluid. Direct comparison with the classical condition is possible. When Nu is lower than 7.54, then this scenario exhibits poorer heat transfer than would occur in the classical constant temperature wall channel. The difficulty in calculating the average heat transfer coefficient stems from the fact that the wall has cavities and ribs with different phases present.

4.1.3 Solution Methodology

Following a similar approach used for the hydrodynamic calculations, the thermal transport results were obtained. A classical control volume approach was employed to characterize the periodically fully-developed thermal transport through an infinitely wide

channel for steady, laminar, conditions with constant fluid properties [19]. The energy equation given below for an incompressible Newtonian fluid was solved numerically.

$$\rho c_p \left(u \frac{dT}{dx} + v \frac{dT}{dy} \right) = k \left(\frac{d^2T}{dx^2} + \frac{d^2T}{dy^2} \right) + \mu \Phi \quad (4.9)$$

Where T is the temperature, u is the streamwise velocity, v is the wall-normal velocity, Φ is the viscous dissipation term, k is the thermal conductivity, c_p is the specific heat and ρ is the fluid density. The viscous dissipation term becomes more significant for scenarios where the viscosity of the fluid is large (like the viscosity of oils) and the temperature gradients are small. In this study the viscous dissipation was neglected because it was assumed that the temperature differences were significantly greater than the viscous dissipation term for a low viscosity fluid like water. To determine the significance of radiation a thermal transport estimate was calculated using a two surface black enclosure. The radiative heat transfer within the cavity was estimated to be the same magnitude as the thermal transport from convection at the liquid-vapor interface; however the total thermal transport was estimated to be two orders of magnitude larger. For this reason radiation was neglected in the model. Equation 4.9 was solved for the domain illustrated schematically in Fig. 4.5. As for the hydrodynamic results, the figure indicates a module length consisting of one rib and cavity section of the two-dimensional channel. The shape of the meniscus at the cavity interface was assumed to be perfectly flat, representing the limiting case of perfectly hydrophobic walls. The vapor space is of length l_s and the micro-rib width where the no-slip condition exists is of length l_r .

In addition to the boundary conditions specified for the hydrodynamic cases the thermal boundary conditions were imposed. Symmetric boundary conditions were specified at the channel centerline, $y = H/2$; constant wall temperature at on the surface of the hydrophobic channel as illustrated in Fig. 4.5. The conditions at the upstream and downstream edges parallel to the y -axis were specified to be thermally periodic, meaning θ , $\partial\theta/\partial x$, and $\partial\theta/\partial y$, were set to be equal at corresponding locations along these two faces. At the liquid-vapor interface, $y = 0$ and $l_r \leq x \leq l_r + l_s$ the solutions were coupled by matching local temperatures and heat fluxes at the interface. The liquid properties were specified to remain constant and equal those of water at standard temperature and pressure. Likewise the vapor fluid properties were specified to be constant and be the values of air at standard conditions.

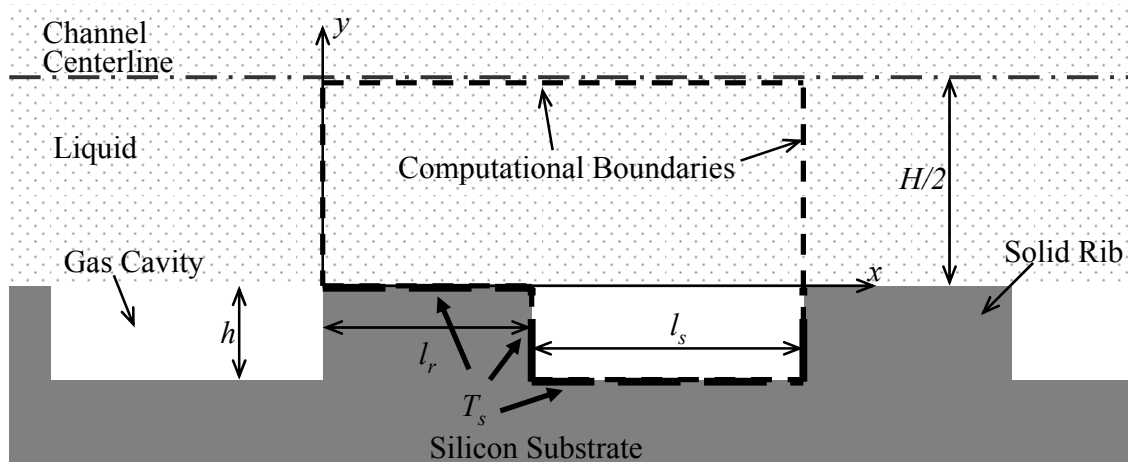


Figure 4.5: Schematic of the computational domain encompassing a rib/cavity module. Flow direction is from left to right. The domain extends into the gas cavity and the temperature of all the walls is indicated as T_s .

The thermal transport solution was obtained after the hydrodynamic solution was found. Occasionally, more grid refinement was necessary for the thermal transport solution because the grid-independent hydrodynamic solution was not grid-independent for the thermal solution. This was expected because the gradients were different between the thermal and hydrodynamic cases. For water, $Pr = 7$, which indicates that the thermal boundary layer, δ_t , will be smaller than the hydrodynamic boundary layer, δ , and to obtain an accurate solution more refinement is necessary. In practice after the grid was refined the hydrodynamic solution was solved followed by the thermal transport solution. The process of grid refinement, solving the hydrodynamic problem, and then solving the thermal transport problem had to be repeated several times in some scenarios.

4.2 THERMAL CONTOUR PLOTS

It is valuable to examine several different contour plots of temperature to show how it varies spatially. Here the temperature has been normalized with the wall temperature, T_s , and the mean outlet temperature, T_{mo} (see 4.10).

$$\Omega = \frac{T_s - T}{T_s - T_{mo}} \quad (4.10)$$

The normalized temperature, Ω , is different from θ in that for a classical scenario the temperature will change at different streamwise locations. This is advantageous in showing how the temperature changes in the domain and in showing the growth of the thermal boundary layer δ_t . It is also illustrative in obtaining a general idea of how the

temperature field in the computational domain is changing. In the following contour plots the temperature of the wall is higher than the temperature of the fluid.

Figure 4.6 shows a Ω contour plot for a slip fraction of 0.5, a relative module length of 0.25, a relative cavity depth of 1, and a Reynolds number of 1000. In this example the walls are at a higher temperature than the fluid. From 4.10 when $\Omega=0$ the temperature of the fluid is at the temperature of the wall and is shown in red. The maximum value of Ω occurs at the centerline of the channel because this is the region where the temperature difference between the fluid and the wall is the highest. In this scenario Ω does not change significantly in the streamwise direction for regions far from the rib. The only apparent streamwise variation in Ω occurs near the rib wall and near the

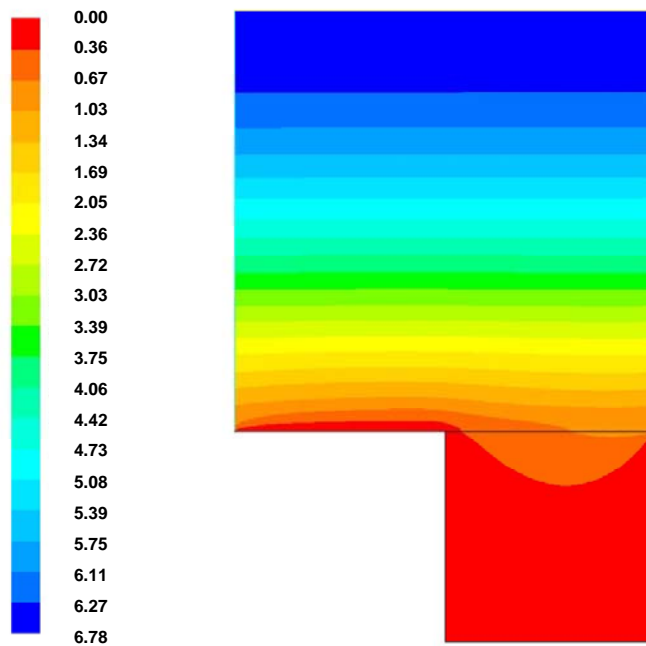


Figure 4.6: Contour plot of Ω for $F_s=0.5$, $Z_c=1$, $L/D_h=0.25$, and $Re=1000$.

gas-liquid interface. In general, Ω decreases as the fluid moves along the top of the rib and increases at the gas-liquid interface. This means that the fluid is increasing in temperature in the near wall region above the rib and then it is convected into a cooler region above the gas-liquid interface. At the outlet the bulk mean temperature is larger than it was at the inlet.

For a smaller Re the contours of Ω change significantly. This is shown in Fig. 4.7 where $F_s=0.5$, $Z_c=1$, $L/D_h=0.25$, and $Re=0.4$. In this scenario throughout the entire channel, except for the region near the gas-liquid interface, Ω is increasing in the streamwise direction. It does not appear periodic because of the definition of Ω , the mean temperature is always increasing so Ω will always increase. At the gas-liquid interface the cavity region has an insulating effect between the wall and the liquid, which is why there is a cooler region above the gas cavity into which hotter fluid is convected. The maximum value of Ω has changed, nearly doubling in value compared to the previous scenario where $Re=1000$. This happened because at low Re the temperature difference between the surface, T_s , and the bulk mean outlet temperature, T_{mo} , has decreased which effectively increases the maximum value of Ω . Even though the maximum value has changed this does not necessarily correlate to larger value of Nu . Recall that Nu is dependent on the change in temperature and on \bar{u} .

The influence of the slip fraction is shown in Fig. 4.8 where $F_s=0.98$, $Z_c=1$, $L/D_h=0.25$, and $Re=1000$. The most significant difference between this contour plot and Fig. 4.6 is the maximum Ω has changed from 6.78 to 1.26 indicating that there is less thermal transport occurring in this scenario. This effect is to be expected as the slip fraction has increased significantly and there is less wall contacting the liquid moving in the channel.

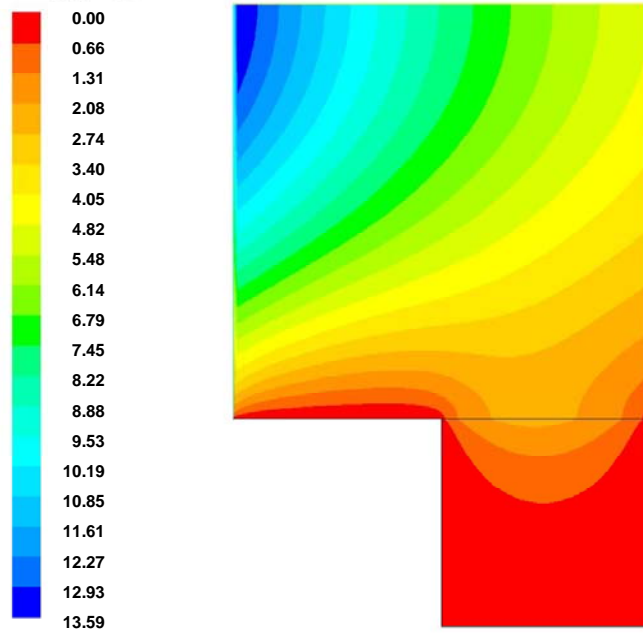


Figure 4.7: Contour plot of Ω for $F_s=0.5$, $Z_c=1$, $L/D_h=0.25$, and $Re=0.4$.

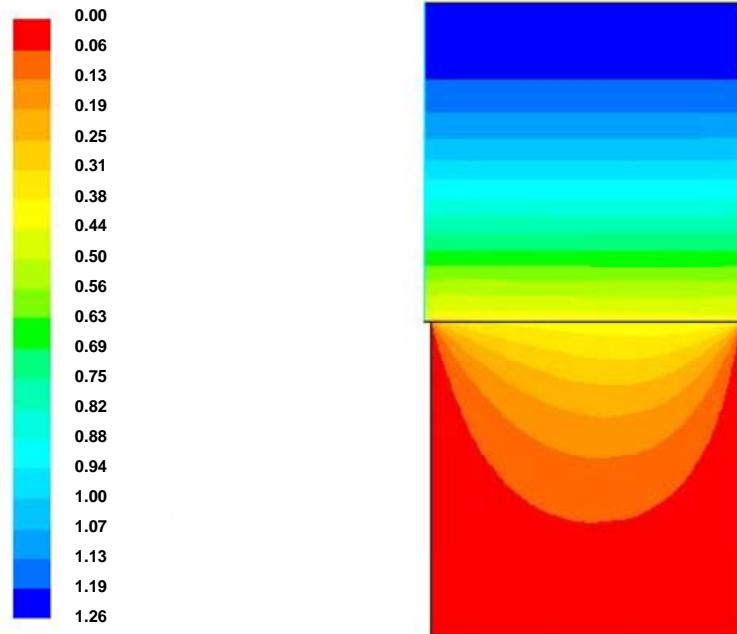


Figure 4.8: Contour plot of Ω for $F_s=0.98$, $Z_c=1$, $L/D_h=0.25$, and $Re=1000$.

The final contour plot is shown in Fig. 4.9. In this scenario $F_s=0.5$, $Z_c=2$, $L/D_h=0.05$, and $Re=0.4$. This figure shows the effect of changing the relative module length, L/D_h . When compared to Fig. 4.7 this shows that a change in the relative module length decreased the maximum value of Ω from 13.59 to 1.62 indicating less thermal transport exists for this scenario. It is important to notice that even though the maximum value of Ω decreased, the thermal boundary layer appears to grow in the same fashion as it did in Fig. 4.7.

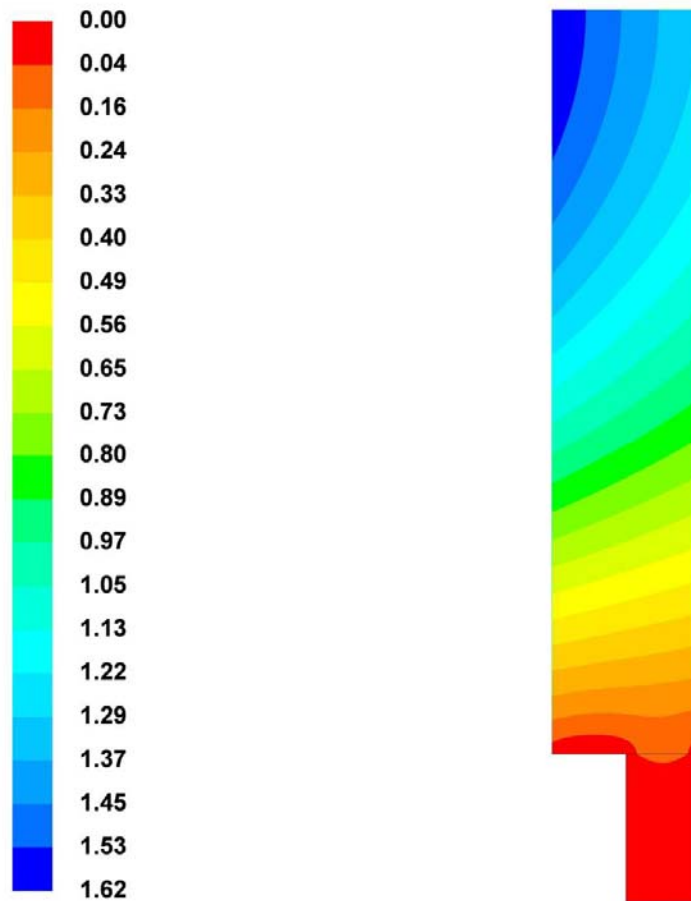


Figure 4.9: Contour plot of Ω for $F_s=0.5$, $Z_c=2$, $L/D_h=0.05$, and $Re=0.4$.

4.3 DETAILED THERMAL TRANSPORT PHYSICS

In section 4.1.1 it was seen that for a classical channel flow the profile of the dimensionless temperature remains constant at different locations within the channel. In this section the dimensionless temperature profiles of θ will be shown at various axial channel locations and will be compared to the classical case. Also, the effect of geometry and Reynolds number will be shown.

As was previously done, results will be presented at different x/L locations illustrated in Fig. 4.10. The value of θ will be calculated using the local fluid temperature, T , at different y -locations along the specific x/L location; T_s , the specified wall temperature; and T_m , the value of the bulk fluid temperature at that particular x/L location. T_m changes with x/L location, thus a new T_m must be calculated at each streamwise position to determine θ .

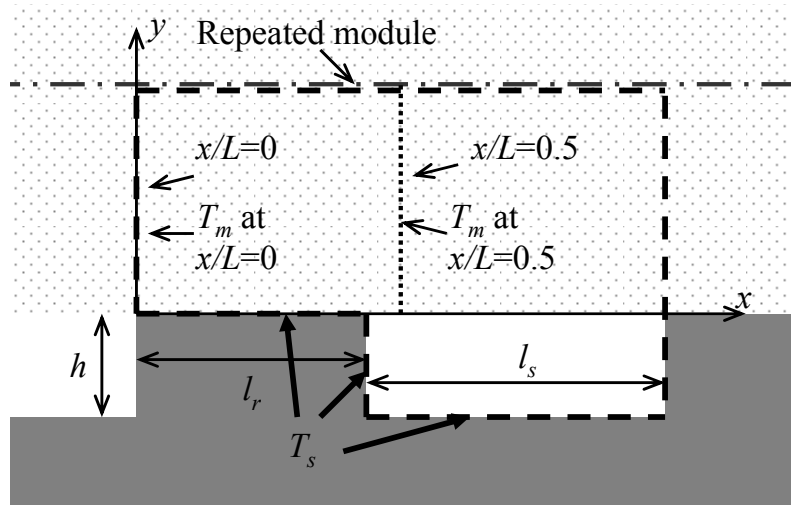


Figure 4.10: Schematic showing percentage of repeated module and mixed mean temperature T_m used in reporting dimensionless temperature data.

In practice the constant wall temperature boundary condition shown in Fig. 4.10 may be difficult to obtain, but it serves as a comparison to a classically studied situation. A more realistic scenario would be to model the bottom side of the silicon as having a constant temperature or constant heat flux. This would be a recommendation for further study but is beyond the scope of this thesis.

In Fig. 4.11, one example of how the dimensionless temperature, θ , changes for a fully-developed flow through a channel with ultrahydrophobic surfaces is shown. The results shown correspond to the scenario: $F_s=0.5$, $Re=1000$, $L/D_h=0.25$, and $Z_c=2$. The data show that for this case the θ profile exhibits only minor deviation from the classical case. This deviation occurs in the near wall region. The value of θ for the

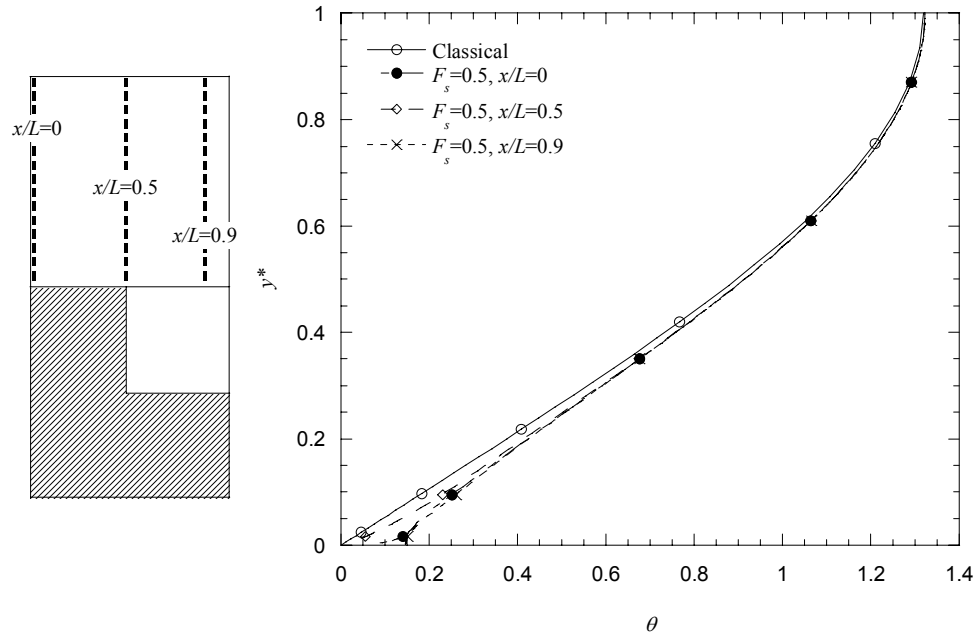


Figure 4.11: Schematic showing dimensionless temperature, θ , for a case where $F_s=0.5$, $Re=1000$, $L/D_h=.25$, and $Z_c=2$ compared to a classical case.

ultrahydrophobic case is always greater than θ for the classical case. From 4.3 this implies the result shown in 4.11 below. The implication is that the value of the local fluid temperature, T , throughout the domain is not as high in the ultrahydrophobic case as it is in the classical case. This is rigorously true only if T_m is the same for both scenarios.

$$\left(\frac{T_s - T}{T_s - T_m} \right)_{\text{Ultrahydrophobic}} > \left(\frac{T_s - T}{T_s - T_m} \right)_{\text{Classical}} \quad (4.11)$$

Greater detail of what is occurring in the near-wall region is shown in Fig. 4.12 (20% of channel shown). For the regions along the surface of the rib ($0 < x/L < 0.5$ at $y^* = 0$) the value of θ vanishes as in the classical case, since the wall temperature is specified at that point. Further from the rib wall θ increases with a steeper gradient than for the classical case. Along the interface between the liquid and the vapor ($0.5 < x/L < 1$) the value of θ need not vanish at $y^* = 0$. The vapor cavity acts as an insulator between the fluid and the wall temperature. The liquid-vapor interface has a larger value of θ because T is smaller. The profile of θ for $x/L = 0$ closely follows the profile of θ for x/L above the cavity regions because the fluid at $x/L = 0$ has just come from a previous cavity region. The profiles will be the same at $x/L = 0$ and $x/L = 1$ because of the imposed periodically fully-developed thermal boundary condition. It is important to highlight that there is a steeper dimensionless temperature gradient above the rib than in the classical scenario and there is a smaller gradient above the cavity than in the classical scenario.

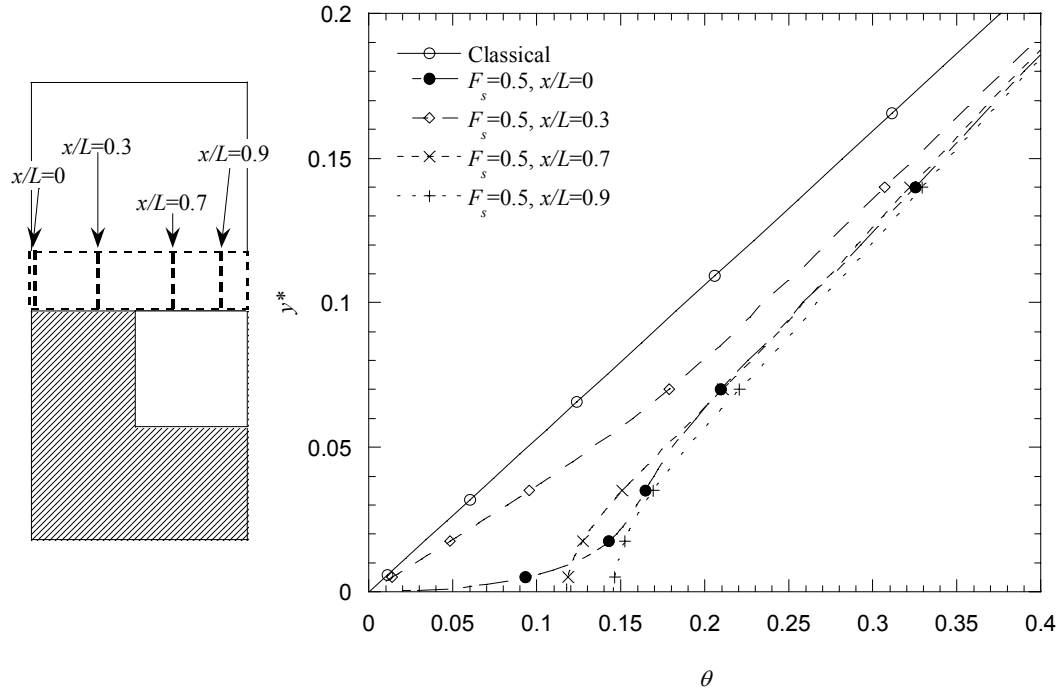


Figure 4.12: Schematic showing the near-wall region of dimensionless temperature, θ , for a case where $F_s=0.5$, $Re=1000$, $L/D_h=.25$, and $Z_c=2$; compared to a classical case.

This means that the thermal transport is high above the rib where the liquid is in direct contact with the wall and the velocity gradients are the highest. A smaller gradient above the cavity indicates that the thermal transport in this area is reduced.

4.3.1 Influence of F_s on θ

The slip fraction F_s plays an important role in the behavior of the local normalized temperature θ . As the slip fraction increases the profiles of θ deviate significantly from the classical case. Shown below in Fig. 4.13 are normalized temperature profiles for two slip fractions. Both cases are at $Re=1000$, $L/D_h=.25$, and $Z_c=2$. The only difference is that for one scenario $F_s=0.5$, and for the second $F_s=0.98$. Fig. 4.13 shows that near the wall (above rib) the fluid in the 98% slip fraction channel has a much larger value of θ

than in the 50% slip fraction channel. Also the local wall-normal gradient is much greater resulting in high thermal transport in this region. Near the channel centerline, however, the value of θ for the 98% slip fraction channel is smaller. In the 98% slip fraction channel there is very little contact with the solid rib because of its characteristic small surface area. Although there is little solid-liquid contact at these interfaces a much smaller thermal boundary layer results, and the wall-normal gradient of θ is much greater.

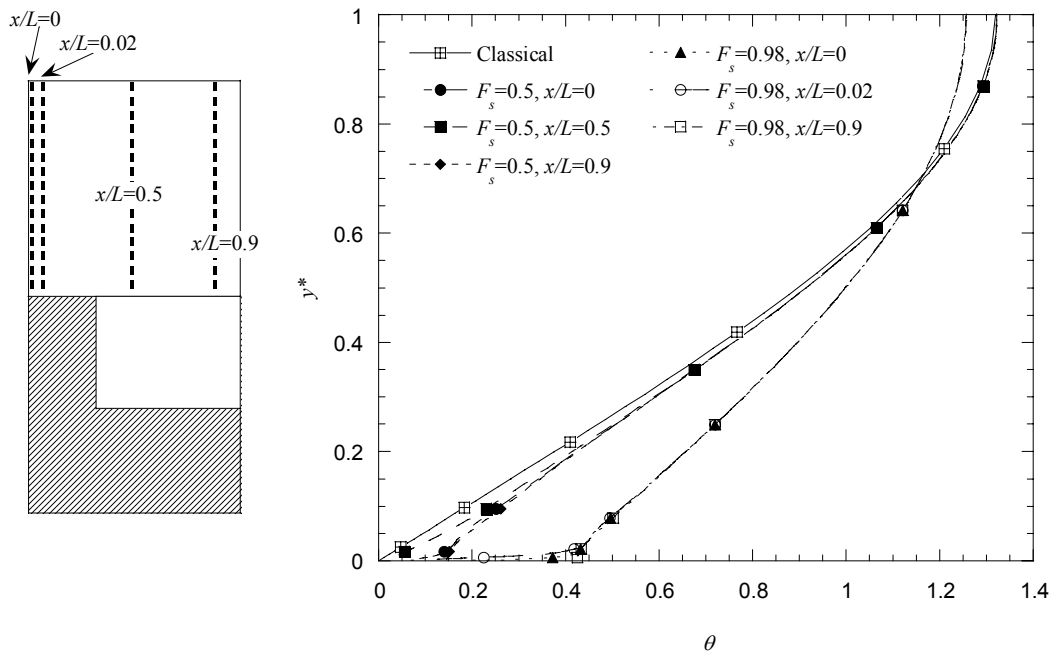


Figure 4.13: Schematic showing comparison θ profiles where $F_s=0.5$ and $F_s=0.98$ while $Re=1000$, $L/D_h=0.25$, and $Z_c=2$. Also shown is θ for a classical scenario.

More detail of the near-wall region is shown in Fig. 4.14. Here it can be seen that after the fluid is transported above the cavity region the thermal energy of the fluid diffuses and the distribution of θ becomes more uniform. Another cause of the uniform

profile is due to the lower temperature air in the cavity. The air is not at the same temperature as the wall because of the motion of the air in the cavity, and the temperature gradient at the liquid-vapor interface.

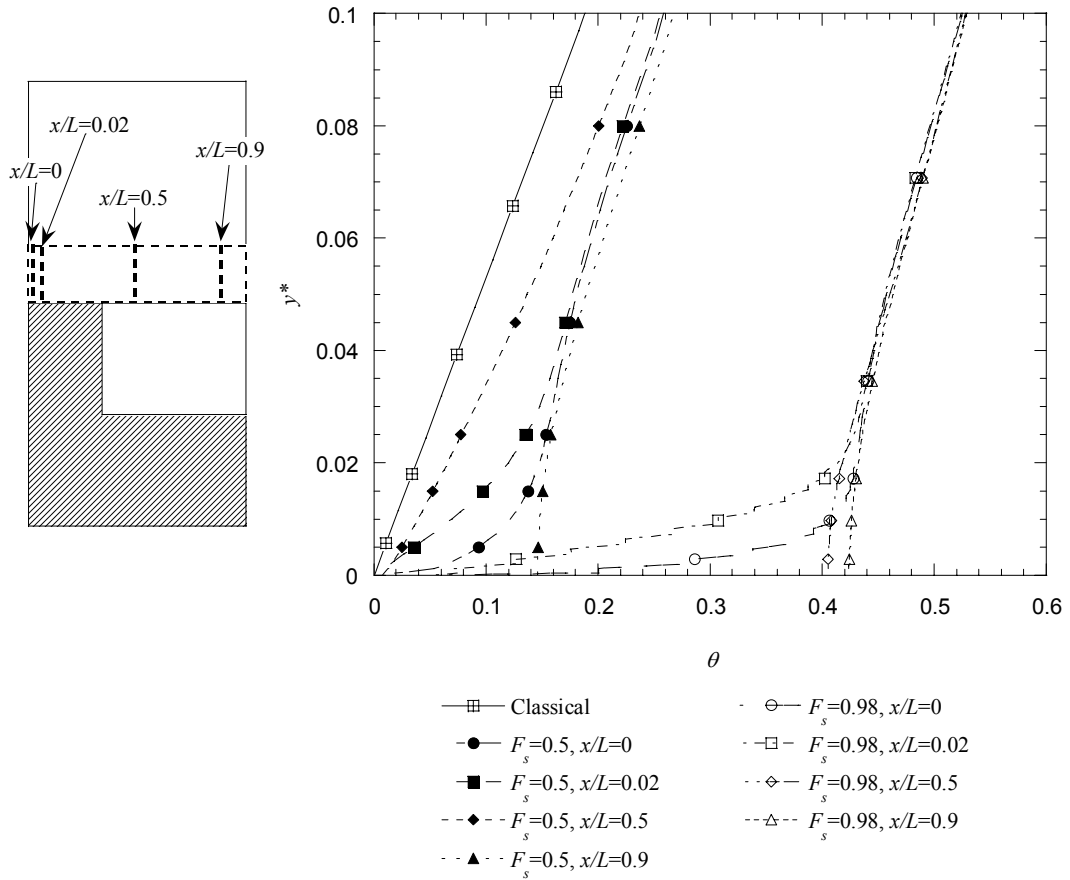


Figure 4.14: Schematic showing the near-wall region (20% of channel) of a comparison of θ profiles where $F_s=0.5$ and $F_s=0.98$ while $Re=1000$, $L/D_h=0.25$, and $Z_c=2$. Also shown is θ for the classical scenario.

4.3.2 Influence of Re on θ

The channel Reynolds number also exercises a large influence on the behavior of the local fluid temperature, θ , and the overall thermal transport. The reason for the

influence is because of the nonlinear nature of the momentum equations and the fact that the velocity profiles vary with Re . The local velocity greatly influences the thermal transport. In the classical scenario profile, θ does not change as the Reynolds number varies in the laminar flow regime unless the flow transitions to turbulent behavior, or if the $Pe \ll 1$ (low Pe flows were not considered here). The Peclet number, Pe , is the product of the Reynolds number, Re , and the Prandtl number, Pr , and indicates the significance of axial conduction. At high values of Pe axial conduction is insignificant, since at very high Re the convective terms in 4.9 dominate the thermal transport in the system. On the contrary, low values of Pe make the conduction terms in 4.9 more significant and axial conduction cannot be neglected in the analysis.

An example of the effect of Reynolds number variation on the local temperature field is shown in Fig. 4.15. Here results from two different Reynolds numbers, $Re = 1000$ and $Re = 4$ are compared. The geometric parameters are the same for the two cases; $F_s = 0.98$, $L/D_h = 0.25$, and $Z_c = 2$. For this channel geometry a lower Reynolds number tends to shift the temperature profile to be more nearly uniform in the wall-normal direction. Even though the Reynolds number is low ($Re = 4$), Pe is not low enough such that there will be significant axial conduction. It is low enough, however, such that the wall-normal conduction is much greater. At higher Reynolds numbers convection is more dominant and the diffusion of heat into the channel centerline is less significant compared to the convection. It should be pointed out that although there is a difference in the velocity profiles from the hydrodynamic results, the difference is small and is not sufficient to explain this behavior.

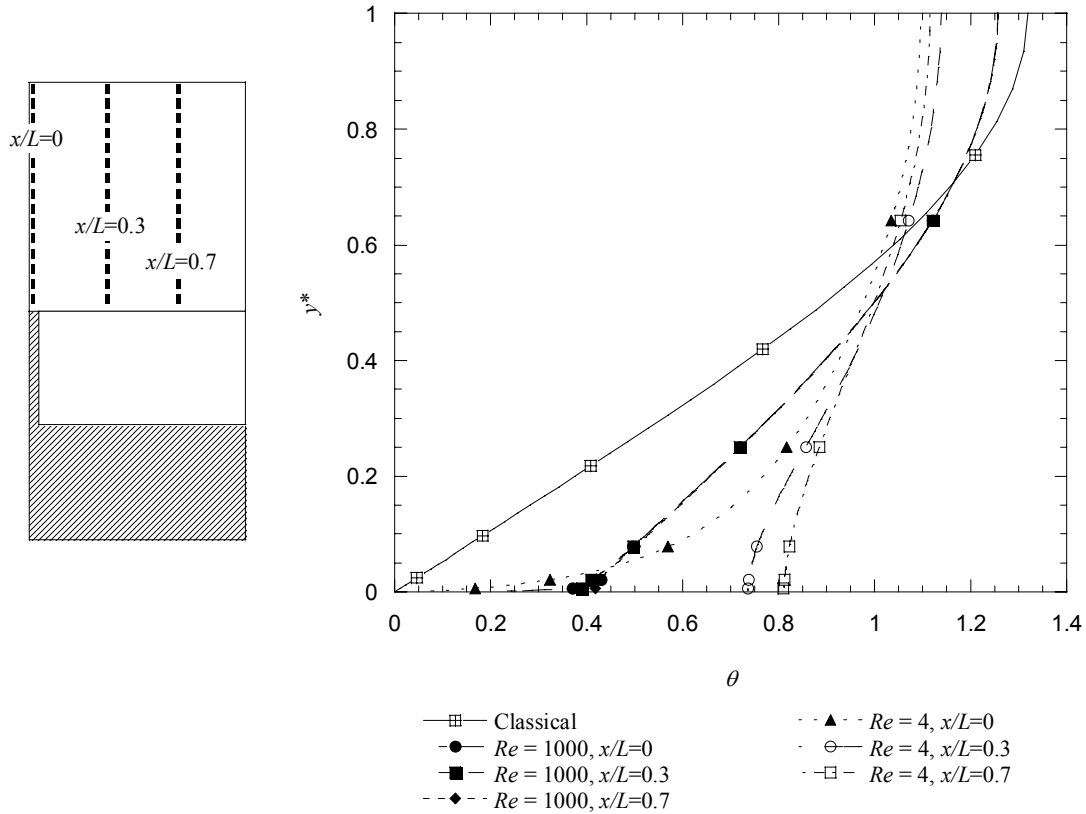


Figure 4.15: Schematic showing effect of Re on the θ profile. A classical case is shown with two ultrahydrophobic cases where $Re=1000$ and $Re=4$ for $F_s=0.98$, $L/D_h=0.25$, and $Z_c=2$.

A near-wall region view of the temperature profiles in Fig. 4.15 is shown in Fig. 4.16 (inner 10% shown). The geometry of each scenario is $F_s = 0.98$, $L/D_h = 0.25$, and $Z_c = 2$ while $Re = 1000$ for one scenario and $Re = 4$ for the other. In this figure more detail of the near-wall region is shown and the steep temperature gradient above the rib in the high Re scenario becomes more evident. Larger temperature gradients are indicative of more thermal transport. For both Re the gradient above the cavity region is small, but it is even smaller for the low Re scenario.

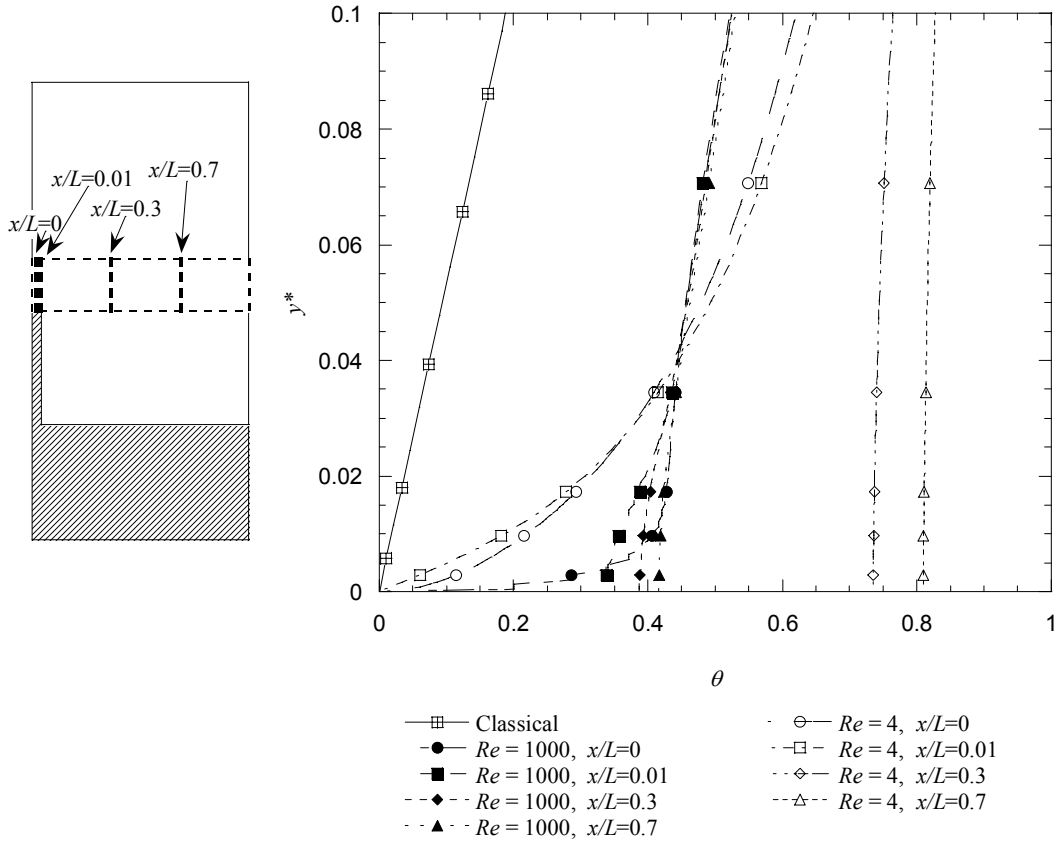


Figure 4.16: Near-wall region showing the effect of Re on the θ profile. A classical case is shown with two ultrahydrophobic cases where $Re=1000$ and $Re=4$ for $F_s=0.98$, $L/D_h=0.25$, and $Z_c=2$.

4.3.3 Influence of L/D_h on θ

An interesting pattern was observed in the velocity profiles when the relative module length was decreased, the velocity profiles in the channel became more like those of a classical channel. Here, as the value of L/D_h , the dimensionless module length, decreases the thermal transport follows the same pattern; the ultrahydrophobic surface tends to have less of an effect on the profiles of θ . This can be seen below in Fig. 4.17 where results for two different values of L/D_h are shown, $L/D_h=0.05$ and $L/D_h=2.5$ for $F_s=0.5$, $Re=1000$, and $Z_c=2$. The scenario with $L/D_h=2.5$ shows a large deviation in θ at

two x/L locations shown. Conversely, the case where $L/D_h = 0.05$ shows a θ profile very similar to the classical case. The reason for this behavior is because as the relative module length increases there is more surface area to volume ratio. At a greater surface area to volume ratio the insulating effect of the gas cavity is increased and small temperature gradients are seen above the cavity region, indicative of less thermal transport.

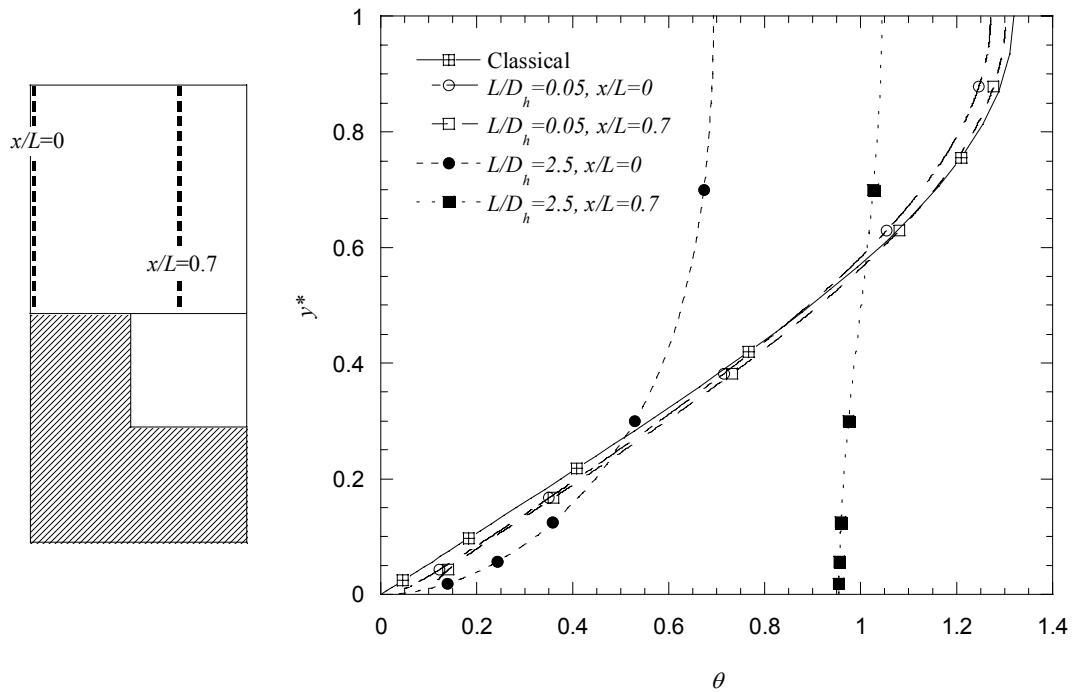


Figure 4.17: Schematic showing the effect of L/D_h on the θ profile. A classical case is shown with three ultrahydrophobic cases where $L/D_h = 0.05$ and $L/D_h = 2.5$ for $F_s=0.5$, $Re=1000$, and $Z_c=2$.

4.3.4 Influence of Z_c on θ

Surprisingly, the value of Z_c did not have a noticeable effect on the θ profiles. Recall that minor differences were noticed in the velocity profiles. Although the velocity differences were small, the cavity depth, Z_c , did not appear to affect θ significantly.

4.3.5 Heat Flux at the Interface and Rib Wall

This subsection focuses on showing how the heat flux at the rib wall and the liquid-vapor interface varies depending on the parameters F_s , L/D_h , Re , and Z_c . The heat flux has been normalized according to 4.12,

$$\zeta = \frac{q'' D_h^2}{k(T_s - T_{mo})} \quad (4.12)$$

where q'' is the heat flux, D_h is the hydraulic diameter, k is the thermal conductivity of the liquid, T_s is the wall temperature, and T_{mo} is the bulk mean temperature of the fluid as it leaves the channel. Fig. 4.18 shows the effect of Re on the dimensionless heat flux, ζ , for $F_s=0.5$, $L/D_h=0.25$, and $Z_c=2$. The heat flux at the beginning of the rib is extremely high because of the nearly infinite temperature gradient at that location (i.e., cool fluid in direct contact with a hot surface). The heat flux above the rib is larger for $Re=1000$ than it is for $Re=4$, whereas above the cavity region the opposite is true. The profiles also appear more symmetric, meaning that the heat flux in the first half of the rib is symmetric with the last half of the rib (the same is true for the cavity), for the lower Re scenario.

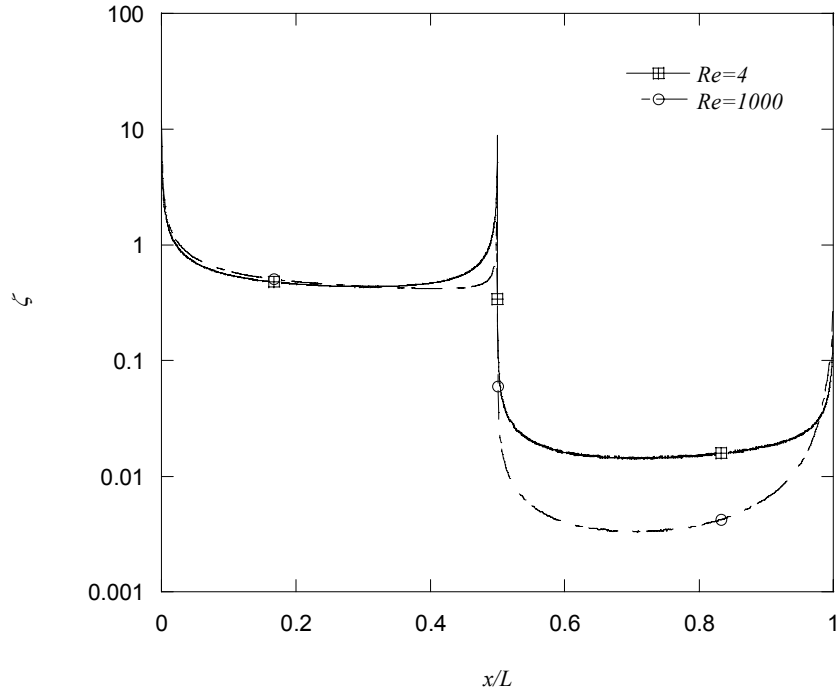


Figure 4.18: Normalized heat flux at the rib wall and interface for two ultrahydrophobic cases where $Re=1000$ and $Re=4$ for $F_s=0.5$, $L/D_h=0.25$, and $Z_c=2$.

Shown in Fig. 4.19 are predicted heat fluxes for $L/D_h=0.25$ and $L/D_h=0.05$ where $F_s=0.5$, $Re=4$ and $Z_c=2$. The results show a much larger heat flux above both the rib and the cavity region for the scenario where $L/D_h=0.05$ than for $L/D_h=0.25$. This difference occurs because the ratio of volume to surface area is higher for low values of L/D_h , meaning that there is more fluid in the domain in contact with the wall that is at a different temperature (either cold or hot). For $L/D_h=0.05$ the heat flux decreases above the rib, which is more characteristic of a classical constant temperature heat flux profile. Subsequently, as the fluid moves above the cavity the heat flux drops significantly for both cases. It is interesting to note that for a high value of L/D_h the heat flux profiles are more nearly symmetric in the streamwise direction in this scenario.

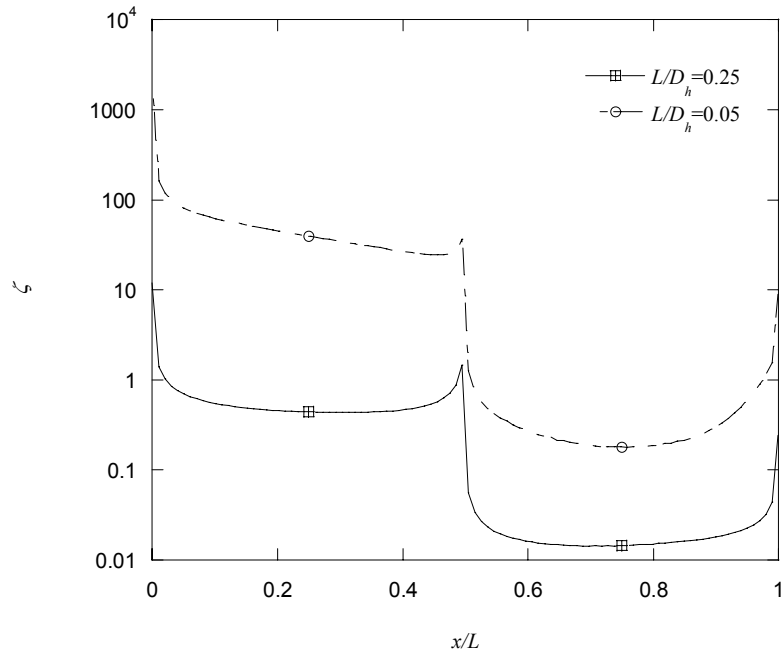


Figure 4.19: Normalized heat flux at the rib wall and interface for two ultrahydrophobic cases where $L/D_h = 0.25$ and $L/D_h = 0.05$ for $F_s = 0.5$, $Re = 4$, and $Z_c = 2$.

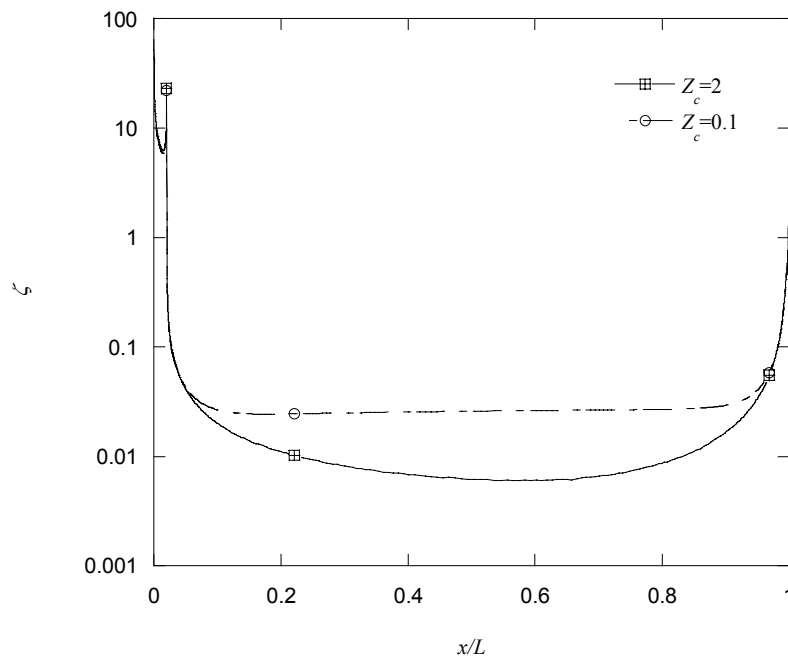


Figure 4.20: Normalized heat flux at the rib wall and interface for two ultrahydrophobic cases where $Z_c = 2$ and $Z_c = 0.1$ for $F_s = 0.98$, $Re = 1000$, and $L/D_h = 0.25$

Fig. 4.20 shows the effect of changing Z_c from 2 to 0.1. The only noticeable affect is in the heat flux above the cavity region. The heat flux is larger for a smaller value of Z_c because the relative air cavity depth is smaller and the hot wall is closer to the fluid, thereby increasing the heat flux. Even though the heat flux varies with the relative cavity depth it is so small that the θ profiles of section 4.3.4 showed no difference.

4.4 AVERAGE NUSSOLT NUMBER RESULTS

For the cases studied in this section, once a grid-independent solution was obtained the inlet and outlet bulk mean temperatures (T_{mi} and T_{mo}) could be reported. This information along with the other parameters such as channel geometry and Reynolds number could be used with 4.7 to calculate the average Nusselt number for each scenario. Trends in the average Nusselt number indicate that ultrahydrophobic surfaces decrease the overall thermal transport performance. As a general rule, when the frictional pressure drop was reduced so was the heat transfer, although not necessarily at a proportional rate.

Fig. 4.21 shows the effect of Reynolds number on Nu at a low value of L/D_h . The results show that as the Reynolds number increases the average Nusselt number increases monotonically. This behavior is more consistent with external boundary layer flows than it is for fully-developed internal flows. Also shown is the improvement that can be expected as the value of F_s decreases. The reason for the improvement in Reynolds number for a smaller slip fraction is due to the fact that the liquid is in contact with more surface area of the heated rib. This increases the heat transfer and results in a larger Nusselt number.

When the same study was performed at a different relative module length ($L/D_h = 2.5$), the variation in Nu with Reynolds number is greater. These results are shown in Fig. 4.18. Here as the Reynolds number increases the average Nusselt number increases as well. The reason Nu varies more with Re at a larger relative module length as shown in Fig. 4.22 compared with Fig. 4.21 is because a larger relative module length corresponds to a larger surface area to volume ratio. Larger Re create smaller thermal boundary layers and causing the heat flux to increase. It is the combination of both the Re effect and the L/D_h effect that make the variance on Nu greater in Fig. 4.22 than in Fig. 4.21.

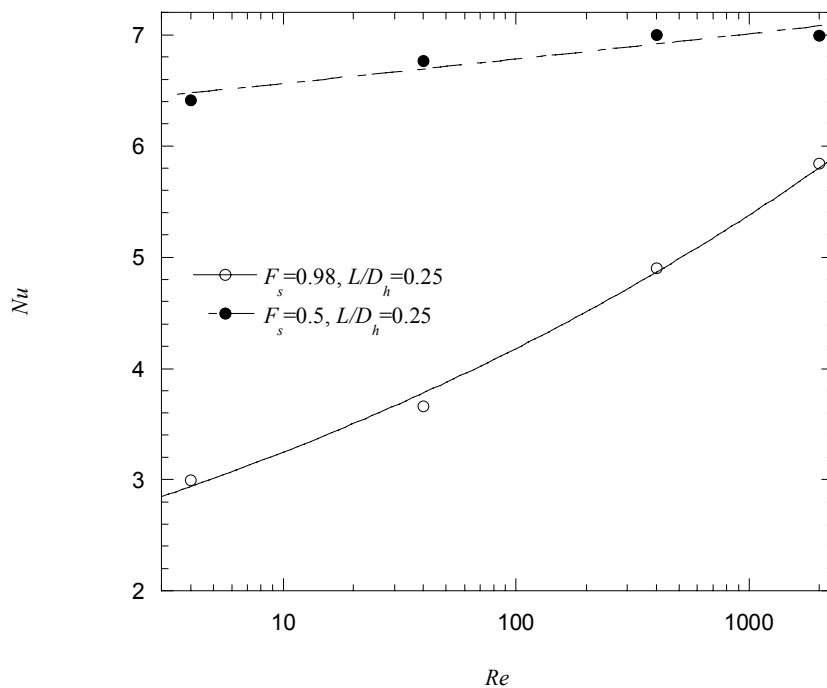


Figure 4.21: Schematic showing effect of Re on Nu for $F_s=0.98$ and $F_s=0.5$ where $L/D_h = 0.25$, and $Z_c=2$.

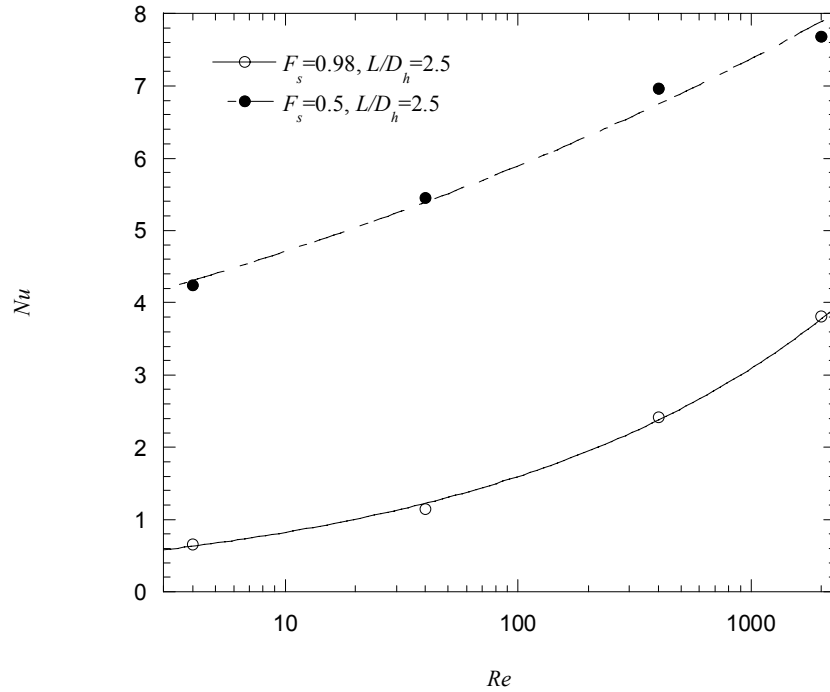


Figure 4.22: Schematic showing effect of Re on Nu for $F_s=0.98$ and $F_s=0.5$ where $L/D_h=2.5$, and $Z_c=2$.

The influence that F_s exerts on the average Nusselt number is shown in Fig. 4.23 for two different values of L/D_h , 0.05 and 2.5. For all scenarios in the figure $Re=1000$ and $Z_c=2$. The figure shows that for small relative module lengths, $L/D_h=0.05$ (large channel spacing), large slip fractions ($F_s > 0.9$) lead to a decrease in the thermal transport, although below a slip fraction of 0.9 the average Nusselt number does not change significantly. At a small value of L/D_h the change in average Nusselt number was much smaller regardless of the slip fraction.

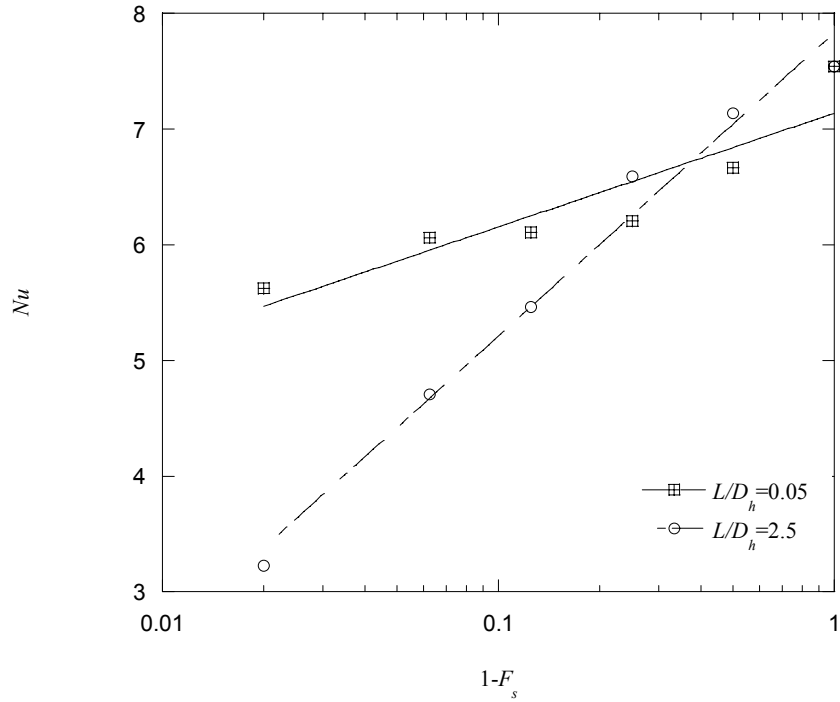


Figure 4.23: Schematic showing effect of F_s on Nu for $L/D_h = 0.05$ and $L/D_h = 2.5$ where $Re=1000$, and $Z_c=2$.

In summary the following conclusions can be made about thermal transport for a constant temperature channel with ultrahydrophobic surfaces.

- Increasing the slip fraction decreases Nu
- Increasing the dimensionless module length decreases Nu
- Decreasing the Reynolds number decreases Nu
- Relative cavity depth had no significant effect on Nu

4.5 COMBINED EFFECT OF AVERAGE NUSSELT NUMBER AND DARCY FRICTION FACTOR – REYNOLDS NUMBER PRODUCT

It has been shown that the average Nusselt number is decreased by using ultrahydrophobic surfaces and it has been shown that the required pressure drop along the channel can be decreased by using these surfaces. In applications where high heat transfer is important as well as having a low pressure drop in the channel, the effect of ultrahydrophobic surfaces are competing, i.e., they help lower the pressure drop, but at the same time they can degrade the heat transfer. Although the two are competing factors, the benefits of the reduction in pressure may outweigh the cost of the reduction in heat transfer.

One way to quantify this difference is to compare ratios of the Nu to fRe between the ultrahydrophobic case and a classical scenario, $(Nu/fRe)/(Nu/fRe)_{classical}$. When this ratio is greater than unity, it would indicate that the ultrahydrophobic surface has more benefit than the classical surface, or the loss in heat transfer compared to the gain in reduction in pressure is better than the classical case.

Fig. 4.24 shows the effect of Reynolds number on $(Nu/fRe)/(Nu/fRe)_{classical}$ at low and high values of L/D_h (2.5 and 0.25) for two different slip fractions ($F_s=0.98$ and 0.5) where $Z_c=2$. The results show that as the Reynolds number increases the ultrahydrophobic surface performs better than a classical scenario. Significant benefit is shown for a large slip fraction ($F_s=0.02$). This plot shows that for $F_s=0.5$ and $L/D_h=0.25$ performance is worse than a classical wall.

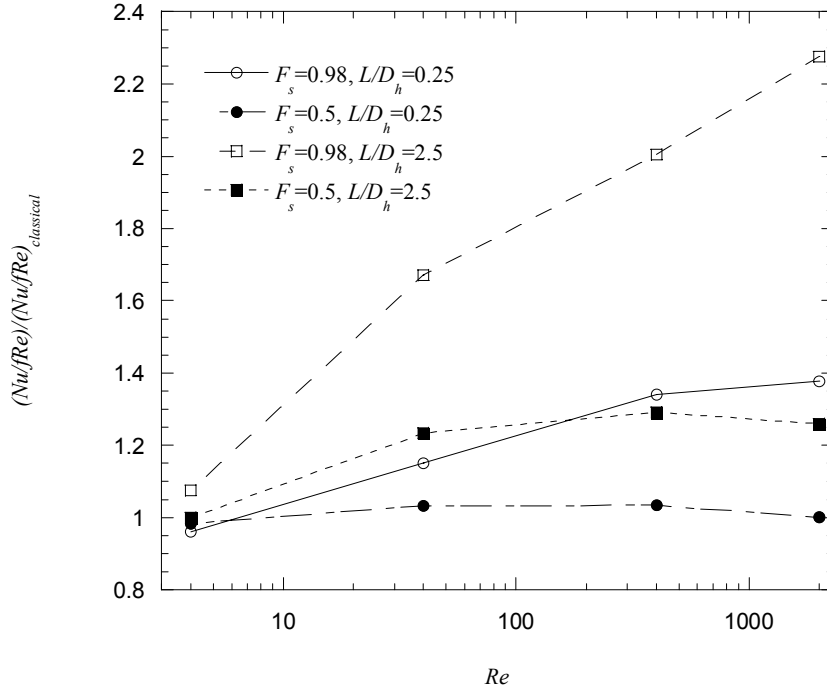


Figure 4.24: Schematic showing effect of Re on $(Nu/fRe)/(Nu/fRe)_{classical}$ for $F_s=0.98$ and $F_s=0.5$ where $L/D_h=2.5$ and 0.25 , and $Z_c=2$.

The effect of F_{ns} on $(Nu/fRe)/(Nu/fRe)_{classical}$ is shown in Fig. 4.25 for two different values of L/D_h , $L/D_h=0.05$ and $L/D_h=2.5$, and for all scenarios in the figure $Re=1000$ and $Z_c=2$. The figure shows that for $L/D_h=0.05$, as the slip fraction decreases the performance of the ultrahydrophobic surface relative to the classical scenario decreases, but in all cases studied for $L/D_h=0.05$ the performance is better. The reason performance was found to be higher is because of the large effect of the pressure drop that a large relative module length, L/D_h , had. The rate of improvement for fRe was greater than the rate of improvement for Nu . For $L/D_h=2.5$ the performance is worse than the classical case and the slip fraction was predicted to have little effect on the performance.

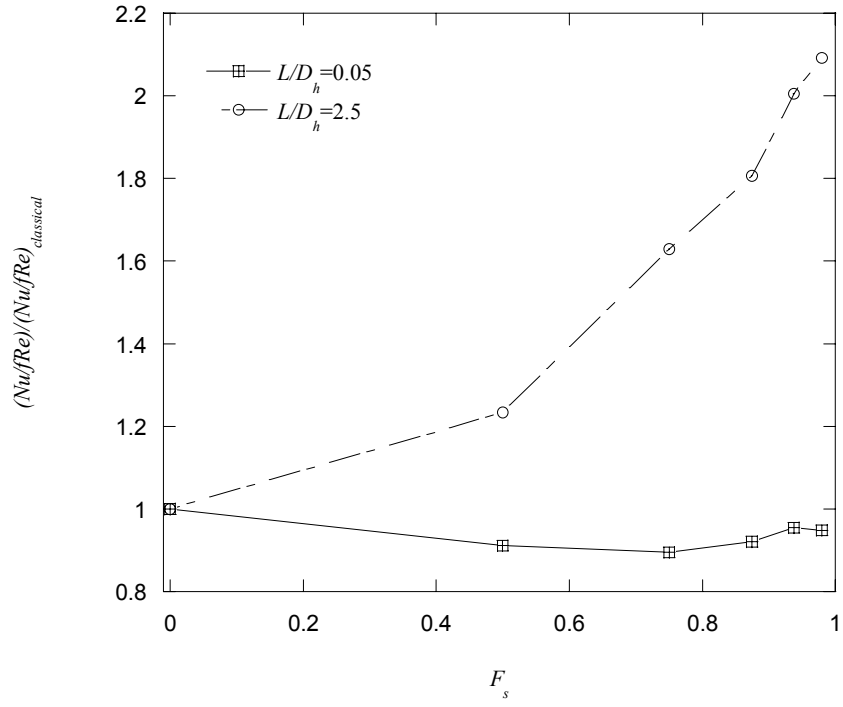


Figure 4.25: Schematic showing effect of F_s on $(Nu/fRe)/(Nu/fRe)_{classical}$ for $L/D_h = 0.05$ and $L/D_h = 2.5$ where $Re=1000$, and $Z_c=2$.

5 CONCLUSIONS AND RECOMMENDATIONS

5.1 CONCLUSIONS

Results of an analytical investigation of the laminar, periodically fully-developed flow in a parallel plate microchannel with ultrahydrophobic walls are reported in this thesis. The ultrahydrophobic surfaces were modeled with microrib and cavity structures oriented perpendicular (transverse) to the flow direction where the walls are treated with a hydrophobic coating. Two conditions were explored with regard to the cavity region: 1) The liquid flow at the liquid-vapor interface was treated ideally as shear-free (vanishing viscosity in the vapor region), and 2) the liquid flow in the microchannel core and the vapor flow within the cavity were coupled through the velocity and shear stress matching at the interface. Velocities, both streamwise and wall-normal, were predicted and compared between the two different cases. The average streamwise velocity was found to be slightly smaller when the vapor flow was modeled. The streamwise centerline velocity was smaller than the classical centerline velocity because there was more motion of the fluid near the wall. The wall shear stress was predicted at the rib wall and liquid-vapor interface from which the average pressure drop was determined. The wall shear stress above the rib was predicted to be larger than the wall shear stress for the classical scenario, while the shear stress at the liquid-vapor interface was predicted to be much smaller.

Predictions reveal that significant reductions in the frictional pressure drop can be achieved relative to the classical smooth channel flow. Reductions in the friction factor are greater (up to 90% reduction) as the cavity-to-rib length ratio is increased (increasing slip fraction) and as the relative module length is increased. The results also show that the average friction factor – Reynolds number product exhibits a flow Reynolds number dependence, where increasing Reynolds numbers increase the friction factor. Furthermore, the predictions reveal the impact of the vapor cavity regions on the overall frictional resistance, showing that small relative cavity depths increase the friction factor.

In addition to a hydrodynamic study of channel flow through ultrahydrophobic surfaces, the thermal transport was studied as well. A channel was analyzed with a constant wall temperature boundary condition. The model was assumed to be periodically thermally developed. Temperature contours were shown as well as dimensionless temperature profiles and these were discussed to show the effects of ultrahydrophobic surfaces. Significant differences were seen in these profiles; an increase in relative module length and a reduction in Reynolds number tends to cause the temperature profile to be more uniform in the wall normal direction.

The dimensionless heat flux was predicted along the rib and liquid-vapor interface. The results showed that, low Reynolds numbers, small relative module lengths, and small relative cavity depths increased the heat flux. The average Nusselt number was predicted and results show that as the cavity-to-rib length ratio is increased and the relative module length is increased the average Nusselt number is reduced. An increase in the Reynolds number was predicted to increase the Nusselt number and to improve heat transfer. An increase in the relative module length was shown to lower the average

Nusselt number. For the scenarios studied, the relative cavity depth had no apparent effect on the average Nusselt number. In all cases studied it was shown that the vapor cavity decreases heat transfer performance for ultrahydrophobic surfaces compared to fully-developed classical parallel plate channel flow.

A measure of the combined effect of the benefit of drag reduction and the cost of thermal transport compared to a classical scenario was calculated. The results show that as the Reynolds number and slip fraction increase the ultrahydrophobic surface performs better than a classical scenario. This means that the cost of a reduction in heat transfer is outweighed by the benefit of drag reduction.

5.2 RECOMMENDATIONS

It is recommended that additional work be conducted with a different heat transfer boundary condition. One suggestion is to include the ultrahydrophobic surface in the computational domain and to study both a constant temperature and a constant heat flux on this boundary. These results could then be compared to results tabulated in the literature for both of these classical scenarios in the classical case. It is also recommended that the similar studies be performed using other fluids to show the significance of ratio of viscosities and thermal conductivities in both fRe and Nu . Experimental data needs to be gathered to validate the model. It is also recommended that low values of Z_c be resolved to show in greater detail what causes the increase in fRe from that parameter. In general there are many combinations of parameters that can be studied and can add greater detail to what has been predicted here.

REFERENCES

1. J. Ou, B. Perot, and J. P. Rothstein, "Laminar Drag Reduction in Microchannels Using Ultrahydrophobic Surfaces." *Physics of Fluids*, **16**, n. 12 (December 2004); 4635-4643.
2. D. Oner, and J. McCarthy, "Ultrahydrophobic Surfaces. Effects of Topography Length Scales on Wettability." *Langmuir*, **16** (2000); 7777-7782.
3. B. Woolford, K. Jeffs, D. Maynes, and B.W. Webb, "Laminar Fully-Developed Flow in a Microchannel with Patterned Ultrahydrophobic Walls," *Proceedings of the ASME Summer Heat Transfer Conference*, San Francisco, CA, HT2005-72726, (2005).
4. H. Jansen, M. de Boer, R. Legtenberg, and M. Elwenspoek, "The Black Silicon Method: a Universal Method for Determining the Parameter Setting of a Fluorine-based Reactive Ion Etcher in Deep Silicon Trench Etching with Profile Control." *J. Micromech. Microeng.*, **5** (1995); 115-120.
5. J. Kim, and "CJ" Kim, "Nanostructured Surfaces for Dramatic Reduction of Flow Resistance in Droplet-Based Microfluidics." *Proc. 15th IEEE Int. Conf. Micro Electro Mechanical Systems*, MEMS 2002, 20-24. Jan., Las Vegas, 479-482.
6. A. Torkkeli, J. Saarilahti, A. Haara, H. Harma, T. Soukka, And P. Tolonen, "electrostatic Transportation of Water Droplets on Superhydrophobic Surfaces," *Proceedings of the IEEE MEMS 2001 Conference*, 475-482 (2001).
7. J. Kim and C-J. Kim, "Nanostructured Surfaces for Dramatic Reduction of Flow Resistance in Droplet-Based Microfluidics," *Proceedings of the IEEE MEMS 2002 Conference*, Las Vegas, NV, 479-482 (2002).
8. W. Chen, A. Y. Fadeev, M. C. Hsieh, D. Oner, J. Youngblood, and T. J. McCarthy, "Ultrahydrophobic and Ultralyophobic Surfaces: Some Comments and Examples," *Langmuir*, **15**, 3395-3399 (1999).
9. J. P. Youngblood and T. J. McCarthy, "Ultrahydrophobic Polymer Surfaces Prepared by Simultaneous Ablation of Polypropylene and Sputtering of Poly(tetrafluoroethylene) Using Radio Frequency Plasma," *Macromolecules*, **32**, 6800-6806 (1999).
10. J. Bico, U. Thiele, and D. Quere, "Wetting of Textured Surfaces," *Colloids and Surfaces A*, **206**, 41-46 (2002).

11. J. Bico, C. Marzolin, and D. Quere, "Pearl Drops." *Europhysics Letters*, **47** (1999); 220-226.
12. J. Lee, H. Moon, J. Fowler, "CJ" Kim, and T. Schoellhammer, "Addressable Micro Liquid Handling by Electric Control of Surface Tension." *IEEE Int. Conf. Micro Electro Mechanical Systems*, MEMS 2001, Jan., Interlaken, Switzerland, 499-502.
13. C. Choi, J. Kim, and "CJ" Kim, "NanoTurf Surfaces for Reduction of Liquid Flow Drag in Microchannels." *Proc. 3rd ASME 2004: Integrated Nanosystems Conf.: Design, Synthesis & Applications, Pasadena, CA*, (Sept. 2004):IMECE2004-46078.
14. J. R. Philip, "Flows Satisfying Mixed No-Slip and No-Shear Conditions." *Journal of Applied Mathematics and Physics (ZAMP)*, **23**, (1972):353-371.
15. R. Benzi, L. Biferale, M. Sbragaglia, S. Succi, and F. Toschi, "Mesoscopic modeling of Heterogeneous Boundary Conditions for Microchannel Flows." arXiv:nlin.CD/0502060 v1 25 Feb 2005
16. C. Cottin-Bizonne, C. Barentin, E. Charlaix, L. Bocquet, and J.L. Barrat, "Dynamics of simple liquids at heterogeneous surfaces: Molecular-dynamics simulations and hydrodynamic description." *The European Physical Journal E: Soft Matter*, **15**, (2004):427-438.
17. F. M. White, *Viscous Fluid Flow 2nd ed.*, McGraw-Hill, (1991).
18. W. M. Kays, M. E. Crawford, and B. Weigand, *Convective Heat and Mass Transfer 4th ed.*, McGraw-Hill, (2005).
19. F. P. Incropera and D. P. DeWitt, *Fundamentals of Heat and Mass Transfer 5th ed.*, Wiley, (2002).

APPENDIX

APPENDIX A – USER DEFINED FUNCTION USED FOR NUMERICAL MODELING

/** UDF used in specifying boundary conditions at the liquid-gas interface for FLUENT. When imposed at the wall boundaries of the gas and the liquid, this UDF matches velocities and shear stresses at this interface. In other words at each point along the gas-liquid interface the velocity and shear stress of the gas is equal to the velocity and shear stress of the liquid. In this case the Zone ID of the wall adjacent to gas is 1, while the Zone ID of the wall adjacent to liquid is 2. These values must be changed to the corresponding Zone ID of each wall. The liquid profile must be used in setting the X-Component of the shear stress for the liquid wall. The gas profile must be used in setting the X-Velocity Component for the moving wall velocity of the gas wall. */

```
#include "udf.h"
```

```
static real mu = 1.7894e-05          /** viscosity of gas (in this case air) */
```

```
DEFINE_PROFILE(liquid, t, i)
```

```
{
    face_t f;
    cell_t c;
    Thread *gaswall, *cellthread;
    Domain *d;
    int zone_ID = 1;
    d = Get_Domain(1);          /** returns fluid domain pointer */
    airwall = Lookup_Thread(d, zone_ID);
```

```
    begin_f_loop(f, t)
```

```
    {
        c = F_C0(f, gaswall);
        cellthread = THREAD_T0(gaswall);
        F_PROFILE(f, t, i) = -mu*C_U_G(c, cellthread)[1];
    }
    end_f_loop(f, t)
}
```

```
DEFINE_PROFILE(gas, t, i)
```

```
{
    face_t f;
    Thread *liquidwall;
```

```
Domain *d;
int zone_ID = 2;
d = Get_Domain(1);          /* returns fluid domain pointer */
waterwall = Lookup_Thread(d,zone_ID);

begin_f_loop(f, t)
{
    F_PROFILE(f, t, i) = F_U(f,waterwall);
}
end_f_loop(f, t)
}
```